



Deutsches Zentrum
für Luft- und Raumfahrt



Effect of Ultraviolet Light on the Interaction of Lunar Regolith in an Electrodynamical Field

Inaugural-Dissertation

zur

Erlangung des Doktorgrades
der Mathematisch-Naturwissenschaftlichen Fakultät
der Universität zu Köln

vorgelegt von

Ya-Chun Wang

aus Changhua, Taiwan

Köln, 2024

Berichterstatter:
(Gutachter)

Prof. Dr. Matthias Sperl
Prof. Dr. Andreas Schadschneider

Tag der mündlichen Prüfung:

16. September 2024

Abstract

Returning to the lunar surface necessitates the development of technologies that ensure the sustainability and longevity of exploration programs. One of the primary challenges in lunar missions is the pervasive presence of lunar dust, which presents ongoing issues for both astronauts and equipment.

This study evaluates a lunar dust mitigation technology using an ultraviolet source to examine its dust removal efficiency under the primary charging mechanism of the Moon's surface: photoelectric emissions. The technology relies on particles carrying a charge to remove them using an applied electric field, and conveniently, there are plenty natural charging mechanisms that exist on the lunar surface. The current research gap lies in the limited understanding of the interaction between dust particles and electrodynamic dust removal technology (EDS) under realistic lunar conditions, specifically regarding the forces involved in grain mobilisation and their relationship with grain size and type. The dust removal efficiency of the EDS under UV was found to be much above 90% across a range of simulants, size ranges and surface materials, except for a certain particle size range on Beta cloth. This highlights the potential of the EDS as a dust mitigation system, but also the need to avoid certain materials when possible, and the development of dedicated dust removal techniques when the use of certain materials cannot be avoided.

Experiments were conducted in a vacuum environment with a UV source to study the forces influencing particle dynamics under various scenarios. Simulations of a simplified system assessing the magnitude of electric field strength and dielectrophoretic force established the required conditions for dust uplift in this system, and the results indicated a significant contribution of the dielectrophoretic force acting toward the EDS surface. These findings enhance the understanding of the working principles of the EDS system, both in general and in the context of lunar exploration.

Acknowledgements

This thesis was completed with a tremendous amount of support. I would like to thank my professor, Matthias Sperl, for the opportunity to pursue this exciting project, which allowed me to work in an international environment between DLR and ESTEC — an invaluable experience that I will cherish forever.

Thank you to Masato Adachi and Fabrice Cipriani for initiating this project and providing general guidance. Special thanks to Fredrik Lefe Johansson for the final push on the thesis and the meaningful and interesting discussions that made this thesis possible.

Thank you to Fredrik and Luc for proofreading. Their feedback and suggestions greatly improved the quality of this work.

Thank you to all the wonderful people I met at ESTEC, especially Bob Witteveen, Natascha Klein, Jaro Vacca, Thijs Lorrier, Victor Lujan Cuenca, and Luis Pacheco at the battery lab, who provided an amicable work environment and first-hand help without hesitation. I also extend my gratitude to Grégoire Déprez, Johannes Müllers, Oliver Korashy, Bart Butler, Matteo Appolloni, Olivier Schmeitzky, Thomas Bader, Alan Dowson, Jose Ramon Campino, Stefano Trombini, Marcel Van Slogteren, Piers Jiggins, Beth Lomax, Véronique Ferlet-Cavrois, Petteri Nieminen, Yvonne Greville, and everyone at TEC-EPS ESTEC. Thank you also to my DLR colleagues Dirk Bräuer, Raphael Kessler, Hubertus Thomas, Mikhail Pustynnik, Till Kranz, Peidong Yu, Matthias Kolbe, Volodymyr Nosenko, and the workshop team for their support along the way.

Thank you to Luc, Nursel, Yi-Pei, Tien-Cheng, Mélanie, Asbjørn, Lisa, Tzu-Han, Leonardo, Juan-Carlos, Dirk, Alessandro, and Dorota for the mental support, encouragement, and fun times that made the experience exciting and worthwhile.

Lastly, I would like to thank my family for their unconditional support, especially my niece Daisy, whose smile has a special healing power that melts all worries away.

Contents

Abstract	i
Acknowledgements	ii
List of Figures	vi
List of Tables	viii
List of Abbreviations	ix
1 Introduction	1
References	3
2 Lunar Surface Environment	4
2.1 Properties of the Moon	4
2.1.1 Atmosphere	4
2.1.2 Magnetic Field	6
2.1.3 Meteoroid Bombardment	7
2.1.4 Surface Temperature	7
2.2 The Lunar Charging Environment	8
2.2.1 Lunar Plasma and Surface Charging	8
2.2.2 Lunar Dust Transport	14
References	17
3 Lunar Regolith and its Simulants	23
3.1 Lunar Regolith	23
3.1.1 Locations and Geology	23
3.1.2 Lunar Mineralogy	24
3.1.3 Type and Shape	26
3.1.4 Electrical Conductivity	27
3.2 Lunar Simulants	29
3.2.1 Simulant Candidates	30
3.2.2 Characteristics of LHS-1 and LMS-1	30
References	32
4 Dust Mitigation Technologies and Mechanisms	35
4.1 The Dust Problem	35
4.2 Active Dust Mitigation	36
4.2.1 Electrostatic/Electrodynamic Methods	37

4.2.2 EDS Performance in Literature	41
4.3 Passive Dust Mitigation	41
4.4 Implicit Dust Mitigation	44
References	44
5 Forces on Dust grains in an EDS System	48
5.1 Non-Electrostatic Adhesion	48
5.2 Tribocharging	50
5.3 Dielectrophoretic Force	51
References	52
6 Experimental Setup and Methods	55
6.1 Design of EDS in this Work	55
6.2 Sample Preparation	58
6.3 Experimental Facility	62
6.3.1 Vacuum Chamber	62
6.3.2 High-Voltage Peripherals	68
6.3.3 LabVIEW Program	72
6.3.4 High-Speed Camera	73
6.4 Dust Removal Efficiency Quantification	75
6.4.1 Weighing	75
6.4.2 Solar Cell Efficiency	76
6.5 Protocol	77
6.5.1 Limitations and Constraints	80
References	81
7 Measurement of Dust Removal Efficiency	83
7.1 Quantitative Data	84
7.1.1 Response to Different UV Conditions	84
7.1.2 Response to Different Material Coatings	87
7.1.3 Solar Cell Output and Optical Microscope Observations	88
7.2 Qualitative Data	91
7.2.1 Unbaked Simulants and Atmospheric Testing	92
7.2.2 Voltage Amplitude Tests	94
7.2.3 Temperature Effect	94
7.2.4 High-Speed Camera Imaging	95
7.3 Discussion	96
7.3.1 Comparison with Literature Results	96
7.3.2 Dust Particles Less than 25 μm	96
7.4 Summary of Key Findings	98
7.5 Electric Field Simulation with COMSOL	99
7.5.1 Electric Field Strength	99
7.5.2 DEP Force Strength	102
References	106
8 Conclusion and Outlook	108

List of Figures

1.1 Astronaut covered in dust	1
2.1 Magnetosphere from a Moon site	10
2.2 Schematic of lunar electrostatic environment	11
2.3 PSRs in lunar south pole	13
2.4 Electrical breakdown of regolith.	13
2.5 Schematic of levitation models	15
3.1 Lunar rock fragments from Apollo 11	25
3.2 Apollo and Luna sample return	26
3.3 Lunar geology.	26
3.4 LHS-1 and LMS-1 sample	31
3.5 SEM images of JSC-1 from NASA	32
3.6 SEM images of LHS-1 and LMS-1	32
4.1 Substrates/coatings and electrode patterns developed for EDS	39
4.2 MISSE-X mission EDS measurement results	40
4.3 Insulated wire electrodes in spacesuit	42
4.4 Carbon nanotube yarns in a spacesuit	42
6.1 EDS electrode design	56
6.2 Composition of an EDS plate	58
6.3 Different coating materials.	58
6.4 Damaged ITO tracks	59
6.5 Simulant samples in a Petri dish	60
6.6 Dust distribution system	61
6.7 Dust distribution patterns	61
6.8 Sketch of vacuum chamber interior	62
6.9 Vacuum chamber photographs	63
6.10 VUV lamp	64
6.11 View through feedthrough	65
6.12 VUV lamp specification	65
6.13 VUV lamp specification	66
6.14 UV photodiode	67
6.15 Solar cells	68
6.16 LabVIEW and HV amplifier setup	69
6.17 LabVIEW-controlled signal output	70
6.18 Op-amp simulation	71
6.19 Vacuum chamber feedthrough	72

6.20 LabVIEW GUI	73
6.21 LabVIEW block diagram	74
6.22 High-speed camera setup	75
6.23 Surface dust concentration check	78
7.1 Dust removal states	84
7.2 DRE of EDS in different UV conditions	85
7.3 Optical microscope inspection	86
7.4 Tests with Kapton and Beta cloth	87
7.5 DRE of EDS with different coatings	89
7.6 Apollo 16 Beta cloth	90
7.7 Beta cloth cleanliness	90
7.8 Short-circuit current ratio	91
7.9 Unbaked sample test in air	93
7.10 Unbaked sample test in air in literature	93
7.11 Unbaked sample test in vacuum	93
7.12 High-speed camera frames 25-50 μm LMS-1	95
7.13 High-speed camera frames of 80-100 μm LMS-1	95
7.14 SEM of LHS-1	97
7.15 EDS removal of Agglutinates	97
7.16 Fine grains of LHS-1	98
7.17 COMSOL simulation of electric field	100
7.18 COMSOL electric field at different locations	101
7.19 COMSOL electric field strengths and potentials	103
7.20 COMSOL DEP forces	104

List of Tables

2.1 Comparison of Moon and Earth	5
3.1 Major minerals on the Moon	24
3.2 Mineralogical components of regolith simulants	31
4.1 Technology Readiness Levels	36
4.2 Summary of EDS studies in literature	43
6.1 UV test cases	78
7.1 COMSOL electric field values	101
7.2 Properties used in COMSOL simulation	102

List of Abbreviations

AC Alternating Current.

ARTEMIS Acceleration, Reconnection, Turbulence and Electrodynamics of the Moon's Interaction with the Sun.

CME Coronal Mass Ejection.

DEP Dielectrophoretic Force.

DRE Dust Removal Efficiency.

EDS Electrodynamic Dust Shield.

EMU Extravehicular Mobility Unit.

EUV Extreme Ultraviolet.

EVA Extra Vehicular Activity.

GCR Galactic Cosmic Ray.

HV High Voltage.

I_{sc} Short-Circuit Current.

ISS International Space Station.

ITO Indium Tin Oxide.

JSC-1 Johnson Space Center-1.

LDEF Long Duration Exposure Facility.

LEAM Lunar Ejecta and Meteorites Experiment.

MISSE-X Materials International Space Station Experiment X.

List of Abbreviations

NASA National Aeronautics and Space Administration.

PCB Printed Circuit Board.

PSR Permanently Shadowed Region.

PTFE Polytetrafluoroethylene.

SA Solar Array.

SEE Secondary Electron Emission.

SEM Scanning Electron Microscope.

SEP Solar Energetic Particle.

TRL Technology Readiness Level.

UV Ultraviolet.

VUV Vacuum Ultraviolet.

1 Introduction

"After lunar liftoff... a great quantity of dust floated free within the cabin. This dust made breathing without the helmet difficult, and enough particles were present in the cabin atmosphere to affect our vision. The use of a whisk broom prior to ingress would probably not be satisfactory in solving the dust problem, because the dust tends to rub deeper into the garment rather than to brush off." (Bean et al., 1970)

Background

The account above was given by Apollo 12 astronaut Alan Bean, who was echoed by Apollo 17 astronaut Gene Cernan: *"I think dust is probably one of the greatest inhibitors to a nominal operation on the Moon. I think we can overcome other physiological or physical or mechanical problems except dust... One of the most aggravating, restricting facets of lunar surface exploration is the dust and its adherence to everything no matter what kind of material, whether it be skin, suit material, metal, no matter what it be and its restrictive friction-like action to everything it gets on."*



Figure 1.1: Astronaut Gene Cernan covered in lunar dust on the Moon following a moonwalk during Apollo 17. Source: NASA.

These anecdotes highlight the severity of dust in lunar outposts, as astronauts reported not only its ubiquity but also its impact on the mission. Earth's Moon has

gained renewed interest over the past decade, and is the primary destination for human space missions in preparation for journeys to other planets. There are compelling reasons to explore the Moon, as it harbours abundant exploitable resources and can serve as an intermediate stop for further exploration destinations.

As demonstrated by the Apollo and Luna missions, rocket design alone is insufficient for space exploration; the actual conditions encountered on the lunar surface can make or break a mission. Dust on the Moon affects mission success in several ways, including instrument operational efficiency, equipment structural integrity, and resource utilisation. The impact of dust on these aspects of exploration can be costly if we do not find ways to moderate its presence. Understanding the characteristics of lunar dust is crucial not only for health and safety but also for developing strategies to minimise its impact effectively. There are several ways to mitigate the detrimental effects of dust, one of which is the active dust-removal mechanism known as the Electrodynamic Dust Shield (EDS). This technology is designed to reduce dust accumulation on surfaces by using high-voltage alternating-current electric fields to mobilise both charged and uncharged particles. This method effectively removes particles from surfaces without mechanical brushing, which is not only inadequate but also damaging to coatings and fabrics.

Research on EDS has been predominantly carried out by National Aeronautics and Space Administration (NASA), though the technology was initially developed by Japanese researchers who continue to contribute significantly to the field of dust mitigation. Research to date has investigated the degradation of EDS materials resulting from extended exposure to space radiation and debris, their performance under varied atmospheric conditions, and their efficacy across diverse design parameters. A crucial prerequisite for effective dust removal is particle charging. Both simulations and experimental models have been developed to explain dust grain charging mechanisms and particle charge acquisition, which facilitate dust levitation, but no currently available modelling method can fully account for the effects on the Moon. These models have typically employed simplified systems, often featuring a single spherical particle in an electric field. Moreover, experiments have been limited to dust particle removal without an active charging mechanism analogous to that present on the lunar surface.

This study aims to address this gap by using a Ultraviolet (UV) lamp to simulate the primary dust charging mechanism on the lunar dayside — photoemission — with an EDS system. Previous research suggests that dust particles should be repelled by this mechanism, as grains naturally acquire charge through radiation and tribocharging when disturbed. However, there is a lack of comprehensive investigation into how different particle types interact with various EDS coating materials under UV exposure. These particle types vary in size, mineralogy, and shape, each exhibiting distinct charging behaviours. By examining these interactions, this study aims to deepen our understanding of particle dynamics within an EDS electric field. This research can inform future studies and facilitate the development of more effective dust mitigation strategies for lunar environments and beyond.

Thesis Outline

Chapter 1 provided a background on the significance of dust mitigation for lunar exploration. Chapter 2 presents the profile of the Moon, specifically with characteristics related to regolith types and the charging environment. Chapter 3 focuses on lunar regolith characteristics and explores different lunar simulants. Chapter 4 reviews active and passive dust mitigation technologies and mechanisms, highlighting electrostatic/electrodynamic methods and their performances. Chapter 5 analyses the forces influencing dust grains within an EDS system, covering non-electrostatic adhesion, tribocharging, and dielectrophoretic forces. Chapter 6 details the experimental methodologies and setup used in this research, including the design of the EDS system, sample preparation, and experimental facilities. Chapter 7 presents the results and discussion on the measurement of dust removal efficiency under various conditions, supported by quantitative and qualitative data analyses. Chapter 8 concludes with a summary of key findings and offers suggestions into future research directions aimed at advancing dust mitigation strategies.

References

Bean, A. L., C. Conrad Jr., and R. F. Gordon (1970). “Crew observations”. In: *NASA Special Publication 235*, p. 29.

2 Lunar Surface Environment

When discussing the lunar environment, we immediately think of its hostile conditions: lack of atmosphere, extreme temperature fluctuations, low gravity, and expansive grey terrain. These defining features have myriad implications for lunar exploration. How might temperature extremes impact equipment performance? What risks do astronauts face without atmospheric protection against solar and cosmic radiation? These questions provide a glimpse into the complex web of issues that must be addressed for any lunar mission to succeed.

2.1 Properties of the Moon

It is perhaps helpful to begin appreciating the lunar environment by comparing its properties with those of Earth. The lunar gravity is about 1/6 of the Earth's gravity and surface pressure is 10^{-12} mbar. The absence of an atmosphere significantly impacts the lunar environment in several ways: without an atmosphere to regulate heat, the Moon experiences extreme temperature fluctuations and faces a continuous bombardment of photons, plasma, and cosmic rays from the solar wind and galactic sources. High-velocity micrometeorite impacts, unimpeded by any atmospheric layer, also modify the properties of the lunar regolith and create different geological properties everywhere on the Moon. Table [2.1](#) compares the physical differences between the Earth and the Moon.

This section will discuss the significant phenomena occurring on and around the lunar surface that define its unique environment. The review on current research and literature aims to consolidate our current understanding of the Moon from the Apollo era to the latest space missions. This sets the stage for research on lunar dust behaviour and provide the context for this thesis.

2.1.1 Atmosphere

Unlike Earth, the Moon lacks a significant atmosphere (Hoffman et al., [1973](#)). The lack of a global magnetic field and weak gravity are the primary reasons it did not retain its atmosphere. Furthermore, there are no geological activities such as volcanic eruptions or tectonic activity to substantially replenish its atmosphere either. These conditions enable the escape of any remaining gas molecules from the surface, making any measurement of gas molecular abundance essentially indicative of its escape rate.

Table 2.1: Physical comparison of the Moon and Earth (Heiken et al., 1991).

Property	Moon	Earth
Mass	7.353×10^{22} kg	5.976×10^{24} kg
Radius (spherical)	1738 km	6371 km
Surface area	37.9×10^6 km ²	510.1×10^6 km ²
Flattening*	0.0005	0.0034
Mean density	3.34 g/cm ³	5.517 g/cm ³
Gravity at equator	1.62 m/sec ²	9.81 m/sec ²
Escape velocity at equator	2.38 km/sec	11.2 km/sec
Sidereal rotation time	27.322 days	23.9345 hr
Inclination of equator/orbit	6°41'	23°28'
Mean surface temperature	107°C day; -153°C night	22°C
Temperature extremes	-233°C to 123°C	-89°C to 58°C
Atmosphere (molecules/cm ³)	~ 10 ⁴ (day); 2 × 10 ⁵ (night)	2.5 × 10 ¹⁹ STP**
Moment of inertia	0.395	0.3315
Heat flow (average)	~ 29 mW/m ²	63 mW/m ²
Seismic energy	2 × 10 ¹⁰ (or 10 ¹⁴ ?) J/yr [†]	10 ¹⁷ -10 ¹⁸ J/yr
Magnetic field	0 ^{††}	22 - 60 μT

* (Equatorial-ideal)/ideal radii.

** Standard temperature and pressure.

† These estimates account for moonquakes only and do not account for seismicity from meteoroid impacts.

†† The Moon lacks a global magnetic field, but there are local magnetic field mapped out by the Lunar Prospector. See Section 2.1.2 for elaboration.

The absence of an atmosphere impacts various processes such as weathering, erosion, and the scattering of light. There is however a tenuous exosphere, which is a weak surface boundary layer composed of sparse and highly scattered gas molecules that are not bound by gravity and can escape into space (Stern, 1999). The exosphere is created by hypervelocity micrometeoritic impacts (Berezhnoy, 2010), photon-stimulated desorption by UV radiation (Yakshinskiy et al., 2004), and ion sputtering (Mendillo et al., 1999). These processes release gas from lunar rocks. The major constituents of the lunar exosphere are neon, hydrogen, helium, and argon, whose molecular abundances vary from daytime to nighttime due to solar wind fluctuations and adsorption on soil grains (Hodges Jr., 1975). Additionally, the exosphere varies in composition and density with latitude, as the temperature difference becomes smaller at higher latitudes during day-night transitions, and ample sunlight at lower latitudes gives rise to more photoionisation and sputtering.

As confirmed by NASA's Lunar Prospector (W. Feldman et al., 1998) and Stratospheric Observatory for Infrared Astronomy (SOFIA) (Honniball et al., 2021), next to hydroxyl (OH) compounds there is also molecular water (H₂O) on the lunar surface. During the hot lunar daytime these molecules are released from the grains into the atmosphere, at about ~ 50 molecules/cm³ (Hodges Jr., 1975). Without the ability to hold these molecules, they are again lost to space.

2.1.2 Magnetic Field

From 1967 to 1972, the Explorer and Apollo missions first revealed that the Moon lacks a global magnetic field due to the absence of a dynamo effect like that on Earth, where the movement of molten iron in its outer core generates a self-sustaining magnetic field (Sonett et al., 1967; Dyal et al., 1974). However, data from Lunar Prospector later mapped magnetic anomalies on the lunar surface, which are localised areas of magnetised crust. These anomalies are characteristic of the presence of magnetic minerals, primarily composed of iron and iron-rich compounds such as magnetite (Fe₃O₄) and hematite (Fe₂O₃). These minerals become magnetised due to shock waves and heat generated by meteoroid impacts on the lunar surface (impact magnetisation) (Martelli et al., 1977), giving rise to sporadic magnetic fields on the order of nT.

The solar wind (see Section 2.2.1), a stream of charged particles emitted by the Sun, can induce magnetic fields in certain minerals upon interacting with the lunar surface (Mitchell et al., 1998). At the boundary of the Moon's surface, where regions of magnetic anomalies interact strongly with the solar wind, bow shocks occur. These are phenomena where the solar wind encounters sharp transitions in magnetic properties, leading to sudden changes in the solar wind's characteristics such as shock waves, caused by abrupt deceleration, deflection, or compression of particles (Ness et al., 1968).

2.1.3 Meteoroid Bombardment

Meteoroid impacts represent a significant hazard to lunar structures, which includes habitat and instruments, and with every impact, dust particles are disturbed and redistributed into the vicinity, causing depositions onto nearby equipment. This section discusses various attempts to measure the frequency of impacts and the challenges associated with these measurements.

Long-term lunar impact studies face several challenges, including logistical difficulties in maintaining consistent data collection over extended periods. These studies require autonomous, durable instruments and reliable data transmission to Earth. The limited number of lunar missions constrains spatial coverage, while gaps in historical data hinder the establishment of comprehensive trends. As a result, understanding variations across different lunar regions and time periods remains difficult, impeding efforts to draw robust conclusions about long-term impact patterns on the Moon.

A meteoroid is a small body ranging in size from a grain of sand to a few meters in diameter, and meteoroids with a diameter of less than 1 mm are classified as micrometeoroids. The cratered surface of the Moon is a product of the impacts made by meteoroids, which create holes of varying sizes and contribute to the ongoing process of erosion and surface modification. The number of impacts per day per unit area varies depending on the location.

Data from five Lunar Orbiters (1966-1967) indicated that the penetration rate of 0.025-mm-thick beryllium-copper detectors in the near-lunar environment is approximately half the rate observed in Earth's vicinity, though this rate is variable due to secondary meteoroids and equipment sensitivity (Grew, 1971). For instance, while Lunar Orbiters recorded a rate of $0.16 \text{ m}^{-2} \text{ day}^{-1}$, Luna 10 recorded a significantly higher rate of $345.6 \text{ m}^{-2}/\text{day}$ (Nazarova et al., 1967). The Lunar Ejecta and Meteorites Experiment (LEAM) on Apollo 17 registered hundreds of impacts daily from 1972 onwards (Rhee et al., 1977), and Surveyor 3 suggested that the lunar micrometeoroid flux could impair optical equipment (Carosso, 1987). NASA's Lunar Impact Monitoring Program (2005) tracked lunar impacts using telescopes and video devices, though it could only detect larger impacts (Suggs et al., 2008). Additionally, Vanzani et al. (1997) used terrestrial flux extrapolation to estimate 30 microcraters larger than 0.1 mm per square meter per year on the Long Duration Exposure Facility (LDEF), with the meteoroid flux on the Moon estimated at 0.6766 times that on Earth (Borin et al., 2009).

2.1.4 Surface Temperature

The equatorial temperature on the Moon's surface can fluctuate greatly, ranging from below 100–400 K, primarily due to the absence of an atmosphere for temperature regulation (Vasavada et al., 2012; Malla et al., 2015). Data collected over nearly six years by the Diviner Lunar Radiometer aboard the Lunar Reconnaissance Orbiter (LRO) has provided detailed surface temperature maps, revealing extreme

thermal conditions. Daytime temperatures near the equator can reach highs of 387–397 K at noon, plummeting to around 95 K before sunrise. In contrast, polar regions, beyond 85° latitude, experience average maximum temperatures of approximately 200 K and average minimum temperatures of about 50 K. Interestingly, the southern polar region tends to have slightly higher average maximum temperatures, about 11 K more than the northern polar region (Williams et al., 2017).

The thermophysical properties of the regolith are noteworthy as they significantly moderate nighttime temperatures. Larger rocks retain heat more effectively during the long lunar nights, with only the outermost 30 cm of regolith affected by solar radiation, temperature variations diminish with increasing depth of the regolith layer (Malla et al., 2015). Surface features such as craters, mountains, valleys, ridges, and plains also contribute to temperature variations, especially in permanently shadowed areas.

The large fluctuations in temperature have significant implications, particularly regarding material characteristics such as thermal expansion and contraction. These fluctuations give rise to several issues in terms of exploration, including maintaining structural stability and ensuring the proper functioning of mechanical components within complex devices. Notably, the extreme temperature variations in some lunar regions also allow for the presence of water ice, particularly in permanently shadowed craters near the poles where temperatures remain low enough to prevent sublimation. This study will focus on how temperature affects the electrical properties of lunar regolith.

2.2 The Lunar Charging Environment

The electrostatic environment on the Moon is characterised by the interaction of various charged particles and fields. These include the plasma environment generated by solar UV radiation, solar wind, cosmic rays, micrometeoroid impacts, and the lunar exosphere. The plasma is dynamic, varying based on the electrostatic potential of the surface layer and the Moon's position relative to the Sun and Earth. The regolith can also acquire charge through mechanisms like triboelectric charging induced by mobilised particles, either by natural or artificial processes. The resulting fields from these charged particles influence dust mobility, surface charging, and interactions with plasma. This section will describe the lunar plasma environment and its implications for studying electrostatics related to particles for dust mitigation purposes.

2.2.1 Lunar Plasma and Surface Charging

As mentioned in previous sections, the interplay of the Moon's distinctive characteristics gives rise to a multifaceted and fascinating plasma environment. As the Moon orbits the Earth, it experiences different plasma conditions depending on its relative position to the Earth and the Sun. The lunar surface plasma conditions vary, with

distinct environments occurring under different circumstances. This section explores these diverse plasma regimes encountered on the Moon.

As any object submersed in a plasma, the collection and emission of charged particles serve to charge the lunar surface until it reaches an equilibrium potential where the net current is zero. With the Moon receiving unimpeded streams of ions and radiation, various processes such as surface reflection/scattering, photoelectron emission, and secondary electron emission create a dynamic plasma system (Halekas et al., 2011). In the case of the poorly conducting lunar surface, the charging is not necessarily uniform, causing radial and horizontal local electric fields to form.

Measurements made by instrument onboard NASA's Lunar Prospector identified the major electrostatic charging processes on the lunar surface: 1) photoemission of electrons J_{ph} , 2) plasma electrons J_e , 3) plasma ions J_p and 4) secondary electrons J_{sec} . Note that J_{sec} is primarily a result of surface ionisation by J_e (Stubbs et al., 2007). There are a few different regions of plasma that the moon encounters, the usual distinctions used for lunar investigations are the solar wind, the magnetosheath and the plasmashet/magnetotail (see Figure 2.1). The solar wind consists mainly of a relatively cool (about 5–10 eV) and dense (on the order of 10 cm^{-3}) plasma, but there are also Solar Energetic Particle (SEP) events (Halekas et al., 2009) and coronal mass ejections (Farrell et al., 2013) as occasional enhanced fluxes of particles that can modulate the charging behaviour. The magnetosheath and plasma sheet are within Earth's magnetosphere and are both characterised by much lower densities, often below 0.1 cm^{-3} , and much higher electron energies (up to several keV). These regions internally also experiences large variations in densities, flow speeds and temperatures, which ultimately depend on Earth magnetosphere's reaction to the solar wind and solar activity: space weather.

To clarify potential confusion, the term 'space weather' refers to the dynamic and varying conditions in space influenced by solar activity and solar wind. The term 'space weathering' on the other hand, is a collection of processes through which the lunar surface is charged and in some cases, physically altered. This includes new impact melt glass bonds creation from micrometeoroid impact, rock damage from high-energy cosmic rays and solar wind surface transformation. These weathering processes can be categorised into random impacts by small physical particles throughout the solar system, and electromagnetic radiation (solar X-ray, Extreme Ultraviolet (EUV), flares) and plasma from the Sun (solar wind, Coronal Mass Ejection (CME), SEP), galactic sources (cosmic rays, gamma ray bursts) or magnetic storms etc. While both terms involve the effects of space conditions, 'space weather' focuses on dynamic solar and cosmic events impacting space environments and technology, whereas 'space weathering' refers to the long-term alteration of surface materials on celestial bodies due to exposure to the space environment.

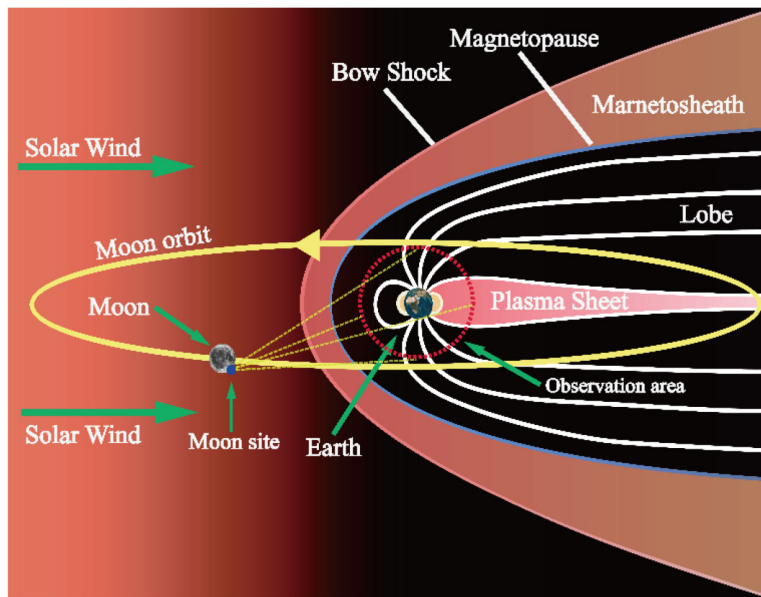


Figure 2.1: Illustration of the Moon’s orbital path (yellow line) interacting with Earth’s magnetosphere. The lines surrounding the Earth illustrate the different regions of the Earth’s magnetosphere. Source: Chen et al. (2021).

Dayside of the Moon

The solar UV radiation is the main charging mechanism on the lunar dayside. The process of UV charging a material by releasing electrons from its surface is called the photoelectric effect. These emitted electrons are called photoelectrons and are sometimes grouped as a specific type of Secondary Electron Emission (SEE): when incident primary particles (photons for photoelectrons) of sufficient energy interact with a dust grain, they can excite and emit a secondary electron from the grain, which leads to a positive charge on the grains. Understanding the photoemission and secondary electron yield of the lunar surface is crucial for characterising its electrostatic charging environment. This yield, defined as the number of emitted electrons per incident primary particle, varies depending on several factors such as surface material, surface porosity/roughness, and degree of structural disorder (Dove et al., 2018).

Feuerbacher et al. (1972) measured a photoelectron yield of 0.07 and a work function of 5 eV from actual lunar soil in laboratory experiments using photon energies from 4–21 eV (wavelengths of approximately 59–310 nm). In contrast, they calculated a photoelectron yield of 0.1 using CPLEE data collected in situ when the Moon was in the geomagnetic tail. Subsequent studies by Abbas et al. (2006) and Abbas et al. (2007) found significant differences in charging behaviours driven by photoemission between micron-sized simulant particles and Apollo sample particles compared to measurements on bulk materials (Wyatt, 1969; Feuerbacher et al., 1973). Recent data from Acceleration, Reconnection, Turbulence and Electrodynamics of the Moon’s Interaction with the Sun (ARTEMIS) missions in both Earth’s magnetotail

and solar wind environments provided a lower limit of 10^{-3} for the photoemission yield for photon energies above 20 eV, with uncertainties spanning approximately four orders of magnitude (Xu et al., 2021).

Current equilibrium on the sunlit lunar surface is reached at potential around +5 to +10 V (Manka, 1973), and photoelectrons form a sheath about 1 m above the lunar surface with a density of 10^3 to 10^4 electrons/cm³ (Singer et al., 1962b). Therefore, both the surface charging processes and the plasma environment on sunlit faces of the moon does not change significantly regardless if the moon is in the solar wind or within Earth’s magnetosphere. On the nightside however, this is no longer the case.

Nightside of the Moon

On the nightside of the moon, photoemission disappears, and the dominating current to the regolith is instead J_e , the electrons from the surrounding plasma, charging the surface on the nightside negative. Although the Earth’s magnetosheath and magnetotail are less dense than the solar wind, the energies of the electrons are significantly higher, rendering the surface charge comparably more negatively to about -50 to -200 V. The potential can even go up to some kilovolts when experiencing periods of intense solar activity or Earth plasmasheet/magnetotail crossings (Halekas et al., 2009). Figure 2.2 illustrates the processes occurring on the lunar surface. Note also that ARTEMIS observations on the lunar nightside surface suggest an additional current source, likely originating from micrometeoroid impact-generated plasma as these impacts may contribute to surface charging on airless bodies with low ambient plasma densities (Stubbs et al., 2007; Poppe et al., 2021).

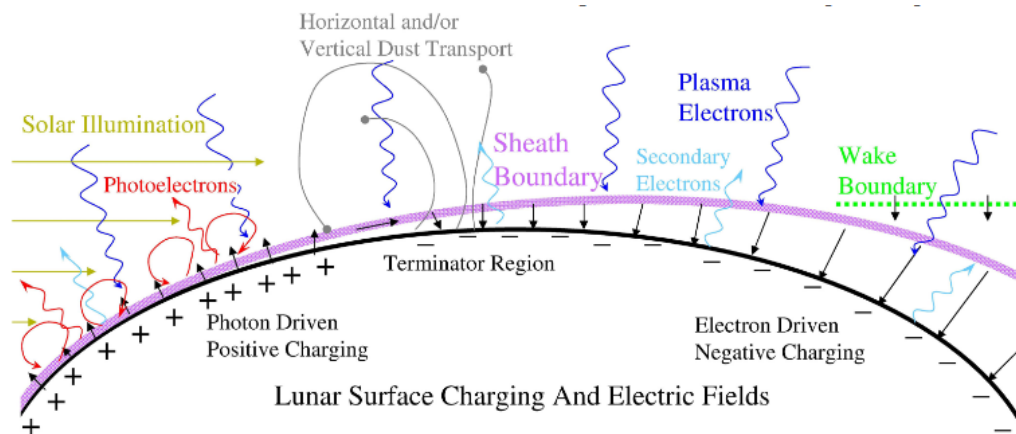


Figure 2.2: Schematic of the electrostatic environment on the lunar surface and which radiation types exist on different regions of the Moon (not to scale). The terminator region is where the sunlit (day)side transitions into the nightside. Dayside of the moon is charged positively due to photoelectrons and the nightside is charged negatively due to plasma electrons. Source: Stubbs et al. (2007).

Space Weathering: Dielectric Breakdown of Lunar Regolith

Lunar regolith is prone to breakdown for several reasons. The grains often have irregular and jagged shapes, and these pointed projections can amplify local electric fields by one to two orders of magnitude compared to the average electric field (Bahder et al., 1982), and inclusions (impurities or gas/fluid) in the regolith particles (lithic clasts, breccias, agglutinates) create boundaries that increase the local electric field, thus decreasing the material's resistance to breakdown (Hara et al., 1998; Fujita et al., 2001; Andres et al., 2001).

Galactic Cosmic Ray (GCR) and SEP events can charge the lunar surface, especially in the polar regions. The model from Jordan et al. (2014) shows that GCR and SEP events may cause dielectric breakdown in which strong electric field ($\geq 10^7$ V/m, typical for most solids (Budenstein, 1980)) rapidly vapourises small channels along mineralogical boundaries within the regolith grains. The breakdown caused by energetic particle deposition must occur within the material's characteristic discharging timescale τ , defined as $\tau = \epsilon/\sigma_c$, where ϵ is the material permittivity and σ_c its conductivity (Buhler et al., 2007). The highly electrically insulating properties of lunar regolith cause charge accumulation to occur more rapidly than the local relaxation process, leading to discharge.

Breakdown has been well studied in spacecraft charging, but it has not been considered as much as for airless body surfaces. In Permanently Shadowed Region (PSR), the regolith there likely has experienced up to 2×10^6 SEP events that are capable of dielectric breakdown in their charging history, a phenomenon that may be able to increase the amount of fine and monomineralics grains within those PSRs; up to 10–25% of PSR regolith is melted or vapourised via dielectric breakdown, comparable to weathering by meteoroid impacts (Jordan et al., 2015; Jordan et al., 2017). SEPs penetrate ~ 1 mm into the regolith layer, which is deeper than the diameter of a typical grain size, and this is the layer where breakdown would occur. Figure 2.3 depicts a map of PSRs that account for approximately three percent of the lunar southern polar region.

Fig. 2.4 shows the estimated yearly rate of SEP events that cause breakdown. The coldest polar regions are predicted to experience breakdown-inducing SEP events more than once per year. Note that larger pieces of rock have an electrical conductivity about four orders of magnitude greater than granular soil (Olhoeft et al., 1974), making their discharging timescales too short for breakdown to happen.

The temperature dependence of conductivity (further discussed in Section 3.1.4) means that regolith at the much colder PSR environment dissipates internal charge more slowly than the other regions and this translates to a larger build up of magnitude of the subsurface electric field. Comparing to temperatures above 160 K, PSRs regolith discharging can take around 20 days (Jordan et al., 2015).

The dielectric breakdown phenomenon is a potential issue for electrodynamic dust mitigation technology, particularly in PSRs or areas frequently exposed to increased solar activity. If dielectric breakdown occurs in either the regolith or the surface

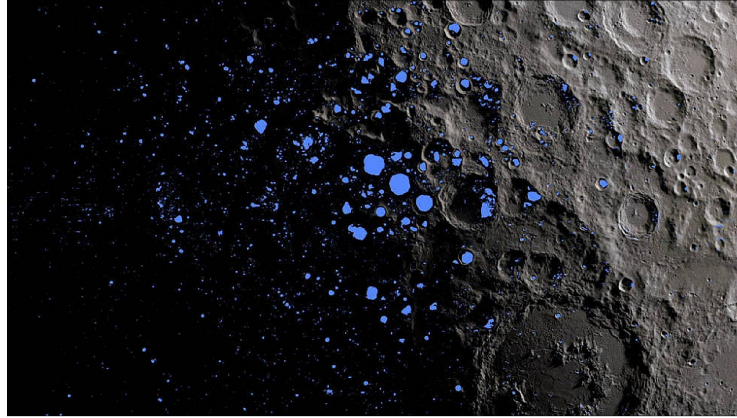


Figure 2.3: PSRs (in blue) in the Moon's south pole region, where a heightened rate of breakdown-inducing SEP events are expected. Source: NASA Goddard LRO mission.

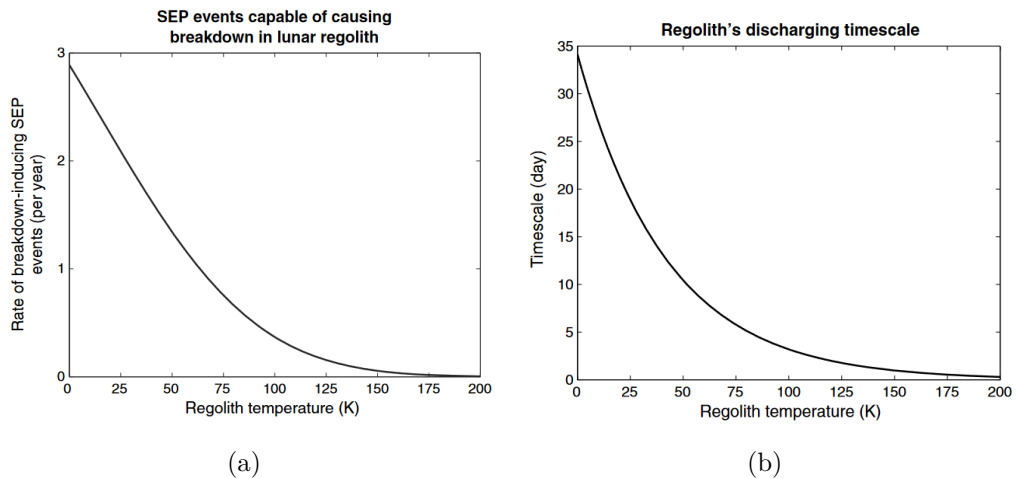


Figure 2.4: (a) Estimated yearly rate of breakdown-inducing SEP events on lunar regolith with respect to regolith surface temperature. (b) Characteristic electrical discharging timescale of lunar regolith with respect to regolith surface temperature. Source: (Jordan et al., 2015).

material, the technology's effectiveness could be compromised, as the surface material may undergo permanent degradation. Furthermore, this technology relies on charged particles responding to the generated electric field for dust removal. Any conductive surface elements would essentially neutralise the charges, undermining the effectiveness of the system.

A brief mention on a lesser-discussed aspect of the lunar environment, probably due to the scarcity of its presence: water. Water is not only an important commodity on the Moon for mission longevity, it could also play a role in the lunar electrostatic environment. Moisture on insulating materials is known to increase their dielectric loss by creating a thin layer that may modify the surface properties of materials, impacting their capacity to retain or accumulate charges (Sow et al., 2013; Toth III

et al., [2017](#)). Since the Moon is a body of unmagnetised dielectric material, charges are retained exceptionally well, but even in low quantity, water could be one of the ways in which particles are discharged on the lunar surface. Two deliberate impact experiments conducted on the lunar surface, one by Chandrayaan-1's Moon Impact Probe (MIP) and the other by Lunar Crater Observation and Sensing Satellite (LCROSS), identified water vapor in the tenuous lunar environment across a large area on the sunlit side (Sridharan et al., [2010](#); Anand, [2010](#)). Substantial amounts of water and organic compounds were also detected in the impact plume created by LCROSS near the lunar South Pole (Colaprete et al., [2010](#); Gladstone et al., [2010](#)). The extent to which water moisture affects dust dynamics on the lunar surface is unknown but likely minimal.

2.2.2 Lunar Dust Transport

Numerous theories have attempted to explain the mechanisms by which particles migrate across the lunar surface. One of the earliest theories is the electrostatic erosion mechanism. According to this theory, charges from the solar wind accumulate on dust grains, and once these grains are sufficiently charged, the repulsion between similarly charged particles can cause them to be lifted off the surface and suspended in the thin exosphere. This process is believed to contribute to the gradual erosion of the lunar surface over time. Grannis ([1961](#)) estimated the rate of mass transport by a mechanism which depends on the buildup of a potential on individual dust grains as a result of a random accretion process. The photoelectrons and ions hitting and leaving the dust grains deviate from an equilibrium value, and two neighbouring grains might experience a sufficiently large force to bring about the ejection of one of the grains from the surface, resulting in movement.

However, Singer et al. ([1962a](#)) suggests that the forces binding the dust layer, or even the weight of the particles, are much stronger than the electric fields produced by UV radiation. Additionally, Walker ([1962](#)) calculated the probability of large charge fluctuations, demonstrating that this mechanism will not result in significant mass transport across the lunar surface, electrostatic transport is therefore not considered the primary process by which dust grains are moved on a large scale, and any appreciable transport is attributed to meteoric impact, a process that also contributes to the breakdown of surface material into finer particles.

Simulation and Experimental Investigations of Dust Levitation

Opposing the uplifting forces are typically gravity and adhesive forces. There are generally four forces responsible for particle adhesion: van der Waals forces (vdW), mechanical interlocking, electrostatic forces, and capillary forces. On the Moon, electrostatic adhesion among like-charge particles frequently exceeds vdW forces by several orders of magnitude (Hartzell et al., [2011](#); Berkebile et al., [2012](#)); for polarisable particles contacting a rough conducting surface, electrostatic forces can dominate adhesion for particle sizes as small as around 1–10 μm . Capillary forces are

virtually non-existent due to the vacuum and lack of moisture. The rough surfaces of regolith particles suggest that mechanical interlocking could be prevalent, and the occurrence of single particles might be rare.

To evaluate the adhesive force between two surfaces, it is necessary to consider the geometry and properties of the surrounding medium. Experimentally accounting for these short-range interactions is challenging due to the difficulties in identifying and isolating the precise mechanisms involved.

In the simulation work done by Colwell et al. (2009), it was found that only particles with a radius of less than approximately $0.5 \mu\text{m}$ can levitate above the lunar surface, while larger particles follow nearly ballistic trajectories. Some particles were observed to be launched at high velocities, reaching heights of kilometers above the surface (Yeo et al., 2021), which theoretical models could not explain. Champlain et al. (2016) devised an experimental setup to study dust charging using Vacuum Ultraviolet (VUV) in the absence of plasma, simulating the conditions on the Moon's dayside. Their findings indicate that dust levitation is challenging under the conditions present on both sides of the terminator region. Stubbs et al. (2006) proposed a dynamic fountain model to account for the observations of $0.1 \mu\text{m}$ -scale particles at $\sim 100 \text{ km}$ lunar terminator surface altitude. Figure 2.5 compares the static levitation concept proposed by Criswell (1973) and others, versus the evolution of a dust grain in the dynamic fountain model.

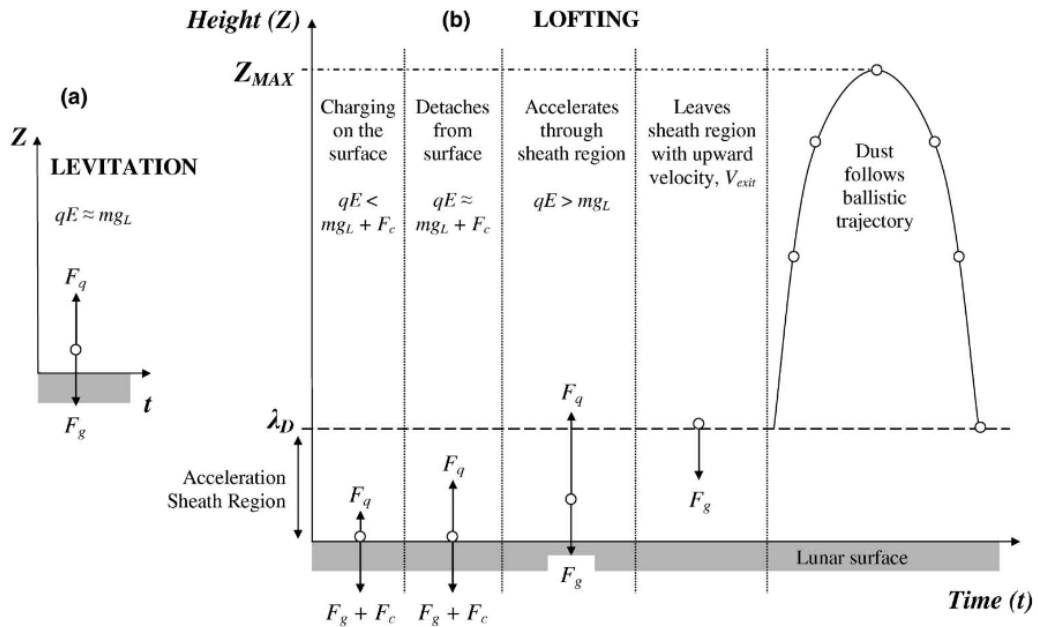


Figure 2.5: Schematic depicting (a) the static levitation model (b) the dynamic fountain model. The dynamic fountain model accounts for the particles observed at 100 km above the lunar surface, which cannot be explained by the static levitation model. Source: Stubbs et al. (2006)

Since these dielectric particles can retain their charges for extended periods, their

charging history should also be considered. Wang et al. (2016) and Schwan et al. (2017) experimentally demonstrated that, upon UV-irradiation, a pile of selected dust grains was able to eject some particles due to a large accumulation of negative charges inside microcavities. Furthermore, Oudayer et al. (2019) modelled a multi-layer dust pile and found that the first two layers tend to charge differentially under VUV irradiation at an incident angle of 45° , compared to a normal incident angle. Particles in the lower layers may charge more negatively due to electron collection. Hood et al. (2018) showed that dust lofting is also a time-dependent process as mobilised dust particles disturb the interparticle microcavities, causing the cavity structures to slowly disappear as the surface conditions reset from the lofting. This process gradually reduces the charge accumulation effect over time.

According to the current literature, there is little robust theoretical estimation indicating that electrostatic forces can overcome adhesion and gravity on the lunar surface, despite the comparatively overwhelming observation indicating the opposite. Experimentally observed lofting has only been seen with aggregated particles, rather than individual particles. The dynamic of a group of particles is difficult to simulate, and so far this case has not been accounted for, so there is a discrepancy in the theoretical model and observation.

Experiments on insulating and semiconductor materials in plasma with energetic electrons have shown that the charge on particles increases linearly with size for diameters ranging from 30 to 120 μm Walch et al. (1995). Experimental investigations on phototelectric and triboelectric charging of dust showed that non-conducting grains have large initial triboelectric charging potential up to ± 15 V and are generally weak photoemitters, suggesting that triboelectric charging may be the main process that gives the particles enough charge to be released from the surface (Sickafoose et al., 2001).

Current literature suggests that a fine balance is required to achieve particle levitation on the lunar surface. Particles must be large enough to accumulate sufficient charge, yet small enough to minimise contact points and reduce adhesion, and light enough to overcome gravity. Experimental conditions that accurately mimic the lunar atmosphere, regolith, and plasma environment do not currently exist, leaving the topic of dust levitation mechanisms still open to debate.

Observation of Dust Levitation

Over the years, increasing evidence has emerged supporting active dust activity at or near the lunar terminator regions. The electric field near the lunar surface at the terminator region is complex, and this complexity arises from the crossing of dayside-positive and nightside-negative potentials, along with the intensely negative potentials in the low plasma density wake region. Popel et al. (2015) demonstrated that an excitation of electric fields on the order of 300 V/m is possible. The electric field strength near the Earth's surface is on average around 100 V/m (Harrison, 2011), so 300 V/m is significant in the context of the lunar environment, where it

can influence dust behaviour. This transition occurs on the illuminated side of the terminator, where the incidence angle of solar photons decreases, yet fast thermal electrons can still directly reach the surface (Freeman et al., 1975). It is speculated that the electric fields generated by the rapid transition from positive to negative potentials in this region are strong enough to loft particles (Criswell, 1973; Colwell et al., 2007; Farrell et al., 2007; Szalay et al., 2015; Vaverka et al., 2016).

The Surveyor landers (1966-1968) provided early indications of lunar dust activity, capturing images of the lunar surface that showed a "horizon glow". The phenomenon is a result of forward scattering of sunlight by electrically charged dust grains of $\sim 10\ \mu\text{m}$ in diameter (Criswell, 1973). The LEAM experiment on Apollo 17 detected high rates of particle impacts, suggesting dust movement, though the results were complicated by thermal noise (Berg et al., 1976).

Other evidence includes Apollo 17 astronaut observations from the orbiting command module (McCoy et al., 1974; Zook et al., 1991), and photographic evidence obtained by Surveyors 5, 6, and 7 showing a bright glow 3 to 30 cm above the surface, and possibly camera images from the Clementine spacecraft (Zook et al., 1995). However, it is important to consider that 'levitation of dust' does not necessarily imply the existence of a stable, permanent layer.

The Lunar Dust Experiment (LDEX), part of the Atmosphere and Dust Environment Explorer (LADEE) mission, was specifically designed to search for a presumed high-density population of small grains (approximately 0.3 μm) (Horányi et al., 2015). However, despite expectations, LDEX did not detect the anticipated density increases over the terminator regions in the altitude range of 3 to 250 km (Szalay et al., 2015).

References

- Abbas, M. M. et al. (2006). "Photoelectric emission measurements on the analogs of individual cosmic dust grains". In: *The Astrophysical Journal* 645.1, p. 324.
- Abbas, M. M. et al. (2007). "Lunar dust charging by photoelectric emissions". In: *Planetary and Space Science* 55.7-8, pp. 953–965.
- Anand, M. (2010). "Lunar water: a brief review". In: *Earth, Moon, and Planets* 107, pp. 65–73.
- Andres, U. et al. (2001). "Liberation of valuable inclusions in ores and slags by electrical pulses". In: *Powder Technology* 114.1-3, pp. 40–50.
- Bahder, G. et al. (1982). "Physical model of electric aging and breakdown of extruded polymeric insulated power cables". In: *IEEE Transactions on Power Apparatus and Systems* 6, pp. 1379–1390.
- Berezhnoy, A. A. (2010). "Meteoroid bombardment as a source of the lunar exosphere". In: *Advances in Space Research* 45.1, pp. 70–76.
- Berg, O. E., H. Wolf, and J. Rhee (1976). "Lunar soil movement registered by the Apollo 17 cosmic dust experiment". In: *Interplanetary Dust and Zodiacal Light*.

- Ed. by H. Elsässer and H. Fechting. Vol. 48. Lecture Notes in Physics. Berlin, Heidelberg: Springer. DOI: [10.1007/3-540-07615-8_486](https://doi.org/10.1007/3-540-07615-8_486).
- Berkebile, S. and J. Gaier (2012). “Adhesion in a vacuum environment and its implications for dust mitigation techniques on airless bodies”. In: *42nd International Conference on Environmental Systems*, p. 3465.
- Borin, P. et al. (2009). “Statistical analysis of micrometeoroids flux on Mercury”. In: *Astronomy & Astrophysics* 503.1, pp. 259–264.
- Budenstein, P. P. (1980). “On the mechanism of dielectric breakdown of solids”. In: *IEEE Transactions on Electrical Insulation* 3, pp. 225–240.
- Buhler, C. R. et al. (2007). “Test method for in situ electrostatic characterization of lunar dust”. In: *2007 IEEE Aerospace Conference*. IEEE, pp. 1–19.
- Carosso, N. J. P. (1987). “Space Station users contamination requirements”. In: *Optical Systems Contamination: Effects, Measurement, Control*. Vol. 777. SPIE, pp. 138–145.
- Champlain, A. et al. (2016). “Lunar dust simulant charging and transport under UV irradiation in vacuum: Experiments and numerical modeling”. In: *Journal of Geophysical Research: Space Physics* 121.1, pp. 103–116.
- Chen, G. et al. (2021). “Influence of topography on the site selection of a Moon-based Earth observation station”. In: *Sensors* 21.21, p. 7198.
- Colaprete, A. et al. (2010). “Detection of water in the LCROSS ejecta plume”. In: *science* 330.6003, pp. 463–468.
- Colwell, J. E. et al. (2007). “Lunar surface: Dust dynamics and regolith mechanics”. In: *Reviews of Geophysics* 45.2.
- Colwell, J. E. et al. (2009). “Lunar dust levitation”. In: *Journal of Aerospace Engineering* 22.1, pp. 2–9.
- Criswell, D. R. (1973). “Horizon-glow and the motion of lunar dust”. In: *Photon and Particle Interactions with Surfaces in Space: Proceedings of the 6th Eslab Symposium, Held at Noordwijk, the Netherlands, 26–29 September, 1972*. Springer, pp. 545–556.
- Dove, A. et al. (2018). “Laboratory investigation of the effect of surface roughness on photoemission from surfaces in space”. In: *Planetary and Space Science* 156, pp. 92–95.
- Dyal, Palmer, Curtis W Parkin, and William D Daily (1974). “Magnetism and the interior of the Moon”. In: *Reviews of Geophysics* 12.4, pp. 568–591.
- Farrell, W. M. et al. (2007). “Complex electric fields near the lunar terminator: The near-surface wake and accelerated dust”. In: *Geophysical Research Letters* 34.14.
- Farrell, W. M. et al. (2013). “The lunar photoelectron sheath: A change in trapping efficiency during a solar storm”. In: *Journal of Geophysical Research: Planets* 118.5, pp. 1114–1122.
- Feldman, W. et al. (1998). “Fluxes of fast and epithermal neutrons from Lunar Prospector: Evidence for water ice at the lunar poles”. In: *Science* 281.5382, pp. 1496–1500.
- Feuerbacher, B., R. F. Willis, and B. Fitton (1973). “Electrostatic potential of interstellar grains”. In: *Astrophysical Journal* 181, pp. 101–114.

- Feuerbacher, B. et al. (1972). “Photoemission from lunar surface fines and the lunar photoelectron sheath”. In: *Proceedings of the Lunar Science Conference*. Vol. 3, p. 2655.
- Freeman, J. W. and M. Ibrahim (1975). “Lunar electric fields, surface Potential and Associated Plasma Sheaths”. In: *The Moon* 14, pp. 103–114. DOI: [10.1007/BF00562976](https://doi.org/10.1007/BF00562976).
- Fujita, T. et al. (2001). “Crushing and liberation of materials by electrical disintegration”. In: *European Journal of Mineral Processing and Environmental Protection* 1.2, pp. 113–122.
- Gladstone, G. R. et al. (2010). “LRO-LAMP observations of the LCROSS impact plume”. In: *Science* 330.6003, pp. 472–476.
- Grannis, P. D. (1961). “Electrostatic erosion mechanisms on the Moon”. In: *Journal of Geophysical Research* 66.12, pp. 4293–4299.
- Grew, G. W. (1971). *The Lunar Orbiter meteoroid experiments: Description and results from five spacecraft*. National Aeronautics and Space Administration.
- Halekas, J. S. et al. (2009). “Lunar surface charging during solar energetic particle events: Measurement and prediction”. In: *Journal of Geophysical Research: Space Physics* 114.A5.
- Halekas, J. S. et al. (2011). “New views of the lunar plasma environment”. In: *Planetary and Space Science* 59.14, pp. 1681–1694.
- Hara, M. and H. Okubo (1998). “Electrical insulation characteristics of superconducting power apparatus”. In: *Cryogenics* 38.11, pp. 1083–1093.
- Harrison, R. G. (2011). “Fair weather atmospheric electricity”. In: *Journal of Physics: Conference Series*. Vol. 301. 1. IOP Publishing, p. 012001.
- Hartzell, C. M. and D. J. Scheeres (2011). “The role of cohesive forces in particle launching on the Moon and asteroids”. In: *Planetary and Space Science* 59.14, pp. 1758–1768.
- Heiken, G., D. T. Vaniman, and B. M. French (1991). *Lunar Sourcebook: A User’s Guide to the Moon*. 2nd. Cambridge, UK: Cambridge University Press. ISBN: 978-0-521-33444-0.
- Hodges Jr., R. R. (1975). “Formation of the lunar atmosphere”. In: *The Moon* 14.1, pp. 139–157.
- Hoffman, J. H. et al. (1973). “Lunar atmospheric composition results from Apollo 17”. In: *Proceedings of the Lunar Science Conference*. Vol. 4, p. 2865.
- Honniball, C. I. et al. (2021). “Molecular water detected on the sunlit Moon by SOFIA”. In: *Nature Astronomy* 5.2, pp. 121–127.
- Hood, N. et al. (2018). “Laboratory investigation of rate of electrostatic dust lofting over time on airless planetary bodies”. In: *Geophysical Research Letters* 45.24, pp. 13–206.
- Horányi, M. et al. (2015). “The lunar dust experiment (LDEX) onboard the lunar atmosphere and dust environment explorer (LADEE) mission”. In: *The Lunar Atmosphere and Dust Environment Explorer Mission (LADEE)*, pp. 93–113.
- Jordan, A. P. et al. (2014). “Deep dielectric charging of regolith within the Moon’s permanently shadowed regions”. In: *Journal of Geophysical Research: Planets* 119.8, pp. 1806–1821.

- Jordan, A. P. et al. (2015). “Dielectric breakdown weathering of the Moon’s polar regolith”. In: *Journal of Geophysical Research: Planets* 120.2, pp. 210–225.
- (2017). “The rate of dielectric breakdown weathering of lunar regolith in permanently shadowed regions”. In: *Icarus* 283, pp. 352–358.
- Malla, R. B. and K. M. Brown (2015). “Determination of temperature variation on lunar surface and subsurface for habitat analysis and design”. In: *Acta Astronautica* 107, pp. 196–207.
- Manka, R. H. (1973). “Plasma and potential at the lunar surface”. In: *Photon and Particle Interactions with Surfaces in Space: Proceedings of the 6th Eslab Symposium, Held at Noordwijk, the Netherlands, 26–29 September, 1972*. Springer, pp. 347–361.
- Martelli, G. and G. Newton (1977). “Hypervelocity cratering and impact magnetisation of basalt”. In: *Nature* 269.5628, pp. 478–480.
- McCoy, J. E. and D. R. Criswell (1974). “Evidence for a high altitude distribution of lunar dust”. In: Pergamon Press.
- Mendillo, M., J. Baumgardner, and J. Wilson (1999). “Observational test for the solar wind sputtering origin of the Moon’s extended sodium atmosphere”. In: *Icarus* 137.1, pp. 13–23.
- Mitchell, D. L. et al. (1998). “Lunar surface magnetic fields and their interaction with the solar wind: Results from Lunar Prospector”. In: *Science* 281.5382, pp. 1480–1484.
- Nazarova, T. N., A. K. Rybakov, and C. D. Komissarov (1967). “Investigation of solid interplanetary matter in the vicinity of the moon”. In: *10th Plenary Meeting of COSPAR (London, England)*.
- Ness, N. F. et al. (1968). “Perturbations of the interplanetary magnetic field by the lunar wake”. In: *Journal of Geophysical Research* 73.11, pp. 3421–3440.
- Olhoeft, G. R., A. L. Frisillo, and D. W. Strangway (1974). “Electrical properties of lunar soil sample 15301, 38”. In: *Journal of Geophysical Research* 79.11, pp. 1599–1604.
- Oudayer, P. et al. (2019). “Multiscale modeling of dust charging in simulated lunar environment conditions”. In: *IEEE Transactions on Plasma Science* 47.8, pp. 3710–3716.
- Popel, S. I., L. M. Zelenyi, and B. Atamaniuk (2015). “Dusty plasma sheath-like structure in the region of lunar terminator”. In: *Physics of Plasmas* 22.12.
- Poppe, A. R. et al. (2021). “ARTEMIS observations of lunar nightside surface potentials in the magnetotail lobes: Evidence for micrometeoroid impact charging”. In: *Geophysical research letters* 48.15, e2021GL094585.
- Rhee, J. W., O. E. Berg, and H. Wolf (1977). “Electrostatic dust transport and Apollo 17 LEAM experiment.” In: *Space Research XVII*, pp. 627–629.
- Schwan, J. et al. (2017). “The charge state of electrostatically transported dust on regolith surfaces”. In: *Geophysical Research Letters* 44.7, pp. 3059–3065.
- Sickafoose, A. A. et al. (2001). “Experimental investigations on photoelectric and triboelectric charging of dust”. In: *Journal of Geophysical Research: Space Physics* 106.A5, pp. 8343–8356.
- Singer, S. F. and E. H. Walker (1962a). “Electrostatic dust transport on the lunar surface”. In: *Icarus* 1.1-6, pp. 112–120.

- (1962b). “Photoelectric screening of bodies in interplanetary space”. In: *Icarus* 1.1-6, pp. 7–12.
- Sonett, C. P., D. S. Colburn, and R. G. Currie (1967). “The intrinsic magnetic field of the moon”. In: *Journal of Geophysical Research* 72.21, pp. 5503–5507.
- Sow, Mamadou et al. (2013). “The role of humidity on the lift-off of particles in electric fields”. In: *Journal of the Brazilian Chemical Society* 24.2, pp. 273–279.
- Sridharan, R. et al. (2010). “Direct evidence for water (H₂O) in the sunlit lunar ambience from CHACE on MIP of Chandrayaan I”. In: *Planetary and Space Science* 58.6, pp. 947–950.
- Stern, S. A. (1999). “The lunar atmosphere: History, status, current problems, and context”. In: *Reviews of Geophysics* 37.4, pp. 453–491.
- Stubbs, T. J., R. R. Vondrak, and W. M. Farrell (2006). “A dynamic fountain model for lunar dust”. In: *Advances in Space Research* 37.1, pp. 59–66.
- Stubbs, T. J. et al. (2007). “Lunar surface charging: A global perspective using Lunar Prospector data”. In: *Dust in Planetary Systems* 643, pp. 181–184.
- Suggs, R. M. et al. (2008). “The NASA lunar impact monitoring program”. In: *Advances in Meteoroid and Meteor Science*, pp. 293–298.
- Szalay, J. R. and M. Horányi (2015). “The search for electrostatically lofted grains above the Moon with the Lunar Dust Experiment”. In: *Geophysical Research Letters* 42.13, pp. 5141–5146.
- Toth III, J. R. et al. (2017). “Particle-size-dependent triboelectric charging in single-component granular materials: role of humidity”. In: *Industrial & Engineering Chemistry Research* 56.35, pp. 9839–9845.
- Vanzani, V., F. Marzari, and E. Dotto (1997). “Micrometeoroid impacts on the lunar surface”. In: *Conference Paper, 28th Annual Lunar and Planetary Science Conference*, p. 481. Vol. 28, p. 481.
- Vasavada, A. R. et al. (2012). “Lunar equatorial surface temperatures and regolith properties from the Diviner Lunar Radiometer Experiment”. In: *Journal of Geophysical Research: Planets* 117.E12.
- Vaverka, J. et al. (2016). “Lunar surface and dust grain potentials during the earth’s magnetosphere crossing”. In: *The Astrophysical Journal* 825.2, p. 133.
- Walch, B., M. Horányi, and S. Robertson (1995). “Charging of dust grains in plasma with energetic electrons”. In: *Physical Review Letters* 75.5, p. 838.
- Walker, E. H. (1962). “Comments on a Paper by PD Grannis, ‘electrostatic Erosion Mechanisms on the Moon’”. In: *Journal of Geophysical Research* 67.6, pp. 2586–2587.
- Wang, X. et al. (2016). “Dust charging and transport on airless planetary bodies”. In: *Geophysical Research Letters* 43.12, pp. 6103–6110.
- Williams, J.-P. et al. (2017). “The global surface temperatures of the Moon as measured by the Diviner Lunar Radiometer Experiment”. In: *Icarus* 283, pp. 300–325.
- Wyatt, S. P. (1969). “The electrostatic charge of interplanetary grains”. In: *Planetary and Space Science* 17.2, pp. 155–171.
- Xu, S. et al. (2021). “Lunar photoemission yields inferred from ARTEMIS measurements”. In: *Journal of Geophysical Research: Planets* 126.6.

- Yakshinskiy, B. V. and T. E. Madey (2004). “Photon-stimulated desorption of Na from a lunar sample: Temperature-dependent effects”. In: *Icarus* 168.1, pp. 53–59.
- Yeo, L. H. et al. (2021). “Dynamics of electrostatically lofted dust on airless planetary bodies”. In: *Icarus* 366.
- Zook, H. A. and J. E. McCoy (1991). “Large scale lunar horizon glow and a high altitude lunar dust exosphere”. In: *Geophysical Research Letters* 18.11, pp. 2117–2120.
- Zook, H. A., A. E. Potter, and B. L. Cooper (1995). “The lunar dust exosphere and Clementine lunar horizon glow”. In: *Abstracts of the Lunar and Planetary Science Conference*. Vol. 26, p. 1577.

3 Lunar Regolith and its Simulants

The Moon's geological characteristics are nothing short of extraordinary. They not only shed light on the early history of planetary formation in our solar system but also serve as a record of Earth's history, as the Moon lacks the geological activity that continuously reshapes Earth's surface (Canup et al., 2001; Ringwood, 2012). Understanding lunar geology is crucial for planning and executing robotic and human missions. This knowledge will help us utilise potential resources such as water, minerals, and oxygen, as well as mitigate the risks inherent in lunar exploration.

This section will summarise lunar regolith properties and introduce the lunar regolith simulants used in this project.

3.1 Lunar Regolith

The term 'lunar regolith' describes the layer of loose rock material covering the entire lunar surface. 'Lunar soil,' on the other hand, refers to the finer-grained fraction of regolith, consisting of particles smaller than 1 cm. While these terms are often used interchangeably in the literature, this thesis primarily focuses on particles typically classified as soil. To maintain clarity and distinguish from the more common use of 'soil' in a non-lunar context, the term 'regolith' will be consistently used throughout. Lunar regolith is formed by meteorite impacts on the underlying bedrock, which break and pulverise the larger structures. The unique conditions on the Moon, characterised by the absence of oxygen, wind, and water, set lunar regolith apart from terrestrial regolith.

Lunar regolith is fine like powder but sharp like broken glass. Due to the atypical weathering on the Moon, particles created by micrometeoroid impacts remain rough and thus hazardous to humans and mission longevity. Measurements indicate that this layer consists of particles with varying sizes across different locations. Typically, the majority of lunar samples fall within the range of 45–800 μm (Heiken et al., 1991). Notably, particles smaller than 20 μm constitute approximately 20% of the total mass (Carrier III et al., 1991; McKay et al., 1991).

3.1.1 Locations and Geology

Even without the aid of sophisticated equipment, distinct darker and brighter regions on the Moon are discernible. The darker regions, known as 'maria' (singular

Table 3.1: A summary of major minerals on the Moon and those used in simulants.

Mineral	Description
Agglutinate	Particle that is an aggregate of smaller soil particles bonded together by vesicular, flow-banded glass that is created by melting in micrometeoroid impacts.
Anorthosite	Igneous rock predominantly (>90%) composed of plagioclase feldspar.
Basalt	Hard, dark, volcanic rock composed primarily of plagioclase, pyroxene, and olivine.
Breccia	A coarse-grained rock produced in impact fragmentation composed of angular rock fragments held together by a mineral cement or a fine-grained matrix.
Plagioclase feldspar	Aluminium-, calcium-, or sodium-rich silicate mineral, ranging from $\text{NaAlSi}_3\text{O}_8$ to $\text{CaAl}_2\text{Si}_2\text{O}_8$.
Pyroxene	Igneous and metamorphic rocks characterised by their monoclinic or orthorhombic crystal structure and typically containing iron, magnesium, and calcium silicates.

'mare' in Latin, meaning sea), contrast with the brighter areas referred to as 'highlands'. Maria, characterised by their flatness, were formed approximately 3.3–3.8 billion years ago when basins in these areas were filled with volcanic magma. In contrast, highlands are heavily cratered with hilly terrain, indicating their ancient origin around 4.5 billion years ago. The darker hue of the maria regions is attributed to their predominantly basaltic composition, formed by a rapid cooling of molten rock from extensive lava flows. Highlands primarily consist of Anorthosite, an igneous rock formed during volcanic activities but at a slower pace.

In addition to these prominent features, the Moon exhibits other geological characteristics such as lunar domes, lunar rilles, and lunar craters. However, this thesis focuses on two generalised simulants (see Section 3.2), representing the mare and highland regions, and therefore does not provide an exhaustive description of all lunar features.

3.1.2 Lunar Mineralogy

The lunar samples returned from Apollo (1969-1972) and Luna (1970-1976) sample-collecting missions have shown that lunar rocks are made up of minerals and glasses and the bulk composition varies between basaltic and anorthositic. The most abundant constituents are silicate minerals, making up over 90% by volume of most lunar rocks, these silicate minerals are pyroxene $(\text{Ca,Fe,Mg})_2\text{Si}_2\text{O}_6$ (8.5–61.1 vol.%), plagioclase feldspar $(\text{Ca,Na})(\text{Al,Si})_4\text{O}_8$ (12.9–69.1 vol.%) and olivine $(\text{Mg,Fe})_2\text{SiO}_4$ (0.2–17.5 vol.%) (Heiken et al., 1991). The next most abundant minerals are oxides, consisting of metals and oxygen, especially concentrated in the mare basalts, potentially comprising up to 20% by volume. These are ilmenite $(\text{Fe,Mg})\text{TiO}_3$ and

a complex series of spinel. Other materials such as native iron (Fe), silica, mare glass, highland glass and rare lunar minerals occur in small quantities but are nevertheless important and characteristic to the highly-reducing and low-oxygen lunar environment.

While the composition and mineralogy of lunar regolith display a level of uniformity when compared to terrestrial soil, the distribution and characteristics of the collected samples differ across the various locations (Vaniman et al., 1991). Figure 3.1 shows the sample return from the Apollo 11 mission. Apollo 11 landed in Mare Tranquillitatis, so many of the fragments are basalts.

Figure 3.2 shows Scanning Electron Microscope (SEM) images of single-grain regolith samples returned from various Luna missions. The surface morphologies of these lunar materials vary due to their distinct formation processes and compositions. Basalts, formed from ancient volcanic lava flows, have a relatively smooth texture. Plagioclase rocks, part of the Moon's original crust, solidified from the magma ocean and are typically lighter in colour with a more crystalline and fractured appearance due to their high aluminium and calcium content. Agglutinates, created by the welding of tiny rock and mineral fragments through micrometeorite impacts, exhibit a glassy, vesicular texture and a bubbly, porous appearance due to the melting and rapid cooling process.

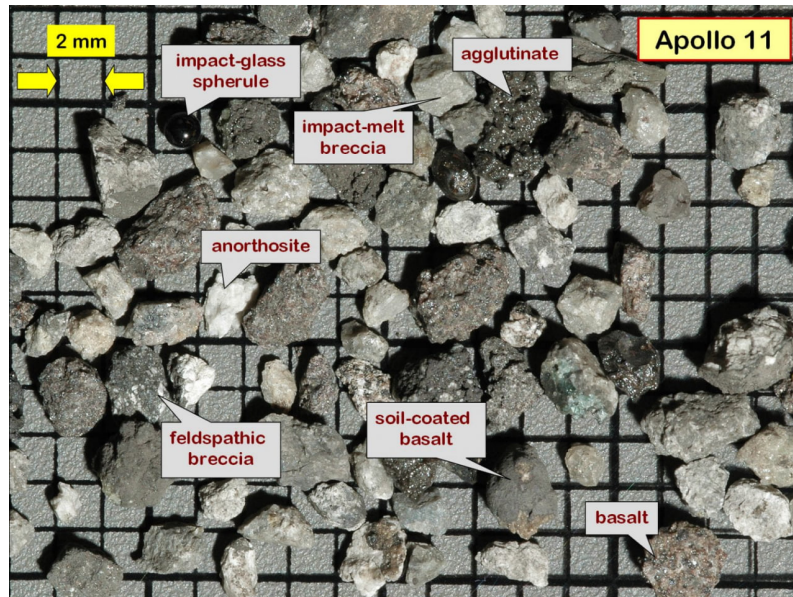


Figure 3.1: Rock fragments from the 2–4 mm grain size fraction of the Apollo 11 sample return. Many of the fragments are basalts. Impact glass spherules, agglutinates and regolith breccias, breccias from the feldspathic highlands (the lightest coloured fragments) are also shown. Source: St. Louis (n.d.), Randy Korotev.

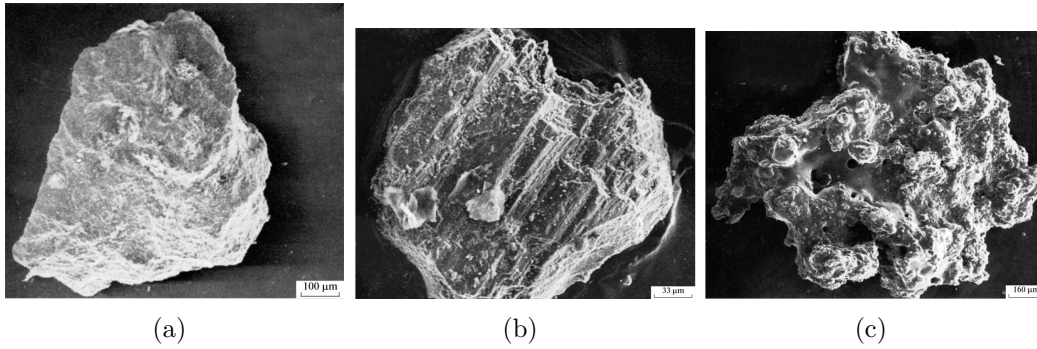


Figure 3.2: (a) Maria basalt fragment, Luna 16 return. (b) Highland plagioclase, Luna 20 return. (c) Agglutinate, Luna 16 return. The surface morphologies differ due to their formation processes and compositions. Source: Rode et al. (1979).

3.1.3 Type and Shape

Rocks on the lunar surface bear the marks of impact craters, spanning sizes from over 1000 kilometres to less than 1 micrometre in diameter. These craters originate from a variety of sources, ranging from large asteroids to minuscule cosmic dust particles, covering a wide spectrum of sizes. Despite the differences in their dimensions, both large and small impacts yield similar effects on the bedrock, including crater formation, shattering, melting, and dispersion of rock fragments.

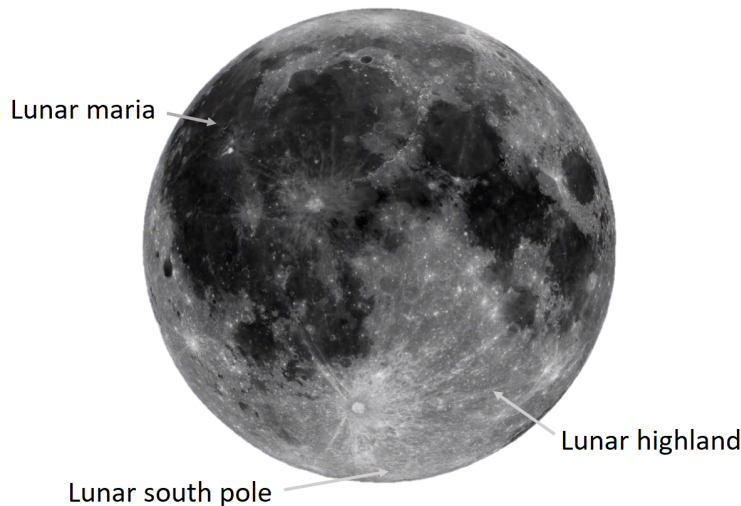


Figure 3.3: Typical regions of lunar mare and lunar highlands. Maria are characterised by their darker appearance due to a higher basalt content.

The lunar landscape can be broadly categorised into two main types: highlands and mare. Figure 3.3 shows the near side of the Moon and indicates typical regions of lunar maria and highland. Maria regions are darker and the highland regions are lighter. The mare basins were shaped by the impact of meteoroids and many were smoothed out when they became filled with basaltic lavas during the Moon's active volcanic period. Two types of lunar regolith lithologies, formed during mi-

cometeorite impacts, are agglutinates and glass spherules. Agglutinates arise when micrometeorites strike the lunar regolith, melting some of its material and producing a glassy substance embedded with mineral and rock fragments. Conversely, glass spherules form similarly, as products of micrometeorite impacts, but are molten glass ejected from a crater and solidify in their ejection trajectory. Some glass spherules were also created during the Moon's volcanic phase, often referred to as pyroclastic glass. When a rock contains either glass spherules or agglutinates, it is termed a *regolith breccia*; if it solely consists of fragmented material without these lithologies, it is simply referred to as a *fragmental breccia*.

3.1.4 Electrical Conductivity

The electrical conductivity of lunar regolith is one of the most important properties in the study of dust mitigation mechanisms involving electrostatic forces, yet it is also possibly the most elusive for experimental measurements. The electrical conductivity is found to be dependent on temperature for both terrestrial and lunar soil. In the lunar environment, where moisture is scarce, electrical conductivity is dominated by electronic and/or solid electrolytic mechanisms within the material. One study found that electrical conductivity becomes greater with increasing iron content (Schwerer et al., 1974), while the other suggests that semiconductor oxide minerals such as ilmenite and basic iron oxides found in lunar regolith contribute minimally to overall conductivity, as they are finely dispersed within the predominantly silicate matrix, and implied that the dominant mechanism for conduction is therefore ionic, which is very strongly controlled by external factors such as temperature, deviations from stoichiometry and electric field strengths (Tilley, 1975).

To predict the electrical tendencies and behaviours of particles, one needs to know very well, or at least have a reasonable range, of the volume resistivity of the material. This will give an indication of the likelihood of particles acquiring and dissipating charges. Insulating materials typically possess resistivities greater than $10^9 \Omega\text{m}$, leading them to accumulate significant amounts of charge during triboelectrification and retain this charge over extended periods (Buhler et al., 2007).

The typical method of measuring material resistivity involves placing the sample between two electrodes and apply a known voltage that corresponds to an expected range of resistivity values, and obtain a steady current readout. This is difficult for porous and irregular bulk granular materials such as the lunar regolith. Compactness, particles sizes, mineral distribution, only to name a few extremely difficult variables that one cannot hope to control nor reproduce for reliable measurements.

Studies on conductivity are not well understood, especially so within the context of amorphous rocks. Different sampling locations on the Moon also result in significant fluctuations in the overall conductivity; paths which a current is more likely to take within the material have determined to be the pyroxene or plagioclase phases*, although this can change with samples with a larger volume of metallic material

*Distinct states or forms of minerals and materials.

(Adler, 1970). The average bulk electrical conductivity of the Moon is calculated to be 7×10^{-4} S/m. Silicate-dominated lunar regolith has low electrical conductivity (10^{-14} to 10^{-9} S/m) (Olhoeft et al., 1974a; Carrier III et al., 1991). The wide range of values may be attributed to numerous factors, particularly in the case of crystalline structures where phase sizes (~ 0.3 mm) are comparable to the sample dimensions. Apollo returned samples exhibited exponentially temperature-dependent conductivity upon heating up to 500°C , where activation energy increases with temperature, and in this particular study by Olhoeft et al. (1974b), the two samples showed different conductivities, with one sharing data close to terrestrial pyroxene. Similar exponential temperature dependence has been observed in amorphous materials as well (Adler, 1971).

The electrical conductivity of lunar regolith increases exponentially as temperature increases, similar to that of a semiconductor (Olhoeft et al., 1974a). The electrical conductivity data obtained by Schwerer et al. (1971) for lunar and meteorite samples fit the expression

$$\sigma(T) = \sum_i \sigma_i^0 \exp(-E_i/kT) \quad (3.1)$$

where $\sigma(T)$ is the electrical conductivity with temperature, σ_i^0 are the prefactors in $(\Omega \text{ cm})^{-1}$, E_i are the activation energies in eV, k is the Boltzmann constant and T is the temperature in Kelvin. An Apollo 15 soil sample's conductivity was found to be of the relationship

$$\sigma_c = \sigma_{c0} e^{\alpha T} = 6 \times 10^{-18} e^{0.0237T} \text{ S/m} \quad (3.2)$$

where σ_{c0} is the experimentally determined electrical conductivity from Olhoeft et al. (1974a). Note that this relationship was obtained for temperatures between 300 and 1000 K.

During a typical lunar day, the effect of temperature on the dielectric properties is small over a range of temperatures (Chung et al., 1970; Chung et al., 1971; Olhoeft et al., 1975; Strangway et al., 1972). As Keilm et al. (1973) have shown that the temperature below a few centimeters of the lunar surface is constant regardless of the time of the lunar day, this implies that no change of dielectric properties will be observed at depth. During the lunar night, soil conductivity drops below 10^{-11} S/m at temperatures below 285 K. Using Equation 3.2 and a temperature near 100 K, the conductivity drops to below 10^{-14} S/m.

An instantaneous increase in surface conductivity was observed when the sample of a lunar breccia was exposed to a UV radiation of 235 nm, and adding visible and infrared radiations further increased the conductivity (Alvarez, 1975). This phenomenon is known as photoconductivity, which would mean that the lunar dayside may see a heightened conductivity compared to the rest of the Moon.

The relationship between dielectric permittivity ϵ and electrical conductivity σ is characterised by their responses to an electric field. More about regolith's dielectric properties in an electric field is discussed in the simulation Chapter 7.5.

3.2 Lunar Simulants

One of the first steps in conducting experiments began with the selection of an appropriate lunar regolith simulant. The simulant is a mixture of terrestrial materials artificially fabricated to enable researchers to conduct extensive testing of technologies for lunar applications with reproducibility and accessibility. These materials mimic the chemical and physical properties of real regolith to a certain extent. However, achieving a perfect simulant is unattainable for several reasons. Variations in mineral composition and particle size are not fully accounted for, as lunar regolith exhibits non-uniformity in its composition. Depending on the collection location, regolith can vary significantly.

We have come far from an assortment of homemade simulants since the first Moon return in 1969. There was a need for large quantities of simulants to conduct studies, so Johnson Space Center-1 (JSC-1) was manufactured in the US in 1994 (McKay et al., 1994), and Japan swiftly followed suit in 1998 (Kanamori et al., 1998). NASA maintains an extensive literature that regularly updates the simulant scene, including adding newly established simulants and refreshing older ones as necessary (Blewett et al., n.d.[a]; Blewett et al., n.d.[b]; A. Martin et al., n.d.).

Unique Lunar Regolith Properties

Replicating the natural conditions of lunar regolith particles on Earth is challenging. These conditions include meteoroid impacts that pulverise rocks into jagged, fine particles, the absence of weathering, which prevents surface erosion, and the effects of solar wind and radiation, which chemically alter and sputter the material, further shaping its morphology. Consequently, creating a simulant that accurately represents the full range of lunar regolith is difficult. No single simulant can meet all lunar-related research purposes.

Lunar regolith lacks clay or hydrated alteration minerals commonly found in Earth's rocks and soils. Most lunar simulants are prepared by air-drying the raw materials, a process that does not effectively remove volatile contaminants. As a result, experiments involving oxygen and water production using these simulants may overestimate production rates (Lomax et al., 2020). This also significantly impacts the discharging process in the context of electrostatics. Methods to minimise the effect of water are discussed in Section 6.2.

Although there are similar minerals on Earth, the magnetic and chemical properties of lunar minerals differ significantly. For example, magnetic beneficiation[†] techniques revealed that lunar ilmenite has similar magnetic susceptibility to pyroxene (paramagnetic), whereas terrestrial ilmenite is highly magnetic (Oder, 1991). Iron in the regolith exists as nanophase iron, which consists of nano-sized grains dispersed in the glass of impact-produced agglutinates. Agglutinates, comprising a major

[†]The process of improving the economic value of mined ore by removing impurities and concentrating valuable minerals.

component of lunar regolith (60–70%), contain many vesicles that increase surface area, potentially providing more sites for charge accumulation (Taylor, 2016).

3.2.1 Simulant Candidates

There are currently various lunar regolith simulants available for research. Several were tested during this project’s initial stages, including JSC-1A, TUBS-T, TUBS-M, LHS-1, LMS-1, and EAC-1. JSC-1A, similar to its predecessor JSC-1, was mined in Golden, CO. JSC-1 and JSC-1A are no longer commercially available, leading to their early disqualification for this project. TUBS-T and TUBS-M, developed by TU Braunschweig in Germany, were made exclusively of a single mineral of anorthosite and basalt, respectively. Their intended use was to be mixed to create site-specific mixtures, which is not ideal for research consistency. EAC-1, developed by the European Space Agency and sourced from the Siebengebirge Volcanic Field in Bonn, Germany, is also 100% basalt like TUBS-M. However, its availability is unclear as it is primarily for large-scale testing and technology maturation at the European Astronaut Centre.

Considering accessibility, recognition, variation, and quality, LHS-1 and LMS-1 from Exolith Lab, originating from the University of Central Florida, were chosen. The simulants are a mix of different simulants to match their corresponding lunar regolith compositions, the highlands and mare. At the time of simulant procurement, which was at the end of 2021, the company had only recently undergone some changes to the feedstocks used to create their simulants, and as of 2024, they had changed their formula twice, so the same name does not guarantee the same composition over time. Therefore, caution is advised when interpreting analysis reports, as older simulants may have been used in place of newer ones, and analyses conducted by different laboratories may yield slightly different results. Ideally, conducting one’s analysis with the current sample at hand would provide the most accurate insights, i.e. measure your own sample’s properties and characteristics.

3.2.2 Characteristics of LHS-1 and LMS-1

LHS-1, or Lunar Highlands Simulant 1, is designed to simulate the highlands regions of the Moon (Isachenkov et al., 2022). It is composed of a mixture of materials such as anorthosite, glass-rich basalt, ilmenite, pyroxene and olivine (Exolith Lab, 2022a). LMS-1, or Lunar Mare Simulant 1, is a simulant for the mare regions of the Moon, which are characterised by dark, smooth plains formed by ancient volcanic activity. LMS-1 is made up of the same minerals as LHS-1 but in different proportions, see Table 3.2 for comparison. Samples of LHS-1 and LMS-1 are shown in Fig. 3.4. Agglutinates make up a significant portion of lunar regolith, and Exolith Lab has a version of LHS-1 agglutinates (LHS-1-25A), created by applying a high temperature to a base material of 99% anorthosite and 1% iron powder, and the particles crushed to create the angular shape seen with real regolith. Note that the LHS-1-25A does not consist of simulated agglutinates, but basalt with a high glass content, which

consists of 25% simulated agglutinates by mass. Figures 3.5 and 3.6 show SEM images of the sieved simulant.

Mineralogy	LHS-1	LMS-1	LHS-1-25A
Anorthosite	74.4%	19.8%	80.6%
Glass-rich Basalt	24.7%	32.0%	18.5%
Ilmenite	0.4%	4.3%	0.3%
Iron	-	1.4%	0.3%
Pyroxene (Bronzite)	0.3%	32.8%	0.2%
Olivine	0.2%	11.1%	0.1%

Table 3.2: Mineralogical components of Lunar Regolith Simulants from Exolith Lab. LHS-1-25A being the agglutinated, higher-fidelity version of LHS-1 with an intermediate regolith maturity (Exolith Lab, 2022a; Exolith Lab, 2022b; ExolithLab, 2023).



Figure 3.4: (a) Sample of LHS-1. (b) Sample of LMS-1. Source: University of Central Florida.

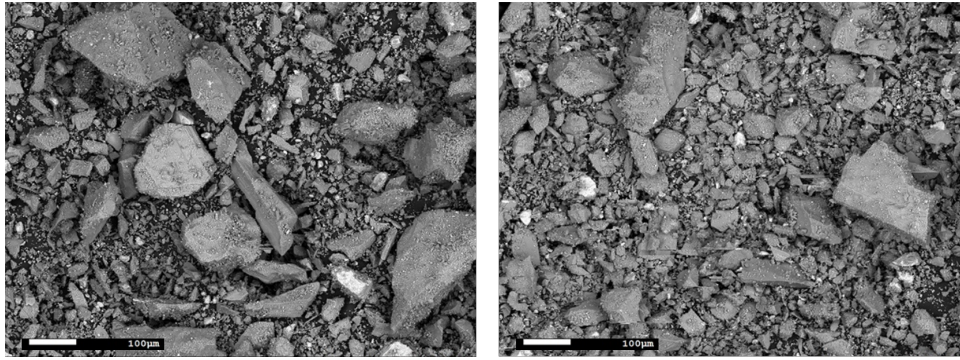


Figure 3.5: SEM images of Johnson Space Center-1 (JSC-1). The scale shown indicates 100 μm . Source: NASA JSC.

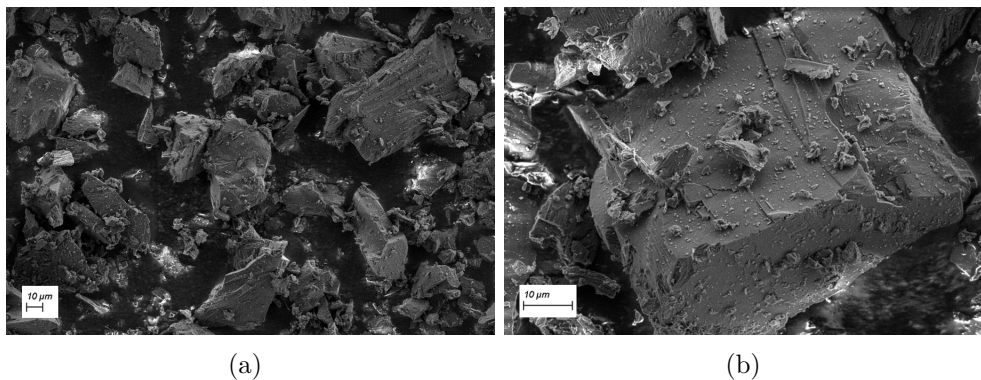


Figure 3.6: (a) SEM image of LHS-1. The particle size range is approximately 25–50 μm in diameter. Smaller particles are also present due to their adhesion to larger particles. (b) 3x more magnification as (a).

References

- Adler, D. (1970). “Electrical and optical properties of transition-metal oxides”. In: *Radiation Effects* 4.1, pp. 123–131.
- (1971). “Amorphous semiconductors”. In: *Critical Reviews in Solid State and Material Sciences* 2.3, pp. 317–465.
- Alvarez, R. (1975). “Lunar and terrestrial sample photoconductivity”. In: *Proceedings of the 6th Lunar Science Conference*. Vol. 6. New York, Pergamon Press, Inc., pp. 3187–3197.
- Blewett, D. T., J. T. S. Cahill, B. T. Greenhagen, et al. (n.d.[a]). “2020 Lunar Simulant Assessment”. In: ().
- Blewett, D. T. et al. (n.d.[b]). “2021 Lunar Simulant Assessment”. In: ().
- Buhler, C. R. et al. (2007). “In situ Test Method for the Electrostatic Characterization of Lunar Dust”. In: *IEEE Aerospace Conference*. KSC-2007-029.
- Canup, R. M. and E. Asphaug (2001). “Origin of the Moon in a giant impact near the end of the Earth’s formation”. In: *Nature* 412.6848, pp. 708–712.
- Carrier III, W. David, G. R. Olhoeft, and W. Mendell (1991). “Physical properties of the lunar surface”. In: *Lunar Sourcebook, A User’s Guide to the Moon*. Ed. by

- G. H. Heiken, D. T. Vaniman, and B. M. French. Cambridge University Press, pp. 475–594. ISBN: 978-0-521-33444-0.
- Chung, D. H., W. B. Westphal, and G. Simmons (1970). “Dielectric properties of Apollo 11 lunar samples and their comparison with earth materials”. In: *Journal of Geophysical Research* 75.32, pp. 6524–6531.
- (1971). “Dielectric behavior of lunar samples: Electromagnetic probing of the lunar interior”. In: *Proceedings of the Lunar Science Conference*. Vol. 2, p. 2381.
- Exolith Lab (2022a). *LHS-1 Spec Sheet*. <https://cdn.shopify.com/s/files/1/0398/9268/0862/files/lhs-1-spec-sheet-Dec2022.pptx.pdf?v=1688051876>. Accessed on February 27, 2024.
- (2022b). *LMS-1 Spec Sheet*. <https://cdn.shopify.com/s/files/1/0398/9268/0862/files/lms-1-spec-sheet-Dec2022.Updated.pdf>. Accessed on February 27, 2024.
- (2023). *Lunar Highlands Anorthosite (LHS-1-25A) Agglutinated Moon Dirt Simulant*. <https://exolithsimulants.com/collections/regolith-simulants/products/agglutinates>. Accessed: April 3, 2023.
- Heiken, G., D. T. Vaniman, and B. M. French (1991). *Lunar Sourcebook: A User’s Guide to the Moon*. 2nd. Cambridge, UK: Cambridge University Press. ISBN: 978-0-521-33444-0.
- Isachenkov, M. et al. (2022). “Characterization of novel lunar highland and mare simulants for ISRU research applications”. In: *Icarus* 376, p. 114873.
- Kanamori, H. et al. (1998). “Properties of lunar soil simulant manufactured in Japan”. In: *Space 98*, pp. 462–468.
- Keihm, S. J. and M. G. Langseth Jr (1973). “Surface brightness temperatures at the Apollo 17 heat flow site: Thermal conductivity of the upper 15 cm of regolith”. In: *Proceedings of the Lunar Science Conference*. Vol. 4, p. 2503.
- Lomax, B. A. et al. (2020). “Proving the viability of an electrochemical process for the simultaneous extraction of oxygen and production of metal alloys from lunar regolith”. In: *Planetary and Space Science* 180, p. 104748.
- Martin, A. and C. Wagoner (n.d.). “2022 Lunar Simulant Assessment”. In: ().
- McKay, D. S. et al. (1991). “The lunar regolith”. In: *Lunar Sourcebook, A User’s Guide to the Moon*. Ed. by G. H. Heiken, D. T. Vaniman, and B. M. French. Vol. 567. Cambridge University Press, pp. 285–356. ISBN: 978-0-521-33444-0.
- McKay, D. S. et al. (1994). “JSC-1: A new lunar soil simulant”. In: *Engineering, construction, and operations in space IV* 2, pp. 857–866.
- Oder, R.R. (1991). “Magnetic separation of lunar soils”. In: *IEEE Transactions on Magnetism* 27.6, pp. 5367–5370.
- Olhoeft, G. R., A. L. Frisillo, and D. W. Strangway (1974a). “Electrical properties of lunar soil sample 15301, 38”. In: *Journal of Geophysical Research* 79.11, pp. 1599–1604.
- Olhoeft, G. R. and D. W. Strangway (1975). “Dielectric properties of the first 100 meters of the Moon”. In: *Earth and Planetary Science Letters* 24.3, pp. 394–404.
- Olhoeft, G. R. et al. (1974b). “Temperature dependence of electrical conductivity and lunar temperatures”. In: *The Moon* 9.1, pp. 79–87.
- Ringwood, A. E. (2012). *Origin of the Earth and Moon*. Springer Science & Business Media.

- Rode, O. D. et al. (1979). *Atlas of Photomicrographs of the Surface Structures of Lunar Regolith Particles. Atlas mikrofotografii poverkhnosti chastits lunnogo regolita.* Dordrecht, Holland ; Boston: D. Reidel Publishing Co.
- Schwerer, F. C., T. Nagata, and R. M. Fisher (1971). “Electrical conductivity of lunar surface rocks and chondritic meteorites”. In: *The Moon* 2.4, pp. 408–422.
- Schwerer, F. C. et al. (1974). “Electrical conductivity of lunar surface rocks-Laboratory measurements and implications for lunar interior temperatures”. In: *Lunar Science Conference*. Vol. 5, pp. 2673–2687.
- St. Louis, Washington University in (n.d.). *Some Photos of Apollo Samples*. <https://sites.wustl.edu/meteoritesite/items/some-photos-of-apollo-samples/>. Accessed: 16-06-2024.
- Strangway, D. W. et al. (1972). “Electrical properties of lunar soil dependence on frequency, temperature and moisture”. In: *Earth and Planetary Science Letters* 16.2, pp. 275–281.
- Taylor, Stuart Ross (2016). *Lunar science: A post-Apollo view: Scientific results and insights from the lunar samples*. Elsevier.
- Tilley, R. J. D. (1975). *Nonstoichiometry, diffusion and electrical conductivity in binary metal oxides*.
- Vaniman, D. et al. (1991). “Exploration, samples, and recent concepts of the Moon”. In: *Lunar Sourcebook: A User’s Guide to the Moon*. Ed. by G. H. Heiken, D. T. Vaniman, and B. M. French. Vol. 5. New York: Cambridge University Press, pp. 5–26. ISBN: 978-0-521-33444-0.

4 Dust Mitigation Technologies and Mechanisms

4.1 The Dust Problem

During the Apollo missions, a significant amount of dust was brought into the lunar excursion module following each Extra Vehicular Activity (EVA). Despite great effort in removing the dust by the astronauts, dust persisted and remained inside the Extravehicular Mobility Unit (EMU)*. Subsequent Apollo missions that landed on the Moon (11, 12, 14, 15, 16, 17) unanimously reported dust-related problems, ranging from vision obscuration, clogged equipment, lost of traction, dust inhalation, equipment degradation, failed seals, false readings, and heavy wear of materials. All of these effects of lunar dust on EVA systems during the Apollo missions have been extensively documented by Gaier (2007).

Lunar regolith is not inherently toxic, but its composition and characteristics can pose several health risks. When they eventually would enter the command module via astronauts suits, these particles become aerosolised and causes irritation to the respiratory system when inhaled and penetrate deeply into the lungs. Long term exposure to lunar soil simulants has been shown to destroy lung and brain cells (Caston et al., 2018). In addition to that, lunar regolith possesses undesirable electrostatic properties for exploration. The combination of fine particles and electrostatics means the dust attaches to every surface its comes in contact with.

Just as with addressing terrestrial dust hazards, mitigation strategies on the Moon will also generally fall into three categories, characterised by 'ART': Avoid, Remove, and Tolerate, a nice mnemonic device delineated in NASA's latest lunar dust mitigation guide (Abel et al., 2023). This perspective is helpful when designing dust mitigation mechanisms and classifying various methods according to different mission scenarios. In an ideal world, the goal would be to completely *avoid* dust deposition or accumulation, but due to the pervasive and ubiquitous nature of dust, prevention efficiency is likely to be very limited. The most practical approaches therefore rely on dust *removal* and *tolerance*. This thesis focuses on one specific kind of dust removal technology, based on a 1972 "electric curtain" design, in order to repel charged dust particles off of a surface through the use of electric forces. The literature on dust mitigation re-views has been constantly updated throughout the last decades (Afshar-Mohajer et al., 2015; Cannon et al., 2022; Abel et al., 2023;

*EMU, consisting of the spacesuit, portable life support system, etc.

Zanon et al., (2023). This chapter will also provide brief overviews of additional technologies aimed at addressing the dust issue.

4.2 Active Dust Mitigation

Active methods for dust mitigation are typically defined as those using external forces, such as fluidal techniques, mechanical cleaning, and electrodynamic mechanisms. The challenges of cleaning dust within a pressurised lunar outpost or vehicle differ significantly from those in the external lunar environment. This study focuses on dust mitigation strategies pertinent to the exterior environment and this section is dedicated to examining current mitigation methods aimed for the open lunar environment.

Table 4.1 is an overview of a measurement system defined by NASA to assess the maturity of a technology, called Technology Readiness Level (TRL). TRL 1 is the lowest and TRL 9, where the system goes from a principle observation and scientific research to being 'flight proven' in a successful mission. This section will provide a brief overview of the various active dust mitigation mechanisms found in the literature, before delving into a detailed discussion of electrodynamic dust shield technology, which is the primary focus of this project.

TRL 9	Actual system "flight proven" through successful mission operations
TRL 8	Actual system completed and "flight qualified" through test and demonstration (ground or space)
TRL 7	System prototype demonstration in a space environment
TRL 6	System/subsystem model or prototype demonstration in a relevant environment (ground or space)
TRL 5	Component and/or breadboard validation in relevant environment
TRL 4	Component and/or breadboard validation in laboratory environment
TRL 3	Analytical and experimental critical function and/or characteristic proof-of-concept
TRL 2	Technology concept and/or application formulated
TRL 1	Basic principles observed and reported

Table 4.1: Technology Readiness Levels (TRL) definitions from NASA (2024). TRL 1 marks the initiation of scientific research, while TRL 9 indicates the technology's application in its final form under mission conditions.

Fluidal solutions are less common in space application due to a number of potential problems: the foams and gels in which the dust particles are intended to be suspended risk residues in addition to the unpredictability of liquid behaviour, and the immediate evaporation in vacuum. This is not to mention that during lunar night, these liquids would freeze. Application realisation would also pose a difficult design problem — do we spray or pour the solutions? These are just some of the many obstacles to overcome.

Other more commonly-seen methods such as the use of an adhesive or compressed gas to mechanically remove dust also come with their own downsides. While the adhesive itself might be a very neat approach, the disposal of a great amount of material goes against the ecosystem for sustainable space exploration in terms of use of storage and waste treatment. It would also be somewhat cumbersome to operate with gloved hands. Blowing compressed gas onto dust grains to overcome

adhesion is also a better option compared to wiping or brushing, but as with liquid, the direction in which gas will go in vacuum is not easy to control precisely, resulting in low efficiency for actual dust removal. Gas expansion also causes extreme temperature decrease, freezing the condensation on the appliances. A portable UV lamp integrated with a metal drill chassis has been proposed by Rhodes et al. (2020) to discharge triboelectrically-induced charges. This method is likely to be followed by shaking or agitating the surface to remove dust. Lastly, one method that might come as a surprise is exploiting the small amount of nanophase-iron (<1 wt%) to pick up regolith particles with a magnet. The presence of a thin (~ 100 nm) rind of glass containing np-iron on <50 μm size fraction of typical mare soil can be attracted and lifted by a simple magnet (Taylor et al., 2010).

Belden et al. (1991) summarise other methods and the design mentality that one should be equipped with when starting to consider dust mitigation in the space environment.

4.2.1 Electrostatic/Electrodynamic Methods

The predominant approach in this category is known as the Electrodynamic Dust Shield (EDS). It consists of parallel electrodes integrated into a thin dielectric material, connected to a voltage source. The potentials of these electrodes are oscillated with phases tuned to propagate an electric field wave down the curtain at a predetermined speed. The electrodes are connected to a multiphase high-voltage source at low-kilovolt and milliampere range. This source generates a travelling wave, which acts as a contactless conveyor, often referred to as the 'electric curtain'. It is based on the concept developed by Tatom et al. (1967) at Kennedy Space Center and was first suggested as a possible approach for lunar dust mitigation by (Adams et al., 1967). The operational concept relies on creating a strong, non-uniform, and time-varying electric field to exert electric forces in order to mobilise particles.

Principle of moving electric fields for transportation of particles was first outlined in the 1970s by (Masuda et al., 1972; Masuda et al., 1973) and the development of transparent electric curtains ('dust shields') for dust mitigation on solar panels is reported by (Mazumder et al., 2007). Transporting matters using uniform or non-uniform travelling fields have also been applied in other disciplines such as biology (Masuda et al., 1988; Moesner et al., 1997), which attests to the mechanism's efficacy. This method does not have any mechanical moving elements, making itself relatively simple hardware to maintain and conveniently, free from requiring a dust mitigation mechanism of its own.

Signal Type and Electrode Configuration

Square waves have been shown to be more effective at removing particles than sinusoidal waves (Sims et al., 2003) and this was also the chosen waveform to the EDS system designed in this project. The oscillation frequency of the high voltage

is low, on the order ranging between 10–100 Hz, as one of the the most important parameters to influence the dust removal rate was found to be the voltage. Higher frequency did not appear to correlate with higher cleaning capabilities (Sims et al., 2003). This finding was also observed during the preliminary parametric study of the setup in this project. Kawamoto et al. (2011b) found that the cleaning efficiency decreased with frequency, but becomes independent in low vacuum (except for <10 Hz). A Numerical simulation study by Gu et al. (2021) also found that particles move in the direction of the travelling wave at 10–50 Hz. At 200 Hz, they move backward, and at 500 Hz, they vibrate on their nearest same-polarity electrodes without horizontal movement. As described by time scale separation in electronic circuits, here the movement of particles occurs over longer time intervals compared to the much faster oscillation frequencies of electromagnetic waves, therefore these particles are considered quasi-static, which would simplify the analysis of the system, should one wish to do one.

Kawamoto et al. (2004) found that maximum electrostatic field when the width of the electrode is twice that of the pitch[†] ($p = 2w$). Jiang et al. (2020) found that thicker electrode tracks decrease the dust removing ability and suggested a 1 mm gap and 1 mm electrode width for optimal geometry, in agreement with the previous research.

Grain Size Effect

Another important factor in moving dust grains is the grain size itself. Simulation results indicated that both leap height and horizontal velocity of particles increased with diameters ranging from 0.03–0.1 mm. Unsurprisingly, higher charge densities significantly enhanced particle leap height and transport speed as well (Gu et al., 2021). Lunar gravity might yield slightly different outcome, but it should be favourable for dust mitigation purposes.

Material Degradation

Exposed EDS tracks are prone to degradation from the harsh radiation and abrasive particles (Schaible et al., 2023). Fortunately, the EDS is not intended to be used uncoated, and applying a thin dielectric material coating is sufficient to increase the breakdown voltage up to kV. There are variations of the EDS design specific to different applications. NASA’s Kennedy Space Center has developed several EDS configurations, as shown in Figure 4.1: copper/Kapton configuration is designed to be coated with thermal paint and attached to spacecraft thermal radiators, silver/fluorinated ethylene propylene shields for thermal radiators but do not require thermal paint, and a carbon nanotube/fabric configuration for space suits, where astronauts noted substantial dust adhesion. Apollo astronauts also identified scarred visors and other optical equipment from the abrasive lunar dust. Indium Tin Oxide (ITO) is a common material for use as an electrode for its transparency, it can be

[†]Pitch distance refers to the center-to-center spacing between adjacent leads.

applied with nanometer thickness, making it practically transparent in applications where full visibility is required, such as solar panels, viewports, astronaut visors and camera lenses, etc. Other advantages include excellent electrical conductivity, thermal stability, durability, smooth surface and ease of integration with other materials.

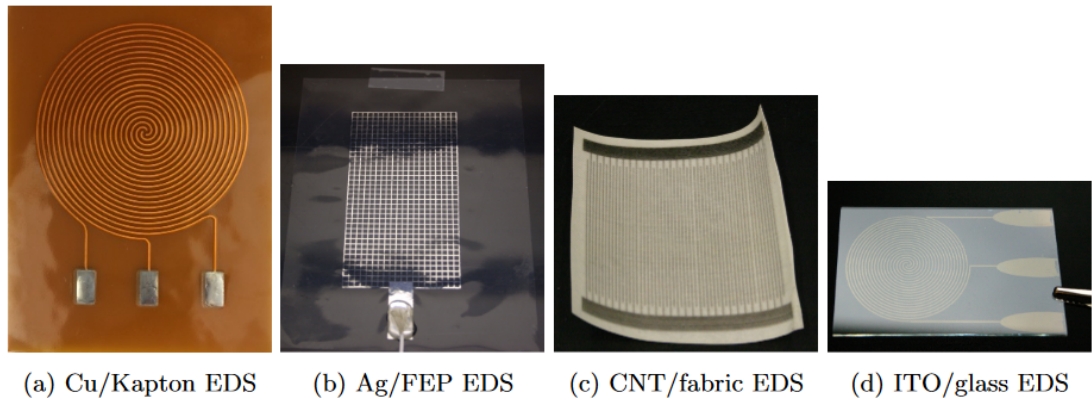


Figure 4.1: The different combinations of substrate/coating materials and electrode patterns for EDS tailored for various applications, depending on the equipment and requirements, such as solar panel, thermal radiator and astronaut suit, etc. Source: (Johansen, 2015).

Material properties, especially the degradation rate under prolonged UV exposure, are important parameters to study and explore. NASA has studied and is continuing the study of this matter with experiments on the ISS. The NASA Materials International Space Station Experiment X (MISSE-X) mission on the International Space Station (ISS) provided a platform to study material behaviour in exposure to the space radiation environment. C. I. Calle et al. (2013) reported on the EDS performance for optical systems and thermal radiators. Both results showed effective cleaning efficiencies (Figure 4.2). A panel of different active and passive samples on the EDS experiment was subjected to the low-Earth-orbit space environment, and placed in the wake position of the ISS to simulate lunar conditions again in on MISSE-11 in 2019. As of a published report in 2020, the technology stands at TRL 8 (Buhler et al., 2020), which is the most developed post-Apollo technology that reached TRL 8, where other technologies ranked only at most to TLR 5 (Zanon et al., 2023). This mission included a variety of materials, such as thermal radiators, lotus-leaf coatings, and prototype spacesuit fabric (Johansen et al., 2019). Most panels were not connected to power to test for material degradation, while those connected were supplied with 4 kV amplitude, 10 Hz frequency square-wave signals. Preliminary results show that the hardware performed as expected. Additional EDS panels were sent to the ISS with the MISSE-15 mission in 2021, which is still active, and data from this mission is yet to be analysed.

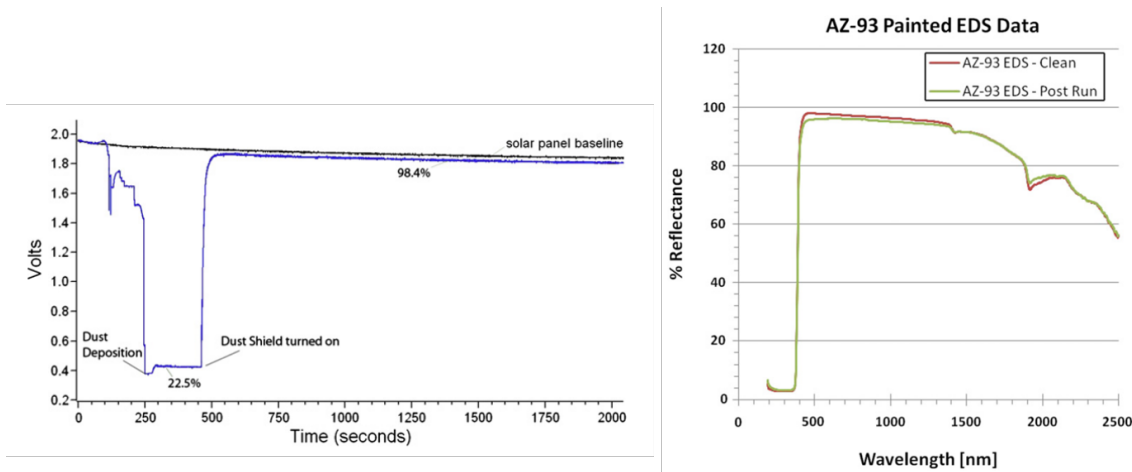


Figure 4.2: Results from the MISSE-X mission testing the durability and performance of materials. Left: Solar panel response over time, with dust deposition beginning at approximately 150 seconds and EDS activation at around 450 seconds. Right: Reflectance spectra of a solid thermal radiator, showing that the cleaned surface (green) exhibits similar reflectance data as the uncontaminated radiator surface. Source: C. I. Calle et al. (2013).

Dust Charging Mechanisms

As discussed in Section 2.2.2, the EDS's effectiveness could be enhanced by the natural conditions on the Moon, such as the plasma environment. C. I. Calle et al. (2006) and C. I. Calle et al. (2009) introduced the theoretical framework for use in extra-terrestrial applications and C. I. Calle et al. (2011) experimentally showed the design of NASA's EDS technology under a partially-simulated lunar environment. Farr et al. (2020) discussed the use of an electron beam to clean dusty spacecraft and spacesuit surfaces based on recent studies of secondary electron build-up inside microcavities between dust particles, which can lead to substantial negative charges, generating a sufficiently strong inter-particle Coulomb force to liberate particles from the surface. Operating at an inclination, the surface was able to reach a cleanliness rate up to 75-85% on ~ 100 sec timescale.

EDS on Photovoltaic Panels

The lack of wind and rain, coupled with weak gravity, prevents dust particles from being effectively removed through natural weathering processes. Other mechanisms, such as rotating large solar cell arrays to dislodge dust particles, are not only mechanically disadvantageous — due to potential wear and tear on the joints — but also inefficient in terms of energy expenditure relative to the minimal results achieved. Mechanical means are both potentially damaging and inefficient, as the abrasive nature of the dust particles will create irreversible deterioration to the material as they are dragged across the surface.

Vibration and ultrasonic cleaning have been studied for solar panels and thermal regulators (Williams et al., 2007; Joyce et al., 2022) and is a non-invasive method which has much potential. Follow-up studies have given experimental data on the performance characteristics of solar panels covered by dust shields with Martian and lunar stimulants (C. Calle et al., 2008; Sharma et al., 2009). There is extensive research done on terrestrial solar cell array cleaning, which are not limited to electrostatic- or electrodynamic-based (He et al., 2011). Not all of these mechanisms will be viable on the Moon, and electrostatic/electrodynamic has become the clear favourite over the years due to its high dust removal rate.

4.2.2 EDS Performance in Literature

Table 4.2 lists some of the published experimental studies on the EDS system relevant to lunar applications. The setup, namely the sandwich configuration of substrate-electrode-coating (see Figure 6.2), should be comparable to the setup shown in this thesis. Studies on EDS application in Martian environments are intentionally excluded due to the significantly different surface properties of Mars. The studies included here vary in their environmental conditions; this table aims to highlight these differences.

The type of dust mitigation technique should be tailored to the surface from which it aims to remove dust. There are variations of the flat EDS screen, just to name a few: electrostatic lunar dust repeller (Afshar-Mohajer et al., 2014), EDS for mechanical seals (Kawamoto, 2014), self-cleaning spacesuits using carbon nanotube (Manyapu et al., 2017; Manyapu et al., 2019). Using a similar travelling wave principle, Kawamoto et al. (2011a) incorporated stitched wire electrodes into the insulating fabric of spacesuits and achieved a cleaning rate above 80% in vacuum, in combination with mechanical vibration (Figure 4.3). Similarly, Manyapu et al. (2019) (Figure 4.4) embedded conductive carbon nanotube yarns into the outer layer of the spacesuit to achieve a comparable effect. The advantage of using a more robust electrode material is its higher mechanical strength, which allows it to withstand the repeated motions of astronaut activities that can cause significant fatigue in many materials. However, this configuration does expose the cables directly to the harsh radiation environment.

4.3 Passive Dust Mitigation

The passive approach to mitigating dust would fit into the prevention category, and would be applicable across various devices and equipment surfaces. Typically, this approach entails altering the surface structure to minimise initial dust adhesion, or simply supplying mechanical shields/seals to stop dust from landing on critical areas in the first place. The former being a lot more nuanced, its mechanism entails enhancing the surface roughness to reduce the area of contact with particles, or chemically treating the surface to lower its surface energy. Researches so far indi-

cate that passive dust mitigation strategies for lunar environments should prioritise reducing electrostatic adhesion.

Materials that share the same work functions are expected to charge to the same potential, and the closer the work functions are, the less adhesion should occur. This can however, only serve to mitigate dust adhesion to a certain extent, as realistically this is not the only factor at play for adhesion; other reasons include electrostatic potential or differential potential. Amorphous fluorocarbon has shown to protect surfaces from molecular and particulate contamination (Crowder et al., 2008). An ion beam process can be used to reduce the surface energy of semiconductors and insulating materials such as silicon and quartz (Dove et al., 2011)

As will be discussed in Section 5.2, there are a multitude of material characteristics that would alter the charging behaviour, so one cannot hope that, with the non-monodisperse in size, irregularly-shaped, non-homogeneous in chemical makeup lunar regolith, the work function matching method alone is sufficient. It should be noted that in literature, the work function of lunar regolith simulant, specifically that of JSC-1A, has found to be between 5.4 (Walton, 2007) and 5.9 eV (Trigwell et al., 2009).



Figure 4.3: Insulated wire electrodes embedded in a spacesuit material, from Kawamoto et al. (2011a).

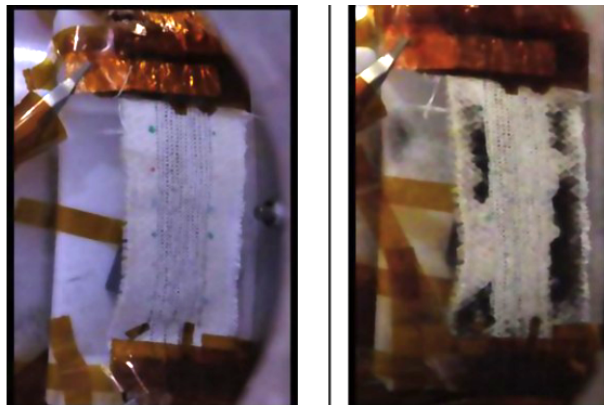


Figure 4.4: Carbon nanotube yarns in a spacesuit material from Manyapu et al. (2019), showing before and after dust cleaning.

Table 4.2: Summary of studies on lunar EDS technology tested on a rigid substrate with a thin dielectric coating of plastic, epoxy, thermal paint, or thin nano-material.

Researcher	EDS Coating	Atmospheric condition(s)	Simulant	Size Range	Simulant Drying	Methodology
C. I. Calle et al. (2006)	Polyurethane on transparent PET	Normal and CO ₂ atmosphere	JSC Mars-1	2–6 μm and 8–15 mm	At 100°C for at least 24 hours	Corona charger and a charge neutraliser. EDS test for uncharged, charged, and neutralised particles. 750–1250 V at 4 Hz, 30 s.
C. I. Calle et al. (2009)	Epoxy on glass	10 ⁻⁵ mbar	JSC-1A	50–75 μm	Baked for several days	Reduced gravity for optical systems.
C. I. Calle et al. (2010)	AZ-93 thermal paint on polyimide sheet	Air and 5 \times 10 ⁻⁷ mbar	JSC-1A	50–100 μm	Dried at 10 ⁻⁶ mbar	1–2 kV square waves at 10 Hz for thermal radiators.
Kawamoto et al. (2011b)	Epoxy on glass	Air and 5 \times 10 ⁻² mbar	FJS-1	<30 μm	Unbaked	800 V for 60 sec, with ultrasonic vibration.
Schaible et al. (2023)	CMrGO ¹ on HDPE ² substrate	10 ⁻⁶ mbar	LHS-1	<500 μm	Unbaked	1–3 kV at 10 Hz for 5 mins on 2-phase and 3-phase EDS, with UV illumination at 172 nm.

^a Chemically modified reduced graphene oxide.^b High-density polyethylene.

4.4 Implicit Dust Mitigation

This branch of dust mitigation technology is somewhat difficult to categorise, but could be the bridging approach between active and passive mechanisms by eliminating the need to deal with dust in the first place. This is where compliant mechanism shines as the alternative approach that could provide resilience in dust-related jamming in machine joints. Electrodynamic mechanisms can partially be deemed to fall under this category, however, it has already been extensively discussed under the active dust mitigation section.

Instead of using the traditional rigid-body hinge which comprises of multiple elements with a connecting part, compliant mechanisms consist of a single piece with an elasticity which allows movement. This removes the gaps and regular lubrication which allow dust to enter and foul the hinge mechanism. In compliant mechanisms, the part can return to its original shape much like a spring. Budzyń et al. (2023) explains the feasibility of using this technique in lunar equipment. As with all dust mitigation technologies, this application is also not without its limitations. The components featuring compliant mechanisms can still be subject to surface abrasion and other wear related to dust accumulation. In addition, while mechanical failure due to dust jamming might be reduced, the maintenance and regular component replacement could be necessary, as the material could be less resilient to the harsh lunar environment and the constant bending makes them more prone to fatigue damage. Undergoing research for reliable and long-lasting compliant mechanism design is ongoing, but the inter-disciplinary considerations involved renders this technology difficult to manufacture. The use of compliant mechanisms in space-related applications has been limited so far and has yet to be included in any mission. The use would usually be located in scientific payloads (Dougherty, 2003; Henein et al., 2004) or for hardware design (Howell et al., 2013; Zhang et al., 2018; Fowler et al., 2011).

References

- Abel, P. B. et al. (2023). *Lunar Dust Mitigation A Guide and Reference First Edition (2021)*. Tech. rep.
- Adams, J. G. et al. (1967). *Lunar dust degradation effects and removal/prevention concepts. volume 2-detailed results final report*. Tech. rep.
- Afshar-Mohajer, N. et al. (2014). “Design of an electrostatic lunar dust repeller for mitigating dust deposition and evaluation of its removal efficiency”. In: *Journal of Aerosol Science* 69, pp. 21–31.
- Afshar-Mohajer, N. et al. (2015). “Review of dust transport and mitigation technologies in lunar and Martian atmospheres”. In: *Advances in Space Research* 56.6, pp. 1222–1241.
- Belden, L. et al. (1991). *Design of equipment for lunar dust removal*. Tech. rep.
- Budzyń, D. et al. (2023). “Implicit lunar dust mitigation technology: Compliant mechanisms”. In: *Acta Astronautica* 203, pp. 146–156.

- Buhler, C. R. et al. (2020). “Current state of the electrodynamic dust shield for mitigation”. In: *The Impact of Lunar Dust on Human Exploration Workshop*.
- Calle, C. et al. (2008). “Dust particle removal by electrostatic and dielectrophoretic forces with applications to NASA exploration missions”. In: *Proc. ESA Annual Meeting on Electrostatics*. Vol. 2008. ESA Minneapolis, MN.
- Calle, C. I. et al. (2006). “Electrodynamic dust shield for surface exploration activities on the moon and Mars”. In: *57th International Astronautical Congress conference*. KSC-2006-125.
- Calle, C. I. et al. (2009). “Particle removal by electrostatic and dielectrophoretic forces for dust control during lunar exploration missions”. In: *Journal of Electrostatics* 67.2-3, pp. 89–92.
- Calle, C. I. et al. (2010). “Active dust mitigation technology for thermal radiators for lunar exploration”. In: *Earth and Space 2010: Engineering, Science, Construction, and Operations in Challenging Environments*, pp. 13–20.
- Calle, C. I. et al. (2011). “Active dust control and mitigation technology for lunar and Martian exploration”. In: *Acta Astronautica* 69.11-12, pp. 1082–1088.
- Calle, C. I. et al. (2013). “Electrodynamic dust shields on the international space station: Exposure to the space environment”. In: *Journal of Electrostatics* 71.3, pp. 257–259.
- Cannon, K. M. et al. (2022). “Working with lunar surface materials: Review and analysis of dust mitigation and regolith conveyance technologies”. In: *Acta Astronautica* 196, pp. 259–274.
- Caston, R. et al. (2018). “Assessing toxicity and nuclear and mitochondrial DNA damage caused by exposure of mammalian cells to lunar regolith simulants”. In: *GeoHealth* 2.4, pp. 139–148.
- Crowder, M. S. and C. Haley (2008). “Mitigating molecular and particulate contamination via surface energy”. In: *Optical System Contamination: Effects, Measurements, and Control 2008*. Vol. 7069. SPIE, pp. 82–90.
- Dougherty, S. (2003). “Micro-imager dust cover, micro-imager contact sensor, and Mössbauer spectrometer contact sensor mechanisms for the Mars Exploration Rovers”. In: *10th European Space Mechanisms and Tribology Symposium*. Vol. 524, pp. 73–80.
- Dove, A. et al. (2011). “Mitigation of lunar dust adhesion by surface modification”. In: *Planetary and space science* 59.14, pp. 1784–1790.
- Farr, B. et al. (2020). “Dust mitigation technology for lunar exploration utilizing an electron beam”. In: *Acta Astronautica* 177, pp. 405–409.
- Fowler, R. M., L. L. Howell, and S. P. Magleby (2011). “Compliant space mechanisms: a new frontier for compliant mechanisms”. In: *Mechanical Sciences* 2.2, pp. 205–215.
- Gaier, J. R. (2007). *The effects of lunar dust on EVA systems during the Apollo missions*. Tech. rep.
- Gu, J. et al. (2021). “Numerical study of particle transport by an alternating travelling-wave electrostatic field”. In: *Acta Astronautica* 188, pp. 505–517.
- He, G., C. Zhou, and Z. Li (2011). “Review of self-cleaning method for solar cell array”. In: *Procedia Engineering* 16, pp. 640–645.

- Henein, S. et al. (2004). “Mechanical slit mask mechanism for the James Webb Space Telescope spectrometer”. In: *Optical, Infrared, and Millimeter Space Telescopes*. Vol. 5487. SPIE, pp. 765–776.
- Howell, L. L. et al. (2013). *Handbook of compliant mechanisms*. Wiley Online Library.
- Jiang, J. et al. (2020). “An optimization dust-removing electrode design method aiming at improving dust mitigation efficiency in lunar exploration”. In: *Acta Astronautica* 166, pp. 59–68.
- Johansen, M. R. (2015). “History and flight development of the electrodynamic dust shield”. In: *AIAA Space 2015 Conference and Exposition*, p. 4446.
- Johansen, M. R. et al. (2019). “Electrodynamic Dust Shield Testing on the Materials on International Space Station Experiment 11”. In: *International Astronautical Congress (IAC)*. IAC-19, C2, 6, 2, x54303.
- Joyce, C. and R. Kobrick (2022). “Modal Optimized Vibration dust Eliminator (MOVE): An Active/Passive Dust Mitigation Technology for Spaceflight Exploration”. In: 51st International Conference on Environmental Systems.
- Kawamoto, H. (2014). “Improved electrostatic shield for lunar dust entering into mechanical seals of equipment used for long-term lunar exploration”. In: 44th International Conference on Environmental Systems.
- Kawamoto, H. and N. Hara (2011a). “Electrostatic cleaning system for removing lunar dust adhering to space suits”. In: *Journal of Aerospace Engineering* 24.4, pp. 442–444.
- Kawamoto, H. and N. Hasegawa (2004). “Traveling wave transport of particles and particle size classification”. In: *Journal of Imaging Science and Technology* 48.5, pp. 404–411.
- Kawamoto, H. et al. (2011b). “Mitigation of lunar dust on solar panels and optical elements utilizing electrostatic traveling-wave”. In: *Journal of Electrostatics* 69.4, pp. 370–379.
- Manyapu, K. K., L. Peltz, and P. De Leon (2019). “Self-cleaning spacesuits for future planetary missions using carbon nanotube technology”. In: *Acta Astronautica* 157, pp. 134–144.
- Manyapu, K. K. et al. (2017). “Proof of concept demonstration of novel technologies for lunar spacesuit dust mitigation”. In: *Acta Astronautica* 137, pp. 472–481.
- Masuda, S. and Y. Matsumoto (1973). “Theoretical characteristics of standing-wave electric curtains”. In: *Electrical Engineering in Japan* 93.1, pp. 71–77.
- Masuda, S., M. Washizu, and I. Kawabata (1988). “Movement of blood cells in liquid by nonuniform traveling field”. In: *IEEE Transactions on Industry Applications* 24.2, pp. 217–222.
- Masuda, S. et al. (1972). “Confinement and transport of charged aerosol clouds by means of electric curtains”. In: *The transactions of the Institute of Electrical Engineers of Japan* 92.1, pp. 9–18.
- Mazumder, M. K. et al. (2007). “Self-cleaning transparent dust shields for protecting solar panels and other devices”. In: *Particulate Science and Technology* 25.1, pp. 5–20.
- Moesner, F. M. and T. Higuchi (1997). “Traveling electric field conveyor for contactless manipulation of microparts”. In: *IAS '97. Conference Record of the 1997 IEEE*

- Industry Applications Conference Thirty-Second IAS Annual Meeting*. Vol. 3, 2004–2011 vol.3.
- NASA (2024). *Technology Readiness Levels*. Accessed: 28.05.2024. URL: <https://www.nasa.gov/directorates/somd/space-communications-navigation-program/technology-readiness-levels/>.
- Rhodes, D. J., W. M. Farrell, and J. L. McLain (2020). “Tribocharging and electrical grounding of a drill in shadowed regions of the Moon”. In: *Advances in Space Research* 66.4, pp. 753–759.
- Schaible, M. J. et al. (2023). “Performance of chemically modified reduced graphene oxide (CMrGO) in lunar electrodynamic dust shield (EDS) applications”. In: *Acta Astronautica* 211, pp. 674–683.
- Sharma, R. et al. (2009). “Experimental evaluation and analysis of electrodynamic screen as dust mitigation technology for future Mars missions”. In: *IEEE Transactions on Industry Applications* 45.2, pp. 591–596.
- Sims, R. A. et al. (2003). “Development of a transparent self-cleaning dust shield for solar panels”. In: *Proceedings ESA-IEEE joint meeting on electrostatics*. Vol. 814, pp. 1–8.
- Tatom, F.B. et al. (1967). *Lunar Dust Degradation Effects and Removal/prevention Concepts*. NASA contractor report. Nortronics, Northrop Corporation. URL: <https://books.google.nl/books?id=k2QKzweACAAJ>.
- Taylor, L. A. and Y. Liu (2010). “Important considerations for lunar soil simulants”. In: *Earth and Space 2010: Engineering, Science, Construction, and Operations in Challenging Environments*, pp. 106–118.
- Trigwell, S. et al. (2009). “The use of tribocharging in the electrostatic beneficiation of lunar simulant”. In: *IEEE Transactions on Industry Applications* 45.3, pp. 1060–1067.
- Walton, O. R. (2007). “Adhesion of lunar dust”. In: *NASA*.
- Williams, R. B. et al. (Apr. 2007). “Vibration Characterization of Self-Cleaning Solar Panels with Piezoceramic Actuation”. In: *48th AIAA/ASME/ASCE/AHS/ASC Structures, Structural Dynamics, and Materials Conference*. AIAA Paper 2007-1746, p. 1746.
- Zanon, P., M. Dunn, and G. Brooks (2023). “Current Lunar dust mitigation techniques and future directions”. In: *Acta Astronautica*.
- Zhang, X. and B. Zhu (2018). *Topology optimization of compliant mechanisms*. Springer.

5 Forces on Dust grains in an EDS System

Along the horizontal axis, forces such as friction and adhesion come into play, affecting lateral motion. Along the vertical axis, gravity and adhesion are the primary factors governing vertical movement. However, with the presence of charge, particles experience an additional force that can act in any direction.

The ability of the electrostatic force to induce dust uplift has been studied in relation to various adhesive forces and gravity, both experimentally and by modelling in various environments and applications (Sickafoose et al., 2002; Abbas et al., 2007; Poppe et al., 2010; Hartzell et al., 2011; X. Wang et al., 2016; Champlain et al., 2016). The non-uniform electric field generated by the EDS system may also induce a dielectrophoretic force on dielectric particles. While this force could aid in mobilising grains, its impact is likely minor compared to the Coulomb force at play (Pohl, 1951; Calle et al., 2006; Liu et al., 2010).

This section will discuss the phenomena significant to the operation of the EDS system under simulated lunar conditions, primarily influenced by the interaction of electrostatic forces with the electric field. These include tribocharging and UV charging, the latter of which is extensively discussed in Section 2.2.1. Additionally, a brief theoretical discussion on the debated dielectrophoretic force is presented, followed by a simulation-based approximation in a later section.

5.1 Non-Electrostatic Adhesion

There are generally five forces responsible for particle adhesion: van der Waals forces, mechanical interlocking, chemical bonding, electrostatic forces and capillary forces. In the lunar context, capillary forces are virtually non-existent due to the vacuum and lack of moisture in general. These short-range interactions are challenging to measure experimentally and the exact mechanism is difficult to determine. The evaluation of the adhesive force between two surfaces requires information on geometry and properties of surrounding medium.

The regolith particles are not smooth spheres, but the area near the contact point can be approximated as a smaller radius half-sphere. Taking the mass density of the particles as 2.4 g/cm^3 , the adhesive force for particles with sizes less than $50 \mu\text{m}$ obtained by Izvekova et al. (2013) is found to exceed lunar gravity. Comparing their

results from Hamaker (1937), increasing surface roughness reduces the adhesion force by two to three orders of magnitude, a result also confirmed by Rajupet et al. (2021). They also found that the electrostatic forces are only slightly diminished with increasing roughness, and in some cases even enhanced by the irregularities in the material. For polarisable particles contacting a rough conducting surface, electrostatic forces can dominate adhesion for particles sizes as small as around 1–10 μm . The electrostatic force, whether it is attractive or repulsion, stems from tribocharging when there are no external charging mechanisms. The magnitude of tribocharging is difficult to estimate and relies on information related to the material’s dielectric properties and surface charge density. The electrostatic force applied by the EDS is given by

$$\mathbf{F}_e = q\mathbf{E} \quad (5.1)$$

where q is the charge of a dust grain and \mathbf{E} is the electric field.

Consider first the adhesion forces between two infinite and flat surfaces. The van der Waals force per area a is given by $F_V/a = H/6\pi d^3$ (Israelachvili, 2011) and the electrostatic force per area is given by $F_E/a = \sigma^2/2\epsilon_0$ (Hays, 1995), where H is the Hamaker constant, σ the surface charge density, ϵ_0 the vacuum permittivity and d the surface separation. Hamaker’s constant is a physical constant that characterises the van der Waals interactions between two spheres at a microscopic level that considers only the material properties, and is used as an estimation for predicting interactions in nanoscale systems. The Hamaker constant for lunar regolith is 4.3×10^{-20} J (Perko et al., 2001). When we observe the more relevant case of a particle-surface interaction, the van der Waals force on a spherical particle with radius R , d distance away is given by (Israelachvili, 2011):

$$F_V = \frac{HR}{6d^2} \quad (5.2)$$

The electrostatic force for a non-polarisable sphere with radius R and uniform surface charge density σ interacting with a smooth conducting surface is given by:

$$F_E = \frac{\pi\sigma^2 R^4}{\epsilon_0(d+R)^2} \quad (5.3)$$

Substituting typical values into the equations, one would find that van der Waals is generally many times larger than the electrostatic force for both cases and would render the latter negligible. However, these equations are idealised cases of perfectly smooth surfaces and it neglects the polarisability of the particle material; various studies have shown that surface roughness can greatly diminish van der Waals forces (Krupp, 1967; Tabor, 1977; Rabinovich et al., 2000; Ramakrishna et al., 2011). This aligns with the typical behaviour of van der Waals forces, which weaken rapidly as the distance between surfaces increases, particularly when there are larger surface irregularities.

5.2 Tribocharging

Tribocharging, or contact electrification, is a phenomenon in which surfaces come into contact and exchange electrons due to their difference in energy levels. Electrons migrate from a material with a lower work function to one with a higher work function until energy equilibrium is established (Sternovsky et al., 2002). The process thereby gives one material a net positive charge and the other a negative one. The contact charging of metals is directly related to the difference in Fermi level^{*} (Schein, 2007); the tribocharging of insulator materials, however, is still not well understood. Possible insulator-insulator contact charging mechanisms have been proposed to be the following: electron transfer, ion transfer and material transfer (Gooding et al., 2011). The triboelectric series ranks a list of common materials according to their electron affinity upon contact, the position of the material in the series indicates how effectively the charges will be exchanged. It is a compiled study and analysis on the materials' chemical nature, electrochemical reactions, work function, ion densities, thermionic emission, triboemission and surface affinity, etc. However, this guideline does not explain how seemingly identical materials still exchange charges, as the equilibrium should already exist. The existence of this equilibrium has been postulated and backed up by the divergent rankings of likelihood to give up electrons upon contact from independent researchers, and can be attributed to the complexities introduced by humidity (Zheng et al., 2014), surface roughness (Fan et al., 2012), temperature (Xu et al., 2018), force or strain (Y. Chen et al., 2018), particle size (Lacks et al., 2007) and other mechanical properties. In general, the relevant properties are assumed to be those of the surface than those of the bulk, and there is no universal tribocharging model.

Thermally-driven contact charging processes such as dust devils, lightning, or sand storms do not occur on the Moon. However, constant micrometeoroid bombardment and exploration activities by astronauts and rovers can create tribocharging, which have been shown to be a possible dominant charging process (Sickafoose et al., 2001), particularly in current-starved regions such as a polar crater or the lunar nightside, lunar rover wheels could generate $\sim 10^3$ V at their maximum speeds (Jackson et al., 2015). The effect of tribocharging was somewhat mitigated by sunlight in the Apollo missions. The charge buildup could pose an electrostatic discharge hazard due to high potentials and charge dissipation times for the astronauts. The population balance model proposed by Lacks et al. (2007) and Waitukaitis et al. (2014) established that there is a general trend of smaller particles accumulating electrons, whilst the larger particles are depleted of electrons. Lunar simulants have been put under test to induce tribocharge among themselves. Forward et al. (2009) brought JSC-1 particles into contact and the results of charge segregation agreed with the general triboelectric tendency of size dependency that smaller JSC-1 particles charge negatively and larger ones positively. The amount of charge transferred can also be approximated as a function of frequency of contact (Kelly et al., 1989; Lindley et al., 1997), so in the case of irregular regolith shapes, the number of contacts is likely to be higher than a smoother surface.

^{*}Higher Fermi level corresponds to a lower work function, and vice versa.

Tribocharging has been demonstrated to facilitate particle movement in an electrostatic travelling wave. Adachi et al. (2017) has demonstrated that this technique can be used in a particle-size sorting system of lunar regolith for in-situ resource utilisation on the Moon; 20 μm FJS-1 simulant particles in a vacuum were successfully separated from bulk material through the charge acquired by triboelectrification on a polyimide-coated conveyor.

5.3 Dielectrophoretic Force

The term dielectrophoresis, a phenomenon describing the movement of charge-neutral dielectric particles in response to polarisation forces generated by a non-uniform electric field, was first coined by (Pohl, 1951). The Dielectrophoretic Force (DEP) induces dipole moments in small, polarised but uncharged particles. Subsequent study from the same researcher further consolidated the characterisation of such force in applications, especially found in biotechnology and particle manipulation, etc. (Pohl et al., 1978). It is commonly applied to separate dielectric particles, such as cells (Doh et al., 2005; Deng et al., 2013), latex particles (Green et al., 1997), and mineral particles (H. Chen et al., 2010), often with technology akin to that of EDS.

As stated in (Pohl et al., 1978), the force equation derivation is based on the assumptions that the dipoles should firstly be much smaller than the variations in the electric field they are placed in, nor alter the overall electric charge distribution in the medium. Secondly, higher-order moments should not have a significant effect and lastly, the electrostatic approximation should accurately describe the electric forces acting on the particles. The expression of $\mathbf{F} = \int_{body} (\mathbf{P} \cdot \nabla) \mathbf{E}_0 dv$ calculates the force acting upon a spherical dielectric body in a fluid medium, where \mathbf{P} is the polarisation, and \mathbf{E}_0 is the local electric field in the volume element, dv . This is one of three approaches to consider the DEP exerted on a particle, with the other two being the Maxwell-Stratton stress analysis and the Helmholtz energy approach. The first approach, known as the dipole approach, calculates the total force resulting from the field's interaction with the dipole moments of each volume element. It is the most suitable method for describing DEP in a particle-EDS system.

In such theoretical calculations, the bodies are assumed to be homogeneous and isotropic. For a small, homogeneous sphere of permittivity ϵ_p experiences a force in a non-uniform electric field in vacuum is expressed as:

$$\mathbf{F}_{di} = (\mathbf{p} \cdot \nabla) \mathbf{E} = 2\pi\epsilon_0 r_p^3 \left(\frac{\epsilon_p - \epsilon_0}{\epsilon_p + 2\epsilon_0} \right) \nabla E^2 \quad (5.4)$$

where \mathbf{p} is the effective induced dipole moment vector, ϵ_0 the permittivity of the medium (vacuum), r_p is the radius of the sphere and ϵ_p the dielectric permittivity of the particle.

However, this does not apply well in the case of a multi-particle system where parti-

cles are in contact with multiple surfaces, including other particles and a substrate, and where the particles deviate significantly from a spherical shape. Moreover, the system will never achieve charge neutrality due to the inevitable tribocharging.

References

- Abbas, M. M. et al. (2007). “Lunar dust charging by photoelectric emissions”. In: *Planetary and Space Science* 55.7-8, pp. 953–965.
- Adachi, M. et al. (2017). “Particle-size sorting system of lunar regolith using electrostatic traveling wave”. In: *Journal of Electrostatics* 89, pp. 69–76.
- Calle, C. I. et al. (2006). “Electrodynamic dust shield for surface exploration activities on the moon and Mars”. In: *57th International Astronautical Congress conference*. KSC-2006-125.
- Champlain, A. et al. (2016). “Lunar dust simulant charging and transport under UV irradiation in vacuum: Experiments and numerical modeling”. In: *Journal of Geophysical Research: Space Physics* 121.1, pp. 103–116.
- Chen, H. et al. (2010). “Separation and manipulation of rare-earth oxide particles by dielectrophoresis”. In: *Chinese Journal of Chemical Engineering* 18.6, pp. 1034–1037.
- Chen, Y. et al. (2018). “Elastic-beam triboelectric nanogenerator for high-performance multifunctional applications: Sensitive scale, acceleration/force/vibration sensor, and intelligent keyboard”. In: *Advanced Energy Materials* 8.29.
- Deng, Y.-L., J.-S. Chang, and Y.-J. Juang (2013). “Separation of microalgae with different lipid contents by dielectrophoresis”. In: *Bioresource Technology* 135, pp. 137–141.
- Doh, I. and Y.-H. Cho (2005). “A continuous cell separation chip using hydrodynamic dielectrophoresis (DEP) process”. In: *Sensors and Actuators A: Physical* 121.1, pp. 59–65.
- Fan, F.-R. et al. (2012). “Transparent triboelectric nanogenerators and self-powered pressure sensors based on micropatterned plastic films”. In: *Nano letters* 12.6, pp. 3109–3114.
- Forward, Keith M., Daniel J. Lacks, and R. Mohan Sankaran (2009). “Triboelectric charging of lunar regolith simulant”. In: *Journal of Geophysical Research: Space Physics* 114.A10.
- Gooding, D. M. and G. K. Kaufman (2011). “Tribocharging and the triboelectric series”. In: *Encyclopedia of Inorganic and Bioinorganic Chemistry*, pp. 1–14.
- Green, N. G. and H. Morgan (1997). “Dielectrophoretic separation of nano-particles”. In: *Journal of Physics D: Applied Physics* 30.11, p. L41.
- Hamaker, H. C. (1937). “The London—van der Waals attraction between spherical particles”. In: *Physica* 4.10, pp. 1058–1072.
- Hartzell, C. M. and D. J. Scheeres (2011). “The role of cohesive forces in particle launching on the Moon and asteroids”. In: *Planetary and Space Science* 59.14, pp. 1758–1768.
- Hays, D. A. (1995). “Adhesion of charged particles”. In: *Journal of adhesion science and technology* 9.8, pp. 1063–1073.

- Israelachvili, J. N. (2011). *Intermolecular and surface forces*. Academic press.
- Izvekova, Y. N. and S. W. I. Popel (2013). “Adhesion of rough particles of lunar regolith”. In: *EPSC Abstracts* 8.
- Jackson, T. L., W. M. Farrell, and M. I. Zimmerman (2015). “Rover wheel charging on the lunar surface”. In: *Advances in Space Research* 55.6, pp. 1710–1720.
- Kelly, E. G. and D. J. Spottiwod (1989). “The theory of electrostatic separations: A review part II. Particle charging”. In: *Minerals Engineering* 2.2, pp. 193–205.
- Krupp, H. (1967). “Particle adhesion theory and experiment”. In: *Advan. Colloid Interface Sci.* 1, pp. 111–239.
- Lacks, D. J. and A. Levandovsky (2007). “Effect of particle size distribution on the polarity of triboelectric charging in granular insulator systems”. In: *Journal of electrostatics* 65.2, pp. 107–112.
- Lindley, K. S. and N. A. Rowson (1997). “Charging Mechanisms for Particles Prior to Electrostatic Separation”. In: *Physical Separation in Science and Engineering* 8. 13 pages, p. 096189. DOI: [10.1155/1997/96189](https://doi.org/10.1155/1997/96189).
- Liu, G. Q. and J. S. Marshall (2010). “Effect of particle adhesion and interactions on motion by traveling waves on an electric curtain”. In: *Journal of Electrostatics* 68.2, pp. 179–189.
- Perko, H. A., J. D. Nelson, and W. Z. Sadeh (2001). “Surface cleanliness effect on lunar soil shear strength”. In: *Journal of Geotechnical and Geoenvironmental Engineering* 127.4, pp. 371–383.
- Pohl, H. A. (1951). “The motion and precipitation of suspensoids in divergent electric fields”. In: *Journal of applied Physics* 22.7, pp. 869–871.
- Pohl, H. A., K Pollock, and J. S. Crane (1978). “Dielectrophoretic force: A comparison of theory and experiment”. In: *Journal of Biological Physics* 6, pp. 133–160.
- Poppe, A. and M. Horányi (2010). “Simulations of the photoelectron sheath and dust levitation on the lunar surface”. In: *Journal of Geophysical Research: Space Physics* 115.A8.
- Rabinovich, Y. I. et al. (2000). “Adhesion between nanoscale rough surfaces: II. Measurement and comparison with theory”. In: *Journal of colloid and interface science* 232.1, pp. 17–24.
- Rajupet, S. et al. (2021). “Relative importance of electrostatic and van der Waals forces in particle adhesion to rough conducting surfaces”. In: *Physical Review E* 103.4, p. 042906.
- Ramakrishna, S. N. et al. (2011). “Controlling adhesion force by means of nanoscale surface roughness”. In: *Langmuir* 27.16, pp. 9972–9978.
- Schein, L. B. (2007). “Recent progress and continuing puzzles in electrostatics”. In: *Science* 316.5831, pp. 1572–1573.
- Sickafoose, A. A. et al. (2001). “Experimental investigations on photoelectric and triboelectric charging of dust”. In: *Journal of Geophysical Research: Space Physics* 106.A5, pp. 8343–8356.
- (2002). “Experimental levitation of dust grains in a plasma sheath”. In: *Journal of Geophysical Research: Space Physics* 107.A11, SMP–37.
- Sternovsky, Z. et al. (2002). “Contact charging of lunar and Martian dust simulants”. In: *Journal of Geophysical Research: Planets* 107.E11.

- Tabor, D. (1977). “Surface forces and surface interactions”. In: *Plenary and invited lectures*. Elsevier, pp. 3–14.
- Waitukaitis, S. R. et al. (2014). “Size-dependent same-material tribocharging in insulating grains”. In: *Physical Review Letters* 112.21.
- Wang, X. et al. (2016). “Dust charging and transport on airless planetary bodies”. In: *Geophysical Research Letters* 43.12, pp. 6103–6110.
- Xu, C. et al. (2018). “On the electron-transfer mechanism in the contact-electrification effect”. In: *Advanced Materials* 30.15.
- Zheng, X., R. Zhang, and H. Huang (2014). “Theoretical modeling of relative humidity on contact electrification of sand particles”. In: *Scientific Reports* 4.1, p. 4399.

6 Experimental Setup and Methods

This section will present and describe the setup and methods used for the EDS experiments. A protocol outlining the procedure is also provided. The experiments aim to investigate the effect of vacuum and UV radiation on the efficacy of electrostatic dust removal.

This experimental setup can be split into the hardware and software components. This section will outline the setup, define the choice of parameters, address the challenges and limitations of building an Earth-bound lunar-environment-simulating setup and explain the methodologies of experimental procedures.

6.1 Design of EDS in this Work

The EDS design has remained largely unchanged since it was first introduced. The three-phase electrode system developed by Masuda et al. (1972) was adapted by NASA, where the configuration allows for a travelling wave which has a strong translational component that rapidly moves the dust particles along a certain direction. A spiral pattern, or a Fresnel ring-like pattern, has been found to yield a higher dust removal rate (Saeidpour et al., 2023) compared to rectangular or zigzag patterns. Furthermore, electrodes in a non-spiral pattern produce strong localised fields at the corners, which increases the risk of electric breakdown. The spiral pattern has axial symmetry, which also has the advantage of simplifying simulation work. A single-phase standing-wave design could work in Martian or terrestrial conditions, where other factors such as air current and a tilted surface (gravitational force) could help assist dust transport. The lunar environment requires an effective dust removal without external assistance.

The spacing between the electrodes and the width of the electrodes have been found to greatly influence cleaning efficiency. The movement of the smaller particles becomes disoriented as spacing distance increases (M. Mazumder et al., 2013). Calle et al. (2004) concluded that most dust was removed with the smallest spacing they tested, which was 1 mm. Subsequent studies from Calle et al. over the years found that for solar panel applications in various atmospheres, the spacing did not significantly affect the outcome. (Kawamoto et al., 2004) observed maximum electric field with spacing twice the width of the electrodes. Other researchers also found a trend of decreasing efficiency with increasing spacing up to a few millimeters (Johnson et al., 2005; Sayyah et al., 2016). A simulation study by Chesnutt et al. (2019) revealed that, at a constant voltage, the electric field strength decreases as electrode

width increases. However, the electric field above the electrode becomes stronger with greater width because of the larger surface area. There is also a positively correlated relationship between the levitation height and spacing, as there is less pull of particles in the horizontal direction to the adjacent electrodes.

Figure 6.1 shows the ITO electrode design, which have extended pads that allow for electrical contact with the high voltage cables. Dust particles are deposited above the spiral-pattern area on the coating, which is referred to as the 'effective area' of this EDS system.

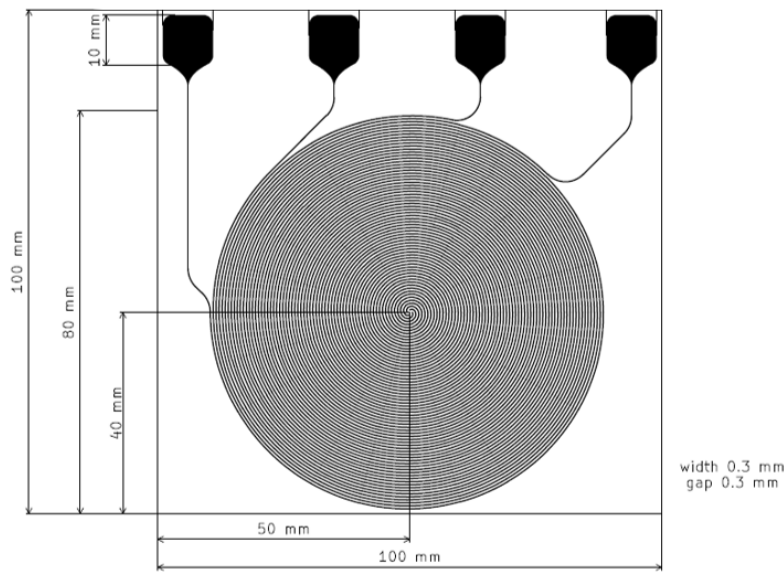


Figure 6.1: Drawing of EDS electrode track design on a $100\text{ mm} \times 100\text{ mm}$ substrate. The track width is 0.3 mm and the gap is 0.3 mm . The spiral pattern is covered with dust during EDS testing. Made by Masato Adachi from the University of Kyoto.

A significant challenge in operating the EDS is preventing Paschen breakdown of the EDS, so the voltage parameter and design of the EDS need to be taken into consideration when operating at such high voltage. For the high vacuum conditions of a simulated lunar environment, the breakdown voltage should be higher, as there are fewer gas molecules in the space to be ionised. However, Paschen's Law becomes analytically challenging to describe a system approaching a perfect vacuum. The surface condition of the electrodes becomes the dominant factor in determining the breakdown; asperities become field emitters, ionising any gas molecule present, which can result in a spark where the high voltage discharges across the gap. This may cause significant surface damage through erosion, as observed in this experiment, where the exposed part of the ITO electrodes was sometimes burned away after several uses. The exact conditions and extent of use that led to the damage were unclear, as this was not always immediately noticed.

Preparing EDS Plates

The standard EDS plate consists of multiple layers of materials. The glass substrate with a nanolayer of ITO was manufactured by *Präzisions Glas & Optik GmbH* and laser-etched into electrode tracks by *LPKF Laser & Electronics AG*. Subsequently, the coating material was manually applied on top of a sheet of optically clear adhesive from 3M was placed onto the bare EDS plate. This process resembles the application of a protective screen to a smartphone.

Figure 6.2 shows the individual layers of the EDS composition in the experiment and the spiral ITO tracks on a glass substrate. An Alternating Current (AC) high-voltage signal generator is connected to the electrodes via the four electrode pad areas that are left uncovered: Figure 6.2(a) shows the components of a $100\text{ mm} \times 100\text{ mm} \times 1.1\text{ mm}$ EDS substrate plate, which consists of a (1) borosilicate glass substrate, (2) an ITO conductive layer etched into 4-phase spiral tracks, a (3) UV-resistant optically clear adhesive, and a (4) coating material. The coating covering the EDS electrodes is typically a 0.1 mm thick borosilicate glass from SCHOTT (D 263® T ECO), or it can be a layer of Kapton polyimide film or a piece of Beta cloth fabric. Beta cloth is a white, Polytetrafluoroethylene (PTFE)-impregnated glass cloth used as an outer Multi-Layer Insulation Blanket (MLIB) layer due to its resistance to atomic oxygen in Low Earth Orbit. It was extensively used on the Space Shuttle and continues to protect the interior and exterior of the International Space Station (ISS).

Figure 6.2(b) shows a schematic drawing of the EDS side view (not to scale): each of the electrode tracks is 0.3 mm in width w , with a 0.3 mm gap g in between. The thickness of the glass substrate h_g is 1.1 mm and the thickness of the ITO electrode, not indicated here, is a few nanometers thick; dielectric 1 is a coating material and dielectric 2 is the OCA adhesive. Figure 6.3 shows the EDS plates with different coating materials, namely glass (100 μm thickness), Kapton (50 μm thickness), and Beta cloth (200 μm thickness).

Risk of Electric Breakdown

As we approach near-perfect vacuum conditions, the surface condition of the electrodes becomes the predominant factor in determining breakdown. Any asperities on the electrode surface can act as field emitters, ionising sporadic gas molecules. These ions are subsequently accelerated and impact the electrode, leading to local heating and high-voltage discharges across the gap between electrodes, potentially causing significant surface damage. The breakdown voltage also becomes sensitive to pressure changes in high vacuum. For instance, when the VUV lamp is activated, chamber pressure can spike by up to an order of magnitude, which might result in localised breakdowns in the uncoated conductive EDS material. Applying a thin layer of insulating material to the electrodes can prevent electrical breakdown, allowing them to withstand voltages up to kilovolts, depending on the vacuum level.

Figure 6.4 shows the area of uncoated ITO that has experienced breakdown damage.

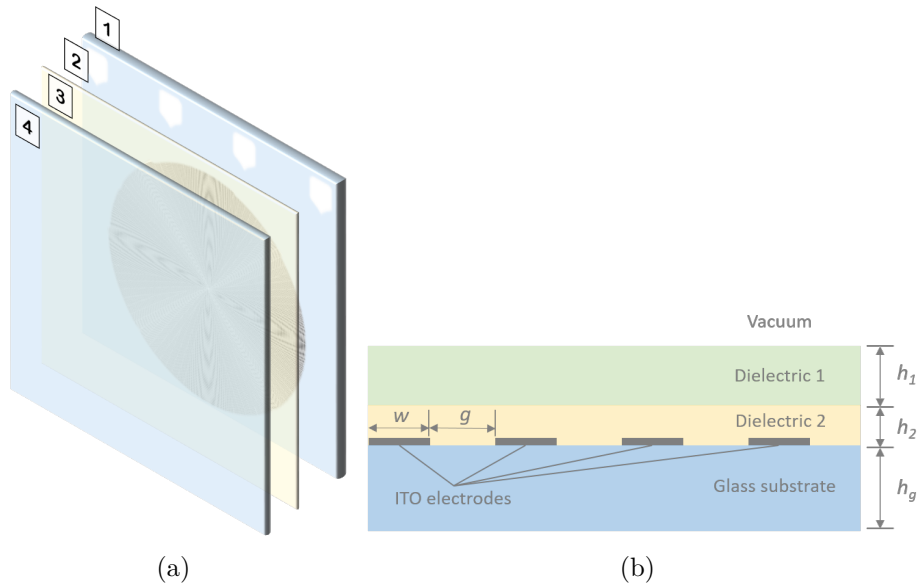


Figure 6.2: Composition setup of the EDS plate used in this project. (a) Structure of an EDS plate, showing its respective layers: (1) substrate, (2) ITO electrode tracks, (3) adhesive, and (4) coating material. (b) Side view of the assembled EDS with component dimensions.

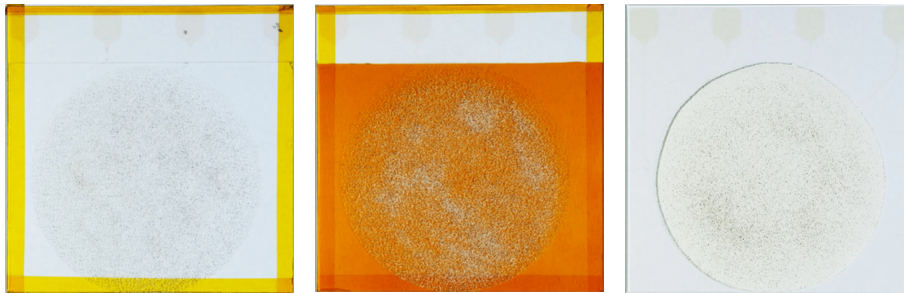


Figure 6.3: Different coating materials on top of the ITO track with an LHS-1 sample deposited on top of the effective area. From left to right: glass, Kapton, Beta cloth.

This damage can occur after a single use of the EDS plate or over multiple uses; however, the precise timing and cause of this damage remain unclear. Minor damage can be repaired with a small amount of liquid solder paste, provided the affected area is not too large. The damage shown in the photograph exceeds the scope of a quick repair and would be discarded.

6.2 Sample Preparation

Sample preparation was one of the most critical stages in the experiment, as there were many potential sources of contamination: the fragile EDS could break, or the sample surface could become disturbed. Utmost care was taken to ensure that each

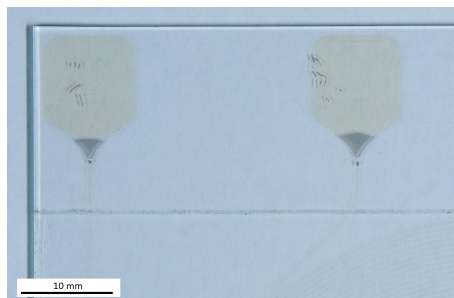


Figure 6.4: Damaged ITO tracks. The ITO coating is ablated at the neck transition from the pad area to the thin track area, with additional ablation observed in portions of the pad area. The maximum damaged area is typically around $2\text{ mm} \times 2\text{ mm}$.

step was handled meticulously, and every repetition was as reproducible as humanly possible. The detailed experimental protocol and workflow can be found later in this section.

Preparing Simulant Samples

The simulant particles were first dry-sieved with a vibratory sieve shaker into two size ranges for our study: $25\text{--}50\text{ }\mu\text{m}$ and $80\text{--}100\text{ }\mu\text{m}$. The shaker's adjustable sieve acceleration allowed for calibrated and reproducible results. The rationale behind these choices was that $80\text{--}100\text{ }\mu\text{m}$ particles were among the largest in the regolith population, while particles below $25\text{ }\mu\text{m}$ became difficult to remove solely via electrostatic means.

The sieved simulant samples were transferred to glass Petri dishes and placed in a vacuum oven at 10^{-2} mbar and 200°C . This procedure, commonly known as *baking*, involved the removal of moisture and organic substances from the particle surfaces. Baking is a necessary step when testing adhesion, as it drastically reduces inter-particle interactions due to hydrogen bonding, an attractive force that is virtually non-existent on the Moon. The longer the sample has been exposed to air, the longer it needs to be baked to remove the moisture Tilley, [1975]. Figure [6.5] shows the baked and unbaked LMS-1 samples side-by-side. The unbaked sample exhibits a darker colour due to its moisture content.

After baking, the baked sample was removed from the vacuum oven for distribution onto the EDS. Consequently, there was a brief period, typically between 5 to 10 minutes, during which the particles were exposed to atmospheric air in the transfer and distribution process. However, this brief exposure did not negate the drying effort.



Figure 6.5: Simulant samples (LMS-1 in 25–50 μm size range) in a Petri dish that usually goes into the vacuum oven for baking. Here some unbaked grains are placed next to the baked grains for comparison. A visible colour difference due to moisture content can be observed.

Dust Distribution System

As depicted in Figure 6.6, (a) is the manual dust distribution system consists of a modular setup of an aluminium cylinder with an inner diameter matching the electrode area, a sieve corresponding to the particle size, and an additional sieve layer made from stocking material. (b) Shows the clean EDS plate was weighed with the sieve on a high-precision scale (resolution of 0.001 g). A predetermined amount of simulant was evenly distributed onto the sieve using a spatula. Once the desired amount was achieved, the system was immediately transferred to the workbench adjacent to the scale, and the aluminium cylinder was inserted between the sieve and the EDS plate. (c) Shows simulant particles were then distributed using a spatula without tapping. Gentle vibration was induced by scratching the sieve mesh with the spatula, allowing the particles to fall directly through the sieves without traversing the surface. The other hand continuously rotated the sieve to ensure a more homogeneous distribution. (d) Is where the EDS plate with simulant particles was weighed again to ensure no significant loss of dust occurred during distribution. The sample was then ready for placement into the vacuum chamber.

A case of tribocharging took place during the process of sieving particles in this stage. In order to achieve a more uniform distribution, a two-layer sieving mechanism was devised to separate the particle as much as possible before they fall onto the EDS surface. The sieving, especially with the stocking material, tribocharged them to similar charges, which compelled them to repel each other. Charge generation on bulk powders under terrestrial conditions during sieving is approximated to have the mass charge density of 10^{-3} to 10^{-5} $\mu\text{C}/\text{kg}$ (Staff, 1992).

The entire dust distribution process took place within a fume hood, and protective gear was worn to minimise inhalation of dust particles. Distributing a precise, small amount of dust particles evenly onto a small circular surface was challenging. Ideally,

an automated system would have been used, but due to cost and time constraints, a manual approach with practiced hands was employed and actually proved superior in terms of achieving an even dust layer distribution.

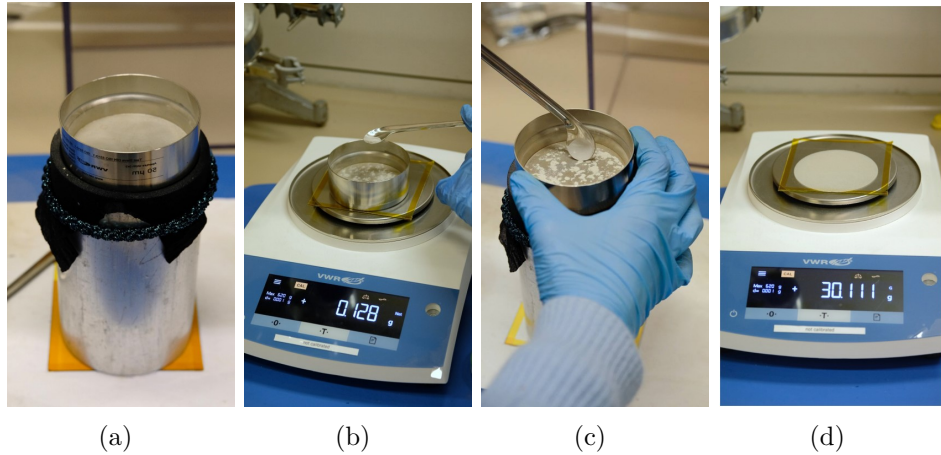


Figure 6.6: Dust distribution system and the process of depositing an even layer of dust onto the EDS. The modular system composes of two parts: a sieve with mesh size matching the simulant sample size range and a cylinder with an inner diameter matching the effective area of the EDS. This procedure takes about 5 minutes to complete the dust deposition process.

Figure 6.7 shows an example of dust distribution in literature compared to the dust distributed using the system mentioned above. Once prepared, each sample was promptly transferred to the vacuum chamber inside a protective box, preventing disturbance to the dusty surface caused by drafts during transport. Figure 6.7(c) shows the EDS plates with simulant samples placed within the vacuum chamber. The four electrodes are attached to the High Voltage (HV) source via polyimide-insulated cables and polyimide tapes (yellow).

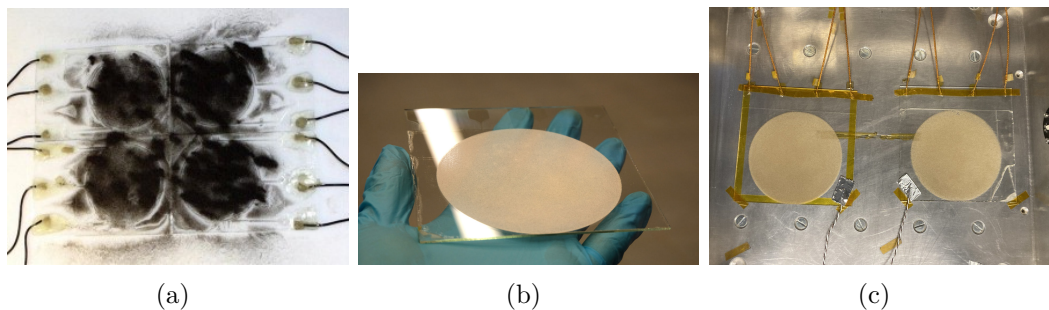


Figure 6.7: Dust distribution pattern comparison with results from literature. The comparison highlights the evenness achieved by the dust deposition system developed in this project. (a): From Calle et al. (2013). (b) and (c): From this project.

6.3 Experimental Facility

This section will describe the role of each component in the experimental setup and how they collectively contributed to the overall project. The primary hardware component was the vacuum chamber designed to accommodate the elements of the EDS system, including the EDS and high-voltage peripherals. The EDS system was controlled by a LabVIEW program, and a high-speed camera was used to capture the dust dynamics. This section will explain their significance within the experimental framework.

6.3.1 Vacuum Chamber

An overview of the setup is illustrated in Figure 6.8 and Figure 6.9 shows photos of the vacuum chamber and the two pumps necessary for achieving and sustaining the high vacuum. Figure 6.11 shows the view into the vacuum chamber via the transparent port at the front.

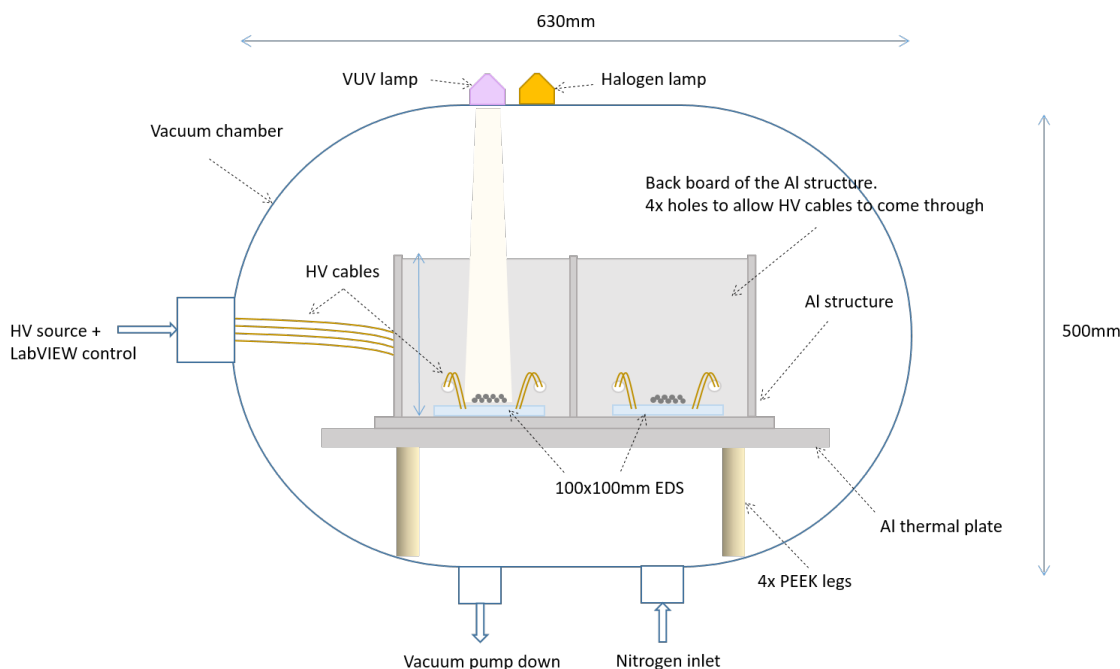


Figure 6.8: A sketch of the setup within the vacuum chamber shows its Berliner-like shape, measuring 63 cm in diameter and 50 cm in height. The EDS plates can be easily inserted and removed after each experimental run.

The vacuum chamber has two pumps: a vacuum pump and a turbomolecular pump. The turbo pump is activated only when the pressure reaches approximately 10^{-1} mbar to prevent over-straining. These pumps are used to achieve and maintain a high vacuum of approximately 10^{-6} mbar. The chamber is connected to a liquid nitrogen inlet to facilitate cleaner depressurisation, as using liquid nitrogen reduces the chance of contaminating the chamber with moisture and impurities compared to using air. When carrying out adhesion-related experiments, a vacuum level of

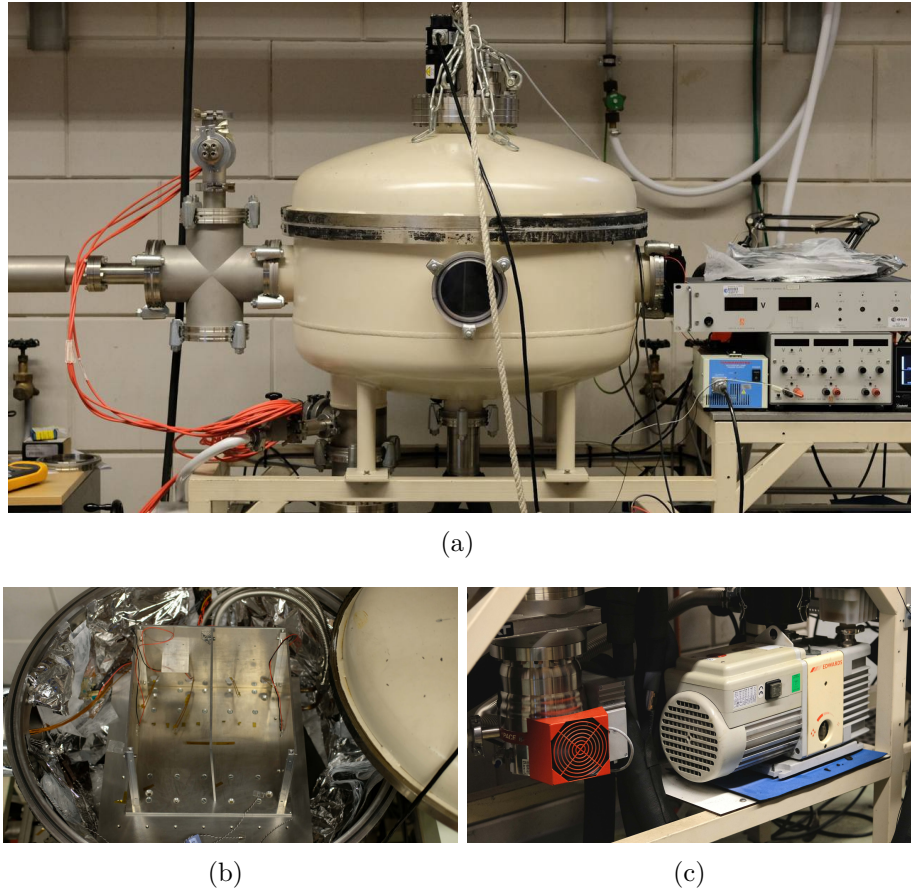


Figure 6.9: Photographs of the vacuum chamber setup. The chamber is connected to two vacuum pumps and has several feedthrough ports. There is a clear front port, a port for HV cable connections, a port for electrical connections (at the back), a top port for VUV lamp and a port for thermocouple connections. (a) Front of the vacuum chamber. (b) Vacuum chamber interior. (c) Vacuum pumps.

at least 10^{-6} Torr, around 1.3×10^{-3} mbar, over a period of several hours should be maintained, as electrostatically-induced adhesion was found to decrease rapidly above this pressure (Berkebile et al., 2012). The typical pressure on the lunar surface is approximately 1×10^{-12} mbar, a level challenging to replicate in Earth-based laboratories.

The vacuum chamber is designed to accommodate two EDS plates, high-voltage cables, a thermal plate, an aluminium structure for electrical grounding, and a physical barrier between the two EDS plates to prevent cross-contamination when activating the dust removal system. The chamber's interior is lined with MLI to enhance temperature regulation, particularly during cooling. This material, commonly used in spacecraft, helps mitigate heat loss through thermal radiation. Beneath the EDS plates and the aluminium structure, there is a thermal plate that serves as a heating and cooling element, capable of reaching temperatures ranging from -40°C to

200°C. A layer of pyrolytic graphite* is placed between the thermal plate and the aluminium structure to improve thermal contact.

There are several separate feedthrough ports to allow for optical viewing and the installation of peripherals such as cables, a UV lamp, a halogen lamp, and thermocouples, with potential for further expansion.

Vacuum Ultraviolet Lamp

The primary charging mechanism on the illuminated side of the lunar surface is thought to be UV radiation below 200 nm, which possesses photon energies surpassing the work function of the lunar regolith materials (Abbas et al., 2007). The VUV lamp shown in Figure 6.10 is a deuterium lamp with a peak intensity at $\lambda = 160$ nm, Figure 6.12 also shows the charge neutralisation time until 10^{-6} mbar.



Figure 6.10: VUV lamp utilised for generating the photoelectric effect, positioned directly above one of the EDS plates. The lamp takes 25 sec to warm up and immediately outputs the maximum UV intensity.

This VUV lamp manufactured by *Hamamatsu* was originally designed for use as an electrostatic charge remover in various processes, including semiconductor wafer and liquid crystal display (LCD) panel production, as well as electron beam applications. The high-energy vacuum UV light emitted at wavelengths less than 160 nm is highly effective at removing electrostatic charges within a few seconds, depending on the lamp's distance from the target.

The operating principle involves ionising residual atoms and molecules in the vacuum, which ejects electrons and creates ions that neutralise static electricity on the

*A man-made material with excellent planar thermal conductor properties, often use as a thermal-interface material. It also exhibits great diamagnetism.

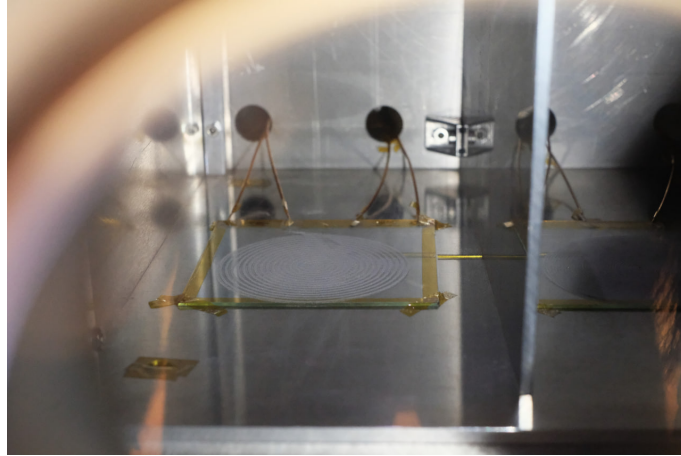


Figure 6.11: View through the front vacuum feedthrough, showing both EDS plates from different angles. This clear view allows for camera observation and recording.

target object. This process occurs almost instantaneously upon activating the lamp. However, our intended use of the VUV lamp differs from this described operation: by continuously irradiating the dusty surface with the lamp left on, we inadvertently create an imbalance of electrostatically charged particles. This imbalance results from an excess of photoelectrons and positive ions, both within the residual atmosphere inside the vacuum and on the particle surface.

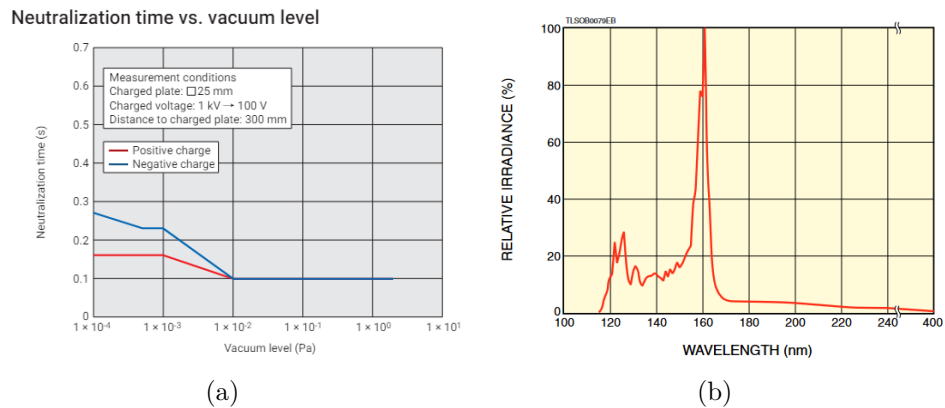


Figure 6.12: (a) Charge neutralisation time of VUV lamp from low to high vacuum. The lamp is ineffective near atmospheric pressure due to rapid UV absorption by the abundant air molecules. The neutralisation time increases gradually with decreasing pressure. (b) Spectral distribution of VUV lamp. This lamp exhibits peak irradiance at 160 nm. Below 200 nm is typically where the photoelectric effect occurs. Source: Hamamatsu Photonics K.K. (2024)

The lamp body is directly fitted to a vacuum flange that can be conveniently attached to the vacuum chamber without additional mechanical parts and is sealed on the vacuum flange by two O-rings. The lamp is ineffective in atmospheric conditions

as the vacuum UV light it emits is absorbed by the abundant air molecules. Therefore, the electrostatic charge removal capability is only achievable in a vacuum or in an environment where air has been adequately substituted with an inert gas such as nitrogen. The spectral distribution ranges from 115–400 nm, with a warm-up time of approximately 25 s.

For reference, in this setup, it produces a photosaturation current density on aluminium oxide that is approximately 30 times greater than what is expected from the solar spectrum at 1 AU[†] (Grard, 1973). It is therefore much stronger than the UV intensity incident on the Moon. However, this partially compensates for the lack of other radiation sources such as solar wind plasma. The lamp has a wide directivity, meaning that it has a large-area irradiation, as shown in Figure 6.13. At an operating distance of 38 cm from the lamp to the surface of the EDS plate, the base of the UV light cone sufficiently covers the effective electrode area on the EDS, with a diameter of 23.6 cm.

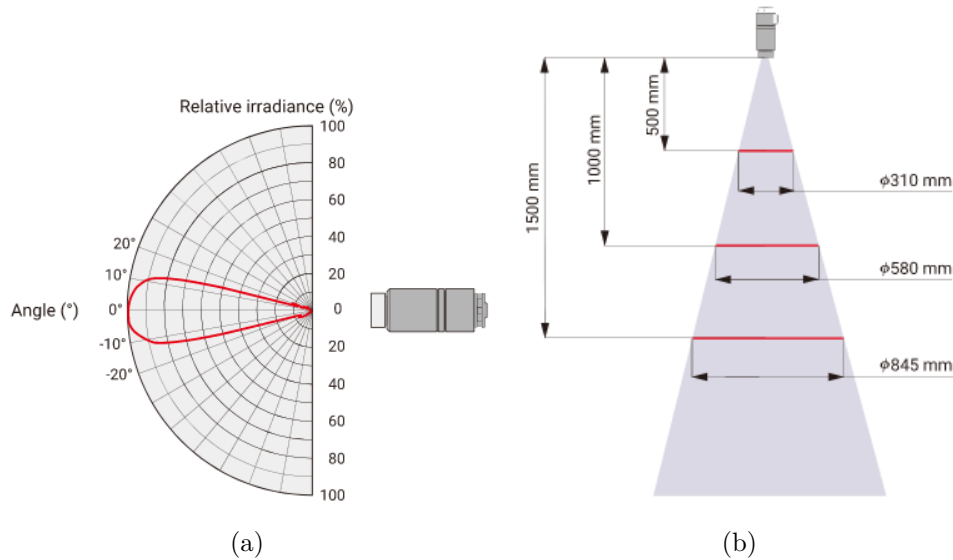


Figure 6.13: (a) Typical directivity (light distribution) of the VUV lamp. At an irradiating angle larger than 12°, the relative irradiance quickly falls below 80%. (b) The cone of a typical light irradiation range (Hamamatsu Photonics K.K., 2024). The EDS is approximately 38 cm away from the VUV source.

A photodiode was used to check for the UV radiation coverage on the EDS. The output current of the UV photodiode (SXUV5 from *Opto Diode*) was measured using a *Keithley* 6517 electrometer. It was mounted on a small copper Printed Circuit Board (PCB) and positioned at various locations within the effective area to assess the uniformity of UV irradiation. The responsivity of the photodiode for the UV lamp range is the lowest of all its measured values, being below 0.05 A/W (Figure 6.14), but it was nevertheless adequate for the required measurements. The

[†]The astronomical unit (AU) is a unit of length defined to be exactly equal to 149,597,870,700 m, about the average Earth-Sun distance.

consistent current outputs from the photodiode indicated uniform UV irradiation across the target area.

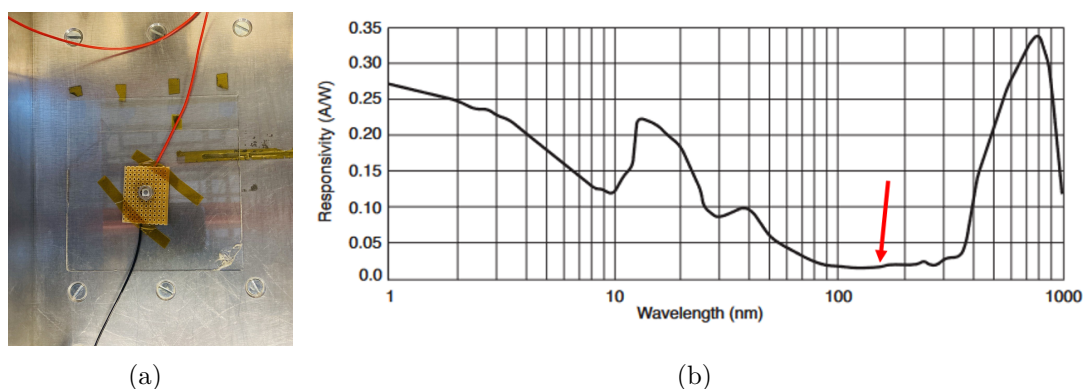


Figure 6.14: (a) A UV photodiode positioned on the EDS surface, used for measuring incident UV intensity. The photodiode was systematically moved across the effective area of the EDS to assess uniformity in UV intensity distribution within this area. (b) Typical photon responsivity of the photodiode, indicating its sensitivity across a range of wavelengths. At the peak irradiance wavelength of the VUV lamp at 160 nm (indicated by red arrow), the photodiode responsivity is relatively low but still detectable.

Solar Cell Array

To quantify the dust removal efficiency and evaluate the potential application of this technology, a Solar Array (SA) was constructed. This test aims to assess the EDS's cleaning capability and its effectiveness in reducing dust accumulation on solar panels. A monocrystalline silicon solar cell, measuring $35.6 \text{ cm} \times 6.40 \text{ cm}$, was used. The cell achieves a fill factor of 77%, which is the ratio of maximum obtainable power to the product of open-circuit voltage and short-circuit current, resulting in a maximum power output of 491.61 mW under standard test conditions[‡].

The cells were individually tested using a solar simulator (courtesy of ESTEC solar simulator lab) for quality control, ensuring consistent and precise laboratory conditions to evaluate each cell's output power and other critical parameters, such as open-circuit voltage (V_{oc}) and short-circuit current (I_{sc}). The xenon arc lamp used in the simulator emits light in 10 ms pulses, which do not affect the temperature of the cells. This procedure ensured that defective solar cells were replaced.

The SA comprised six of these cells connected in parallel[§] on a PCB, which sufficiently cover the EDS's effective area. The total current output is the sum of the

[‡]Atmospheric conditions at room temperature.

[§]In parallel connections, solar cells maintain the voltage of a single cell. In series connections, the voltages of individual cells add up.

currents produced by each individual cell. Figure 6.15 shows the setup and utilisation of the SA. An aluminium mask, with an opening diameter matching the effective area of the EDS allowed the EDS to be positioned on the SA while simultaneously shielding the unused areas. The output current of the SA is directly proportional to the area exposed to the light source.

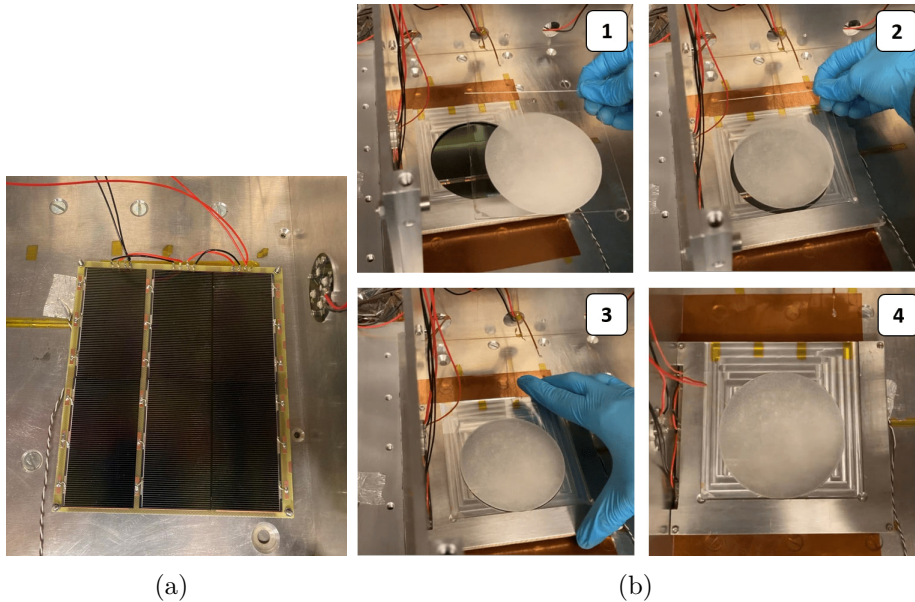


Figure 6.15: Photographs depicting an EDS with a transparent glass coating placed on top of the SA. This design prevents direct dust contact with the SA surface. (a) Six silicon solar cells connected in parallel to create the solar cell array (SA). (b) SA with an aluminium mask that leaves only the effective area uncovered.

Solar panel output efficiency can be negatively affected by heat, reducing efficiency by up to 10–25%. The optimal operating temperature for solar panels is typically 25°C. Beyond this temperature, efficiency generally decreases by 0.5% for every degree increase (Dubey et al., 2013). Consequently, the use of the halogen lamp as a source of illumination was restricted to a maximum of a few seconds.

The lamp FHL-25K-PS used here is from *JEVAlux* and is a vacuum compatible halogen lamp. The light source has a luminous flux of 300 lm and is able to withstand pressure down to 10^{-9} mbar. Although prolonged irradiation for up to 20 minutes would reach a temperature equilibrium on the surface of the SA, it would significantly lengthen the dust removal experiment, especially considering the subsequent cooling-off period.

6.3.2 High-Voltage Peripherals

The principle of the EDS relies on an alternating electric field to mobilise particles. The high-voltage amplifier (HAR-51-4M from *Hivolt*) has a signal gain of

$300\pm 1\%$ and can achieve an output voltage range from -3000 V to $+3000\text{ V}$. The amplifier's output is safeguarded against over-current, short circuits, over-voltage, over-temperature, and high voltage flash-over. As depicted in Figure 6.16, the HV amplifier is a rack capable of housing up to four high voltage amplifier modules, with each module connecting to one EDS electrode.

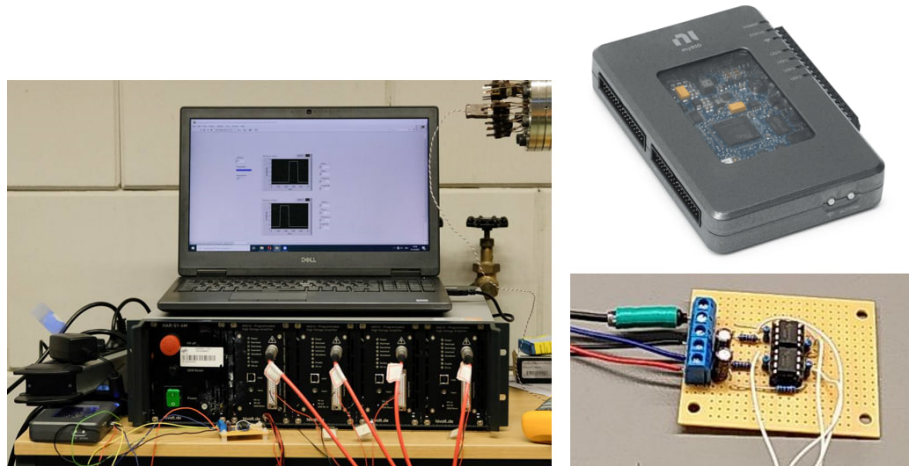


Figure 6.16: LabVIEW sends commands to the myRIO microcontroller, which outputs a voltage signal to be amplified by the HV amplifier. Clockwise from the left: Photograph of a laptop running LabVIEW software connected to a HV amplifier; a myRio-1900 (National Instruments, 2024); a dual-quad amplifier PCB (more in Signal Control).

Signal Control

The HV amplifier is controlled by the myRIO-1900 from *National Instruments (NI)*. It is a microcontroller that combines the adaptability of an ARM processor with the speed of a Field Programmable Gate Array (FPGA). This package offers both analogue and digital interfaces, featuring bipolar analogue I/O, making it an optimal choice for high-speed control applications. As part of the NI product line, it responds to commands sent from LabVIEW, which will be detailed in Sec. 6.3.3.

Figure 6.17 illustrates the interconnections among the myRIO, myRIO pinout connections, dual-quad amplifier PCB, and high-voltage amplifier. Commands are sent from a LabVIEW program on the computer to the myRIO, which is connected to the dual-quad amplifier PCB through multiple analogue output channels. The circuit elements, powered by $\pm 15\text{ V}$, invert the input voltage signal from the myRIO by 180° . AO0 and AO1 (pins 4 and 5) are analogue output channels located on Connector C of the Mini System Port (MSP). These channels are capable of generating signals with amplitudes up to $\pm 10\text{ V}$. Initially, signals of 2.5 V (pins 1 and 2) were generated by the myRIO and directed to a dual-quad amplifier PCB. The IC consists of two industry-standard dual operational amplifiers (op-amps) LM358 and two $10\text{ k}\Omega$ resistors for each op-amp, which produced an inverted copy of each signal. Subsequently, each signal was amplified by the HV amplifier with a gain of

300, resulting in an output amplitude of ± 750 V.

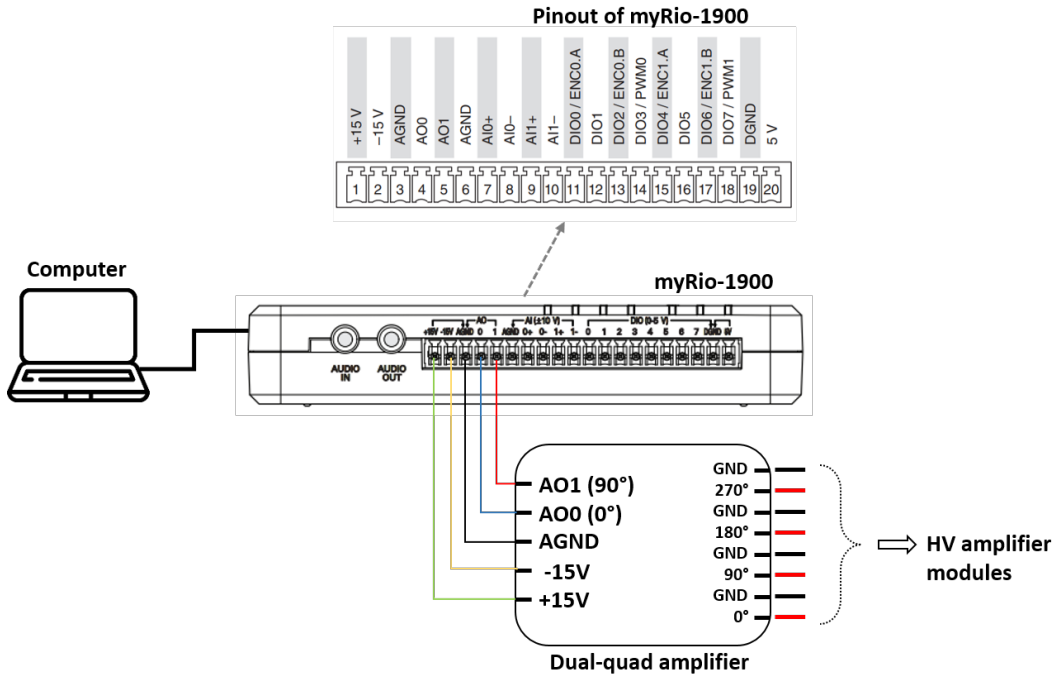


Figure 6.17: A schematic of the LabVIEW-controlled signal output. Depicted are the ports used in the myRIO microcontroller and a small PCB with a dual-quad amplifier to multiple the two signals from the myRIO into four.

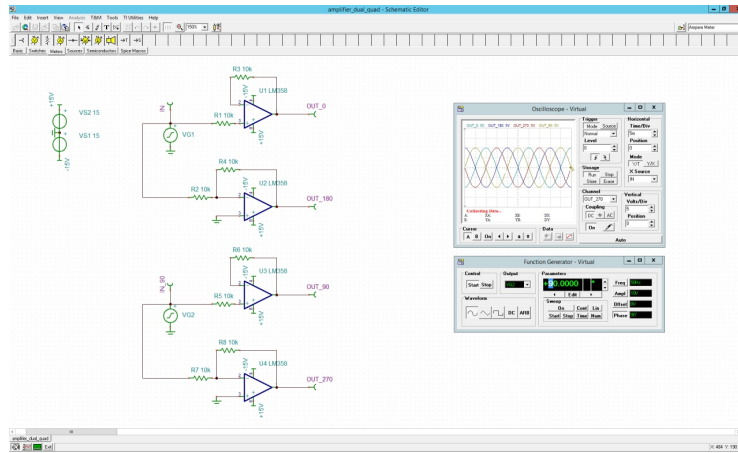
Figure 6.18 presents the op-amp schematic and its corresponding simulation results. An input of 0° and 90° signals create an output of 180° and 270° signals. The op-amp duplicates and inverts the duplicated signal relative to the 0V level. When the input signal is connected to the '+' of the op-amp, it is an amplifier with gain=1; when it is connected to the '-' of the op-amp, it becomes an inverting amplifier. For periodic signals such as sinusoidal and square waves, inverting the polarity of the voltage has the same effect as shifting the signal by 180° .

HV Amplifier Signal Processing: Sanity Check

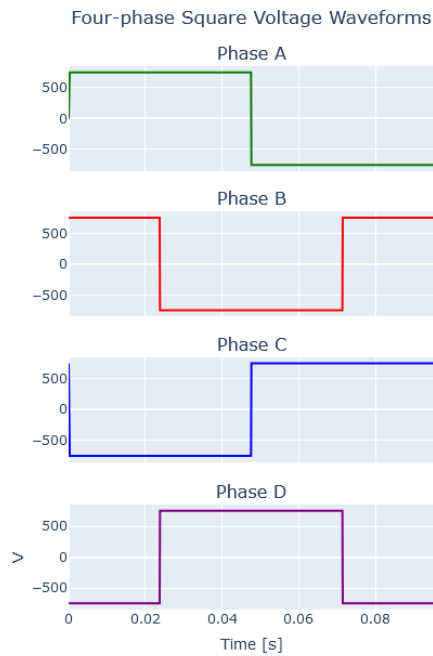
The slew rate of the HV amplifier is $15 \text{ V}/\mu\text{s}$, which adequately accommodates the input signal settings from myRIO, as per the following formula:

$$SR \geq 2\pi f V_{pk} \quad (6.1)$$

Here, SR is the slew rate, f the operating frequency, and V_{pk} the peak amplitude of the waveform. For a waveform to avoid slew rate limitations, the slew rate capability at all points in an amplifier must meet this condition. At $f = 10.5 \text{ Hz}$ and $V_{pk} = 512.5$, the right-hand side of Equation 6.1 calculates to $1.64 \times 10^{-4} \text{ V}/\mu\text{s}$, significantly lower than the amplifier's own slew rate, thus satisfying the condition.



(a)



(b)

Figure 6.18: (a) Op-amp simulation with Toolkit for Interactive Network Analysis (TINA). The schematic depicts op-amps inverting and duplicating the signals from the myRIO. (b) The resulting four-phase square voltage waveforms as outputted by the HV amplifier to the EDS electrodes, in one time period T .

HV Feedthrough and Cabling

The vacuum chamber has several feedthroughs that can be further expanded into smaller feedthroughs for various purposes (Figure 6.19). Four HV signals from the amplifier are transmitted to the EDS via four separate ultra-high vacuum (UHV) Kapton-insulated HV cables. Simultaneously supplying voltages to both EDS plates was not feasible due to the availability of only one high-voltage amplifier system.

Therefore, the two EDS plates were used sequentially, always running the test without UV first to mitigate UV contamination to the other plate. By switching the cable set between two different feedthroughs, each connected to a respective EDS plate, it was possible to power the plates one after the other within the same test, ensuring uninterrupted vacuum operation.

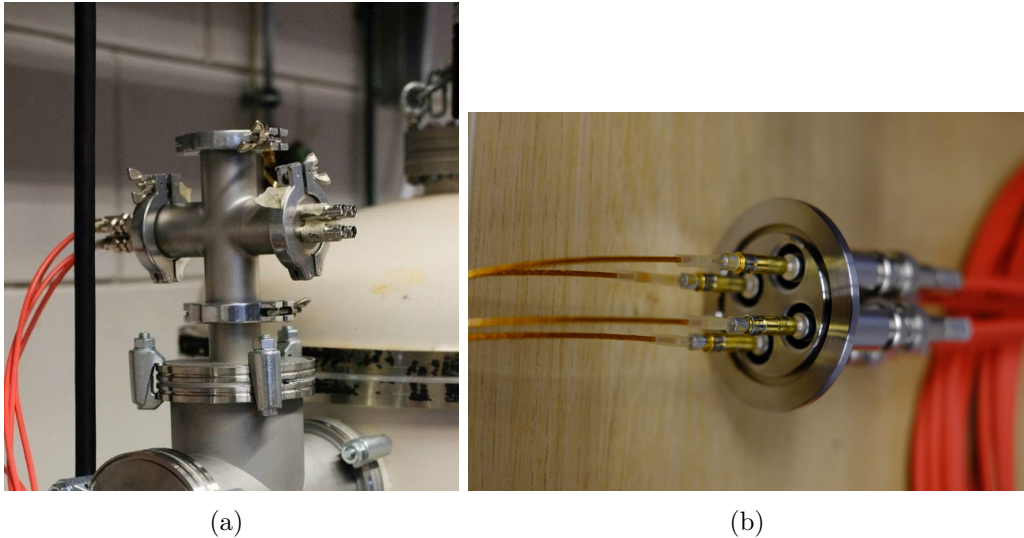


Figure 6.19: (a) Two feedthroughs of four female BNC connectors. One feedthrough is connected to an EDS. To test the two EDS plates in the chamber sequentially, the cables are switched to the alternate feedthrough. (b) Inside the feedthrough flange are four UHV Kapton-insulated high-voltage cables, each connected to an EDS electrode pad.

6.3.3 LabVIEW Program

LabVIEW is a widely used software platform for data acquisition, instrument control, and industrial automation. It features a graphical programming environment where users create commands by dragging and dropping visual elements, known as nodes, to control instruments such as the myRIO-1900. The graphical user interface (GUI) and block diagram shown in Figures [6.20](#) and [6.21](#) illustrate this process. Nodes, which perform specific operations, are connected by wires that define control signals. Constants and controls provide fixed values for nodes, such as timers, while the enclosing structure manages the flow of execution within the block diagram. In this example, the program controls waveform generators to emit square wave signals for a specified duration.

The program is configured to transmit a 10.5 Hz square-wave voltage signal at 2.5 V from the myRIO for 60 s. As detailed in Section [6.3.2](#), the myRIO's analogue signal output channel can provide a maximum output of 10 V. This voltage signal is amplified 300 times by the HV amplifier, resulting in a 1500 V peak-to-peak signal, which is then sent to the EDS.

According to Kawamoto et al., [2006], particle motion was predominantly synchronised with the wave at a low frequency of 10 Hz. As the frequency increased to 140 Hz, particles exhibited movement in the opposite direction. At even higher frequencies, such as 250 Hz, particles remained stationary and only vibrated. This behaviour was also observed during preliminary tests on the influence of frequency in this study, so a frequency of 10.5 Hz was selected. The program could not be initiated at exactly 10 Hz for reasons that are unknown.

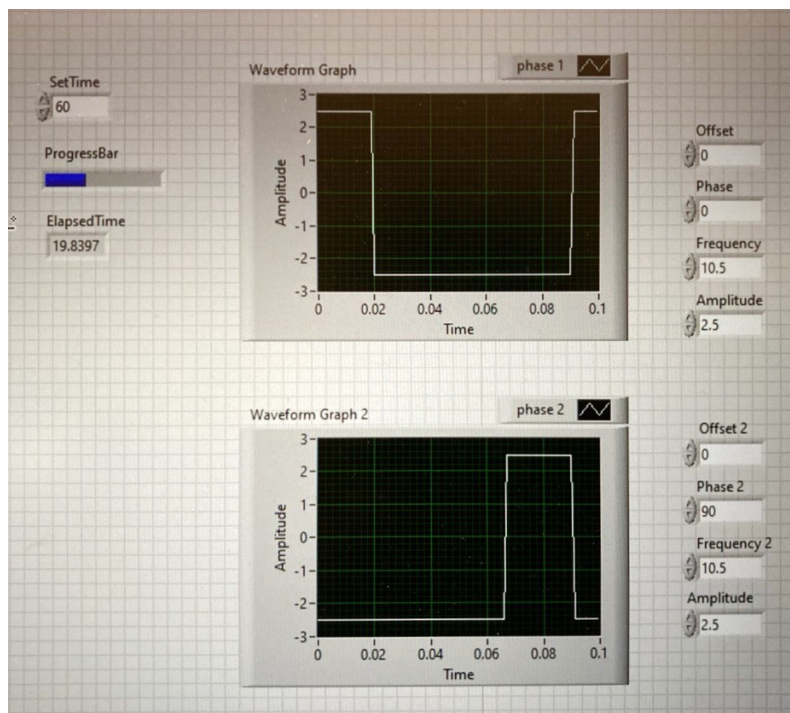


Figure 6.20: (a) LabVIEW GUI showing two input signals to the myRIO, each with a frequency of 10.5 Hz and a voltage amplitude of 2.5 V. The voltage amplitude is subsequently amplified by a factor of 300 using the HV amplifier.

6.3.4 High-Speed Camera

A high-speed camera was used to observe and track particle dynamics, allowing the acquisition of both qualitative and quantitative data for the experiments. The high-speed camera employed was the CP90-25P-M/C-72 CoaxPress camera from *Optronics*. It features four CoaxPress channels with a transmission rate of up to 6.25 GBit/channel. It is connected to a computer and to terabytes of frame grabbers for data storage. The camera's settings were adjusted using the high-speed digital video capture software *StreamPix* developed by *Norpix*.

Obtaining an optimal particle motion recording was challenging due to several factors. Firstly, the vacuum chamber had an inherent dark environment, further exacerbated by limited options for in-vacuum illumination. Secondly, the flat dust

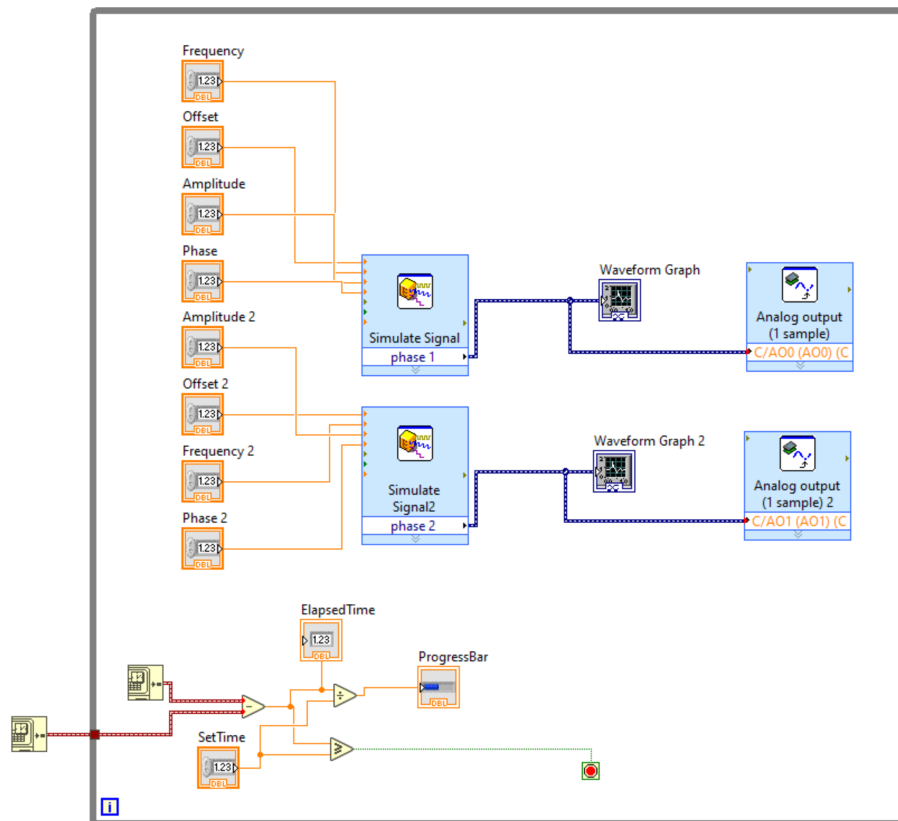


Figure 6.21: LabVIEW block diagram illustrating the nodes (individual icons) used to control waveform parameters, including frequency, voltage offset, voltage amplitude, and phase shift.

surface resulted in a shallow depth of field. Ensuring a larger area in focus required reducing the lens aperture to at least $f/8$ [¶], which was not feasible as it would significantly limit the amount of light reaching the camera sensor, leading to insufficient illumination for high frame rate recording. Achieving a balance between focus and brightness was a compromise. Ultimately, a larger aperture of around $f/5$ was employed, using a 50 mm $f/1.2$ lens from *Zeiss*.

The camera setup is depicted in Figure 6.22. The illumination intensity of 72000 Lux and the high-speed camera capturing 1500 frames per second were inadequate for capturing the initial ballistic trajectory of particles in clear, consecutive frames. While achieving faster frame rates was technically feasible, it would have substantially compromised image clarity, rendering the marginal improvement in frame rate not justified.

[¶]The larger the f -number, the smaller the aperture size of a camera lens.

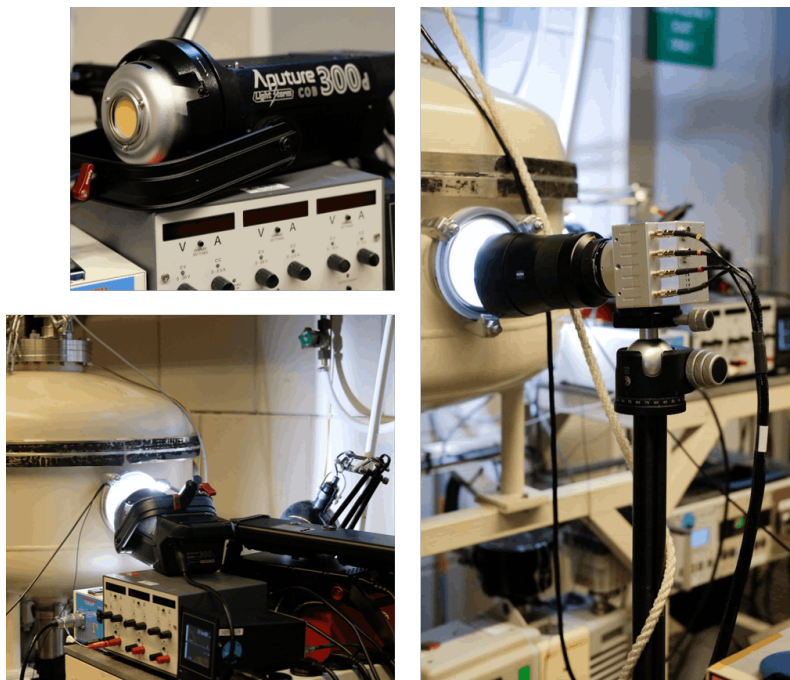


Figure 6.22: On the left, the photographs show the illuminating element for the high-speed camera. The photograph on the right shows the camera looking through the vacuum chamber feedthrough, which has a transparent flange.

6.4 Dust Removal Efficiency Quantification

Two methods are employed to determine the Dust Removal Efficiency (DRE) of the EDS on lunar simulant particles: **weighing** and **solar cell efficiency**. While these methods share similarities, they have slightly different implications for applications on the lunar surface, as the mass removed does not necessarily correlate with optical transparency. In the context of this paper, 'DRE' refers to a quantitative measure of the efficiency of the EDS in removing dust particles from a surface in a given environment (such as vacuum, UV irradiation, temperature, etc.), typically expressed as a percentage. A high DRE indicates that the system can effectively remove a significant portion of the dust particles present on the surface.

6.4.1 Weighing

This method provides a direct quantification of the physical amount of dust removed, regardless of the size or distribution pattern. The DRE is calculated by comparing the dust mass on the surface before and after EDS activation, which represents the quantity of dust that remains on the effective area of the EDS, i.e. the area above the spiral electrodes. Dust outside this area is brushed away prior to weighing. The percentage of dust removed is then calculated from these measurements:

$$DRE_{mass} = \frac{M_{after}}{M_{before}} \times 100, \quad (6.2)$$

where M is the mass.

6.4.2 Solar Cell Efficiency

The second approach explores a prospective application of EDS technology on the Moon, involving the evaluation of light transmission through the dust layer using an SA. EDS application on SA has been studied for lunar use (M. K. Mazumder et al., 2007; Kawamoto et al., 2011) and further adapted for terrestrial use (M. Mazumder et al., 2013; Kawamoto et al., 2015; Altıntaş et al., 2021). The reason for studying light transmission, as discussed above regarding dust adhesion, is that stubborn sub-micron particles are often too light for scales to detect, yet they are still present and impactful. As a result, the SA might still experience some opacity from residual dust grains that impede light transmission.

The electrostatic adhesion depends on the quality of the vacuum. Discharging occurs through several mechanisms such as conduction, solar wind plasma currents and photoelectric emission. Case in point: in the lunar environment, the lack of the latter two mechanisms in crater regions might prolong the discharge time of particles, and in vacuum experiments, strong electrostatic adhesion was observed to persist for several days with no significant degradation at 10^{-10} Torr, around 1.3×10^{-9} mbar. According to Berkebile et al. (2012), a vacuum of at least 10^{-5} mbar is necessary to retain charge adhesion on fluorinated ethylene propylene (FEP) particles.

This method helps to assess the extent of the fine-grain issue. The SA test uses the same setup as the regular EDS test, but here the SA is added below the transparent EDS plate with a glass coating (see Figure 6.15).

One should take into consideration that not all incident light reaches the SA surface, as it may be absorbed or scattered by particles within the dust layer. The SA short circuit current (I_{sc}) here is measured at three instances: 1) when the EDS plate is dust-free (I_{sc}^0), 2) after dust is deposited on the EDS (I_{sc}^1) and 3) after EDS has been activated (I_{sc}^2). The silicon solar cells typically have a high quantum efficiency in the range of 300–1100 nm, and the energy from a halogen lamp (400–700 nm) is converted to I_{sc} of the SA. To compare the absolute cleanliness, a calculation is made against I_{sc}^0 :

$$R_{beforeEDS} = \frac{I_{sc}^1}{I_{sc}^0} \quad (6.3)$$

$$R_{afterEDS} = \frac{I_{sc}^2}{I_{sc}^0} \quad (6.4)$$

The ratio indicates the opacity relative to the dust-free EDS plate; the closer the

ratio is to 1, the cleaner the EDS plate. Therefore, the higher the quantity of dust, the lower RR will be. This approach allows for assessing the effectiveness of the EDS under varying initial dust quantities. For instance, initial low dust coverage (e.g., 10 mg) results in high transparency due to minimal dust deposition, so the relative change in I_{sc} after dust removal remains small. If a percentage increase in efficiency were calculated, I_{sc} would appear to scale with the initial dust coverage, decreasing as dust coverage decreases, as this represents a relative change.

Assessment of Dust Deposition Uniformity

First, the dust deposition method was examined to ensure the reproducibility of the dust layer. However, it is only an estimation, as reproducing the exact granular arrangement of the dust particles is impossible. This assessment evaluates the specific pattern of dust deposition on the EDS surface by using the software ImageJ (Rasband, 1997) to calculate the percentage of dust coverage in a given image. The software converts the image into a binary format, separating the particles (foreground) from the background, and then calculates the percentage of pixels representing the particles in the total area.

Figure 6.23 shows the coverage as a percentage of the total surface area covered by dust on a transparent EDS surface, using LHS-1 and LMS-1 simulants in quantities of 10 mg, 50 mg, 80 mg and 200 mg of dust on a $\varnothing 80$ mm circular arrangement of electrodes. These quantities are converted to 0.20, 1.00, 1.59 and 3.98 mg/cm², respectively (see 6.1). This evaluation confirms the reproducibility of the dust deposition method across different dust types. The variation in coverage between the two simulants is negligible, indicating a consistent distribution.

6.5 Protocol

This section outlines a protocol for preparing the experimental setup, designed to maintain integrity and optimise performance by ensuring precision and reliability in each test and repetition. Key procedures include sample baking, cleaning, deposition, setting up the vacuum chamber, activating instruments, recording data, and conducting post-experiment measures.

The particles are subjected to either charging ('UV' case) or partial discharging ('transient-UV' case) using the same UV source. In the 'UV' case, continuous exposure to UV while the EDS is activated charges the particles through the photoelectric effect, while in the 'transient-UV' case, turning off the UV source before EDS activation partially discharges some dust particles through photoionisation. However, as our system comprises layers of granular, poorly conducting particles, it is unclear to what extent the dust would be neutralised by such an exposure. It is therefore not possible to discharge all particles in this scenario. The introduction of a continuous charging mechanism (here: UV, but on the Moon, also ambient plasma) forces every particle out of charge equilibrium in a stochastic manner, as photoelectrons can be

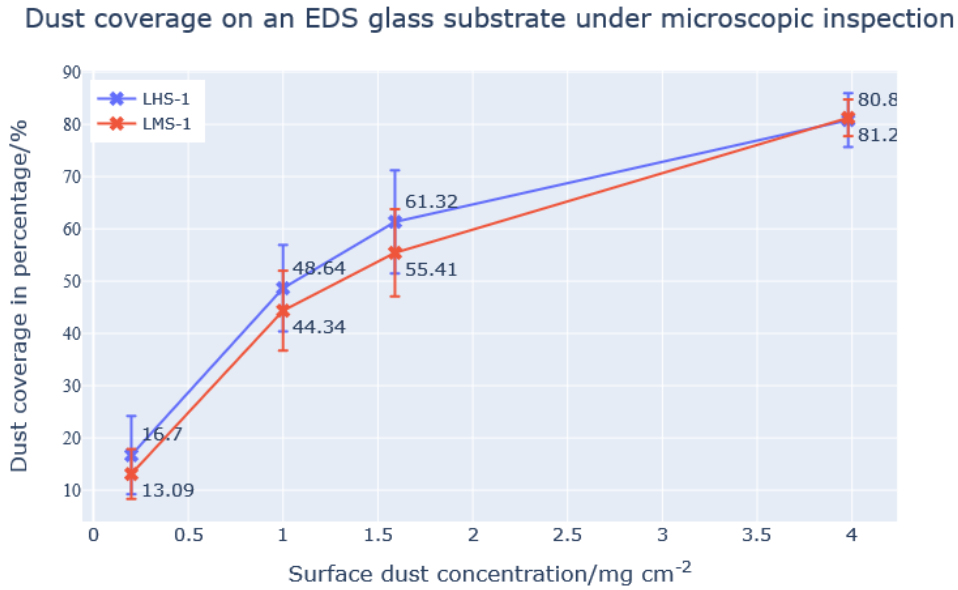


Figure 6.23: Mean percentage values with standard deviations of dust coverage for each simulant species on an EDS with a transparent coating. Higher percentages indicate denser particle populations.

emitted and collected by the grains. This allows electrostatic repulsion to act on grains that initially were not carrying charge or had identical charge with respect to surrounding particles. Without a charging mechanism, these grains would otherwise not be affected by electrostatic forces. A baseline case, termed 'no-UV' in vacuum, was also created for comparison. These cases are summarised in Table 6.1 for clarity.

Case	Description
UV	Continuous irradiation before and during EDS activation.
Transient-UV	Brief irradiation before EDS activation (~ 1 min).
No-UV	Only vacuum, no UV irradiation.

Table 6.1: The different UV test cases for the EDS.

1. Turn on the vacuum chamber 24 hours before the experiment until it reaches 10^{-6} mbar.
2. Bake the samples in a glass dish with glass lid in the oven for a minimum duration of 24 hours, or as long as possible. Retrieve the samples only before each dust deposition.
3. Clean the EDS glass surface with isopropanol and lint-free cloth before changing to a new sample. If a microscope is available, inspect for remnants; otherwise, skip this step. Keep the vacuum chamber closed with the vacuum pump running when not in use.

4. Determine the net glass weight, excluding the dust simulants.
5. Deposit the sample onto the glass surface using the dust deposition system, ensuring the deposited amount is within the 190 mg to 210 mg range.
6. Weigh the EDS glass with the sample again without the dust deposition cylinder to double check that no dust was lost.
7. Capture an image of the glass with a white (or black, depending on the simulant color) background for optimal contrast.
8. Re-pressurise the vacuum chamber and place the glass inside. Connect high-voltage cables to the EDS electrode pads using polyimide tape, and attach thermocouples with aluminium tape.
9. Begin the vacuum pump-down process: start with the main pump, and when the pressure reaches approximately 10^{-1} mbar, activate the turbomolecular pump. This process may take overnight to reach the final pressure of 10^{-6} mbar, depending on chamber content.
10. (If testing with temperature variation) When the pressure reaches approximately 10^{-4} mbar, initiate temperature control to stay above the dew point. Set temperature to -40°C .
11. (If testing with temperature variation) When the pressure reaches 10^{-6} mbar, record the current pressure and temperatures from the thermocouples attached to the EDS, thermal plate, and chamber.
12. Activate the high-power LED for high-speed camera recording. Adjust brightness and shadow effects to maximise clarity and contrast.
13. Power the EDS by applying LabVIEW-controlled high-voltage signals, amplified via myRIO through an HV amplifier. Turn on the HV amplifier, reset the SDN to unlock the switch, and switch all HV channels on. Start the LabVIEW run.
14. Run the HV for 1 minute with the chosen parameters while recording activation with the high-speed camera.
15. After the run, stop the recording, turn off the HV amplifier, and connect the cables to another feedthrough for the second EDS plate in the chamber.
16. Turn on the UV lamp for 1 minute.
17. Repeat steps 10–14 for the second EDS.
18. (If testing with temperature variation) After completing the test, adjust the thermal plate temperature to 30°C and wait until all chamber components reach at least 15°C to prevent condensation when opening the chamber.

19. Turn off the turbomolecular pump, then the main pump. The fan of the turbomolecular pump is still running at this point.
20. Depressurise the vacuum chamber using a nitrogen flush: slowly open the nitrogen valve to gradually stop the turbomolecular pump fan. Monitor the pressure to ensure proper deceleration of the fan.
21. Open the vacuum chamber once the pressure reaches 1 bar.
22. Remove the separation board from the aluminium structure for easier access.
23. Remove the EDS plates from the chamber.
24. Gently and swiftly brush away dust from the non-active areas of the EDS surface using a brush.
25. Weigh the glass with the remaining sample immediately.
26. Capture an image of the EDS plate with an appropriate background color for contrast.
27. Clean the aluminium structure of any dust using a vacuum cleaner and an isopropanol wipe. If necessary, remove it from the chamber before cleaning.
28. For the next test, repeat the protocol from step 2. If no further runs are planned, close the vacuum chamber and maintain a vacuum with the main pump. Periodically bake out the vacuum chamber with the thermal plate as needed.

6.5.1 Limitations and Constraints

Despite planning and preparation, it is important to address inherent limitations and procedural constraints to identify potential discrepancies in results, provide explanations for possible errors, and suggest ideas for future improvements.

There are several aspects of limitations in the sample preparation stage. Starting with achieving identical initial samples for experimental studies on granular matter: no two extractions of the dust sample were ever identical and the author acknowledges that complete replication of conditions for each experiment is not possible. To reduce the inherent randomness, obtaining sufficient statistical data for calculating an average representation was implemented. This means that a typical EDS test with a specific simulant type and a specific coating material would be tested at least three times.

To minimise moisture condensation inside the vacuum chamber and on the surfaces of the dust samples and EDS system, preparation time was kept to a minimum as a general practice. However, it must be acknowledged that there was a transfer time between extracting the samples from the vacuum oven and placing them into

the vacuum chamber. Consequently, some of the effects of the baking process were unavoidably reversed to a certain extent beyond control. This limitation arises from the inability to prepare the samples in a continuous high-vacuum environment. A solution to this would be an in-situ dust distribution system. This would fundamentally alter the charging and discharging behaviours of the dust grains. Further discussion on this will be included in the results section.

References

- Abbas, M. M. et al. (2007). “Lunar dust charging by photoelectric emissions”. In: *Planetary and Space Science* 55.7-8, pp. 953–965.
- Altıntaş, M. and S. Arslan (2021). “The study of dust removal using electrostatic cleaning system for solar panels”. In: *Sustainability* 13.16, p. 9454.
- Berkebile, S. and J. Gaier (2012). “Adhesion in a vacuum environment and its implications for dust mitigation techniques on airless bodies”. In: *42nd International Conference on Environmental Systems*, p. 3465.
- Calle, C. I. et al. (2004). “Electrodynamic shield to remove dust from solar panels on Mars”. In: *Proceedings of the 41st Space Congress, Cape Canaveral*.
- Calle, C. I. et al. (2013). “Electrodynamic dust shields on the international space station: Exposure to the space environment”. In: *Journal of Electrostatics* 71.3, pp. 257–259.
- Chesnutt, J. K. W., B. Guo, and C.-Y. Wu (2019). “Numerical analysis of the effects of particle-particle interactions and particle size on the performance of an electrodynamic dust shield”. In: *Journal of Electrostatics* 98, pp. 58–68.
- Dubey, S., J. N. Sarvaiya, and B. Seshadri (2013). “Temperature dependent photovoltaic (PV) efficiency and its effect on PV production in the world—a review”. In: *Energy Procedia* 33, pp. 311–321.
- Grard, R. J. L. (1973). “Properties of the satellite photoelectron sheath derived from photoemission laboratory measurements”. In: *Journal of Geophysical Research* 78.16, pp. 2885–2906.
- Hamamatsu Photonics K.K. (2024). *VUV Lamp TLSZ1037E User Manual*. URL: https://www.hamamatsu.com/content/dam/hamamatsu-photonics/sites/documents/99_SALES_LIBRARY/etd/VUV_TLSZ1037E.pdf.
- Johnson, C. E. et al. (2005). “Effect of particle size distribution on the performance of electrodynamic screens”. In: *Fourtieth IAS Annual Meeting. Conference Record of the 2005 Industry Applications Conference*. Vol. 1. IEEE, pp. 341–345.
- Kawamoto, H. and N. Hasegawa (2004). “Traveling wave transport of particles and particle size classification”. In: *Journal of Imaging Science and Technology* 48.5, pp. 404–411.
- Kawamoto, H., K. Seki, and N. Kuromiya (2006). “Mechanism of travelling-wave transport of particles”. In: *Journal of Physics D: Applied Physics* 39.6, p. 1249.
- Kawamoto, H. and T. Shibata (2015). “Electrostatic cleaning system for removal of sand from solar panels”. In: *Journal of Electrostatics* 73, pp. 65–70.

- Kawamoto, H. et al. (2011). “Mitigation of lunar dust on solar panels and optical elements utilizing electrostatic traveling-wave”. In: *Journal of Electrostatics* 69.4, pp. 370–379.
- Masuda, S. et al. (1972). “Confinement and transport of charged aerosol clouds by means of electric curtains”. In: *The transactions of the Institute of Electrical Engineers of Japan* 92.1, pp. 9–18.
- Mazumder, M. et al. (2013). “Characterization of electrodynamic screen performance for dust removal from solar panels and solar hydrogen generators”. In: *IEEE Transactions on Industry Applications* 49.4, pp. 1793–1800.
- Mazumder, M. K. et al. (2007). “Self-cleaning transparent dust shields for protecting solar panels and other devices”. In: *Particulate Science and Technology* 25.1, pp. 5–20.
- National Instruments (2024). *myRIO-1900*. URL: <https://www.ni.com/nl-nl/shop/model/myrio-1900.html> (visited on 2024).
- Rasband, W. (1997). *ImageJ*. <https://imagej.nih.gov/ij/>. Version 1.53e.
- Saeidpour, S. et al. (2023). “Effect of electrode design and dust particle size on electrodynamic dust shield procedure”. In: *Physics Open* 14, p. 100131.
- Sayyah, A. et al. (2016). “Electrostatic force distribution on an electrodynamic screen”. In: *Journal of Electrostatics* 81, pp. 24–36.
- Staff, British Standards Institute (1992). *Code of Practice for Control of Undesirable Static Electricity. Recommendations for Particular Industrial Situations*. B S I Standards. ISBN: 9780580200182. URL: https://books.google.nl/books?id=gR7_PAAACAAJ.
- Tilley, R. J. D. (1975). *Nonstoichiometry, diffusion and electrical conductivity in binary metal oxides*.

7 Measurement of Dust Removal Efficiency

The content of this chapter is an extended version of a submission to *Advances in Space Research* under the title "Electrodynamic Dust Shield Efficiency Characterization Under UV in Vacuum for Lunar Application". The primary objective of this study is to investigate how the charging of irregularly-shaped dust grains, in conjunction with an external non-uniform electric field, affects dust dynamics. To simulate a key dust-charging mechanism on the lunar surface, Vacuum Ultraviolet (VUV) radiation was artificially introduced, producing both positively and negatively charged particles.

The particle charging mechanisms are extensively discussed in Section [2.2](#). This section will present quantitative data on the effect of UV radiation, and thereby the photoelectric charging effect, on the dust removal efficiency of the Electrodynamic Dust Shield (EDS) for selected lunar simulants, LHS-1 and LMS-1. The data will cover various particle sizes, quantities, and surface materials. Simulation work analysing the electric field strength, electric potential, and Dielectrophoretic Force (DEP) forces at various locations above an EDS surface was conducted to understand the forces at play and their respective contributions to particle dynamics.

Structure Outline

The results will be presented as both quantitative and qualitative data. The quantitative data will encompass the measured DRE under various UV conditions and with different coating materials, exploring the application of EDS as a dust mitigation mechanism. The qualitative data will detail observations from the experiments what are crucial for understanding dust dynamics but are difficult to quantify. These include preliminary tests with baked and unbaked simulants, tests in atmospheric conditions, voltage responses of grains, and high-speed camera footage for tracking particle motions.

Each research topic will be followed by a discussion, and a comprehensive discussion will be provided at the end to address overall trends and analyses. Finally, a simulation with a simplified EDS system setup will be presented to investigate the significance of the DEP force in our system.

7.1 Quantitative Data

This section presents the response of the EDS system with various material coatings and simulant types under different UV conditions and discusses the impact of UV exposure on the DRE. The system's response is analysed in terms of the mass of dust removed, and observations made with an optical microscope are compared with their correlation to solar cell output.

7.1.1 Response to Different UV Conditions

The first question is: How does the presence of continuous UV radiation affect the dynamics of dust grains when subjected to the electric field of the EDS? For this, three UV scenarios were created, which have been detailed in Section 6.5 in Table 6.1. Previous studies have suggested that charge deposition within the regolith, especially on adjacent grains, can result in repulsive forces affecting entire grain areas. They may experience electrostatic repulsion due to the presence of microcavities (Wang et al., 2016; Carroll et al., 2020), which increases the effectiveness of external fields in mobilising dust. This becomes particularly crucial when operating an EDS system while irradiating simulants with a UV source, serving as a proxy for natural dust charging. Figure 7.1 is a top-view of the aftermath of EDS activation with LMS-1 80–100 μm simulant as an example, with (left) and without (right) UV irradiation. A visibly smaller quantity of particles remained on the surface that had been exposed to UV.

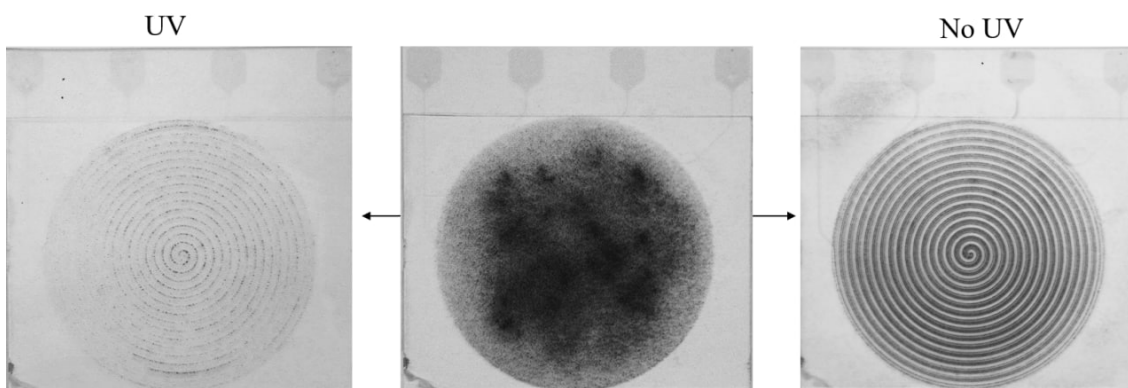


Figure 7.1: A comparison on the dust removal state of 200 mg of LMS-1 80 μm to 100 μm before (middle) and after EDS activation with or without UV irradiation (left and right, respectively).

To quantify dust removal in each scenario, Figure 7.2 presents a bar chart depicting the response of LHS-1 and LMS-1 under various UV irradiation conditions with activated EDS, as assessed using the weighing method. DREs (by mass) of different species of simulants on a glass coating, with UV-irradiated simulants shown in blue, compared to transient-UV exposure in orange, and no-UV exposure in red. Approximately 200 mg of dust was used in each test; for each size range (25–50 μm and 80–100 μm), the experiment was repeated at least three times, often more. The

error bars represents the standard deviation of the results of repeated runs.

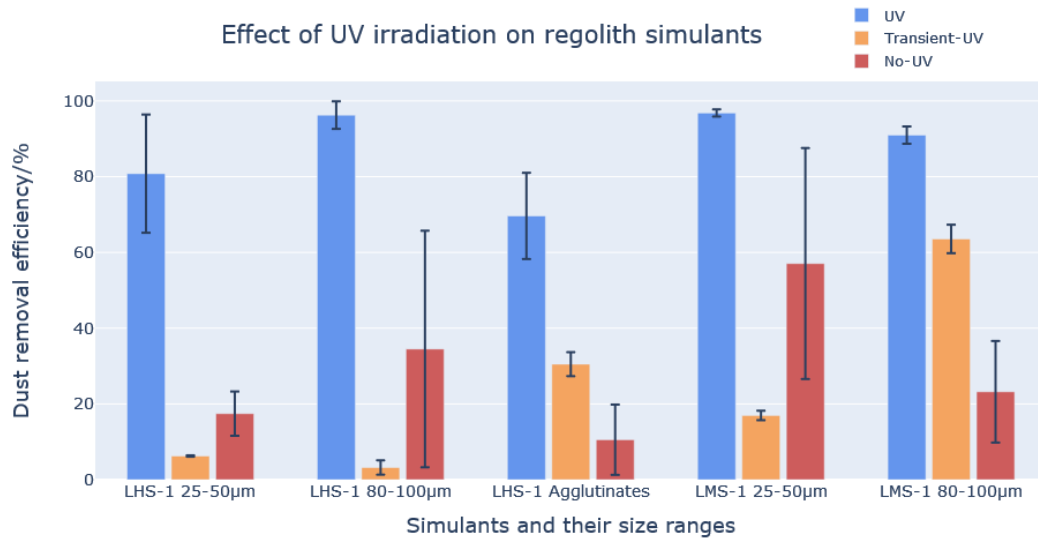


Figure 7.2: Dust Removal Efficiencies of the Electrodynamic Dust Shield in different UV conditions with various simulant types are shown. Five simulant types were tested under three distinct UV conditions. The figure presents the average DRE values obtained from multiple tests, with error bars representing the standard deviation for each case.

Discussion

In the **UV** case, a clear and distinct difference in the dust removal rate is observed compared to the other two cases (**transient-UV** and **no-UV**). The data suggest that for particles to be repelled by the electric field at the same field strength, they must acquire a greater charge from photoemission, as the force experienced by a charged particle is proportional to the magnitude of its charge (Equation 5.1). In addition, since photoelectric charging dominates, the effect of initial charging conditions prior to UV irradiation is insignificant.

The data for the cases of **transient-UV** and **no-UV** exhibit little to no discernible general pattern to be followed. The large error bars in the **no-UV** cases are likely due to variations in the initial charge states of the dust layer, which are caused by uncontrolled surface conditions and tribocharging. In the case of **transient-UV**, most of the particles are assumed to be neutralised by UV, but the extent to which the charges are neutralised has not been directly verified through measurement. Upon examining the DRE values, it was observed that LHS-1 grains were largely neutralised according to Equation 5.1, whereas LMS-1 grains exhibited less neutralisation, as evidenced by the high DRE observed for LMS-1 grains in the 80-100 µm range.

In the improbable scenario where all particles are neutralised ($q = 0$), a comparison

of Equation 5.1 and Equation 5.4 suggests that movement can only be induced by the DEP force in the **transient-UV** case. However, it is more likely that there are (sub)layers of particles that have not been fully neutralised, which allows an electrostatic repulsive force to still have an effect on dust removal.

A quick test was conducted to assess how the duration of UV exposure influences the effectiveness of EDS. The DRE of 200 mg of LHS-1 in the 80–100 μm size range was examined under UV exposure durations of 5, 10, 15, and 30 minutes. The standard deviation of these values was approximately 2.53 percentage points, representing 2.65% of the mean value (95.73%). The results show that the initial UV irradiation duration before EDS activation does not significantly affect the final DRE outcome. No apparent correlation between exposure duration and DRE was observed, suggesting that an equilibrium charging state is reached within a few minutes, if not seconds. It is also possible that any charge neutralisation would be instantaneous.

The microscope images depicted in Figure 7.3 reveals a significant accumulation of simulant particles on specific electrodes, as also observed in Figure 7.1. The surface was inspected at ten different locations and the images were analysed using ImageJ to calculate an average for the surface coverage. These ten locations do not match between the 'before' and 'after' states. Here, we display only four specific locations chosen to represent different dust densities on the EDS. This accumulation results in one or two adjacent electrodes being covered with these grains on an otherwise effectively cleaned EDS surface.

Without further investigation, we cannot ascertain the exact cause of this phenomenon, but we speculate that particles, which are sufficiently charged to be mobilised but not ejected, may roll or jump between electrodes while carrying the same charge from photoemission, thus preferentially resting on one or two specific electrodes as the EDS is deactivated. We also cannot rule out manufacturing imperfections or operational errors, but it has come to our attention that this phenomenon has been documented in literature (Calle et al., 2004) and other laboratories in Japan and France (personal correspondence, Masato Adachi, Pierre Sarraillh).

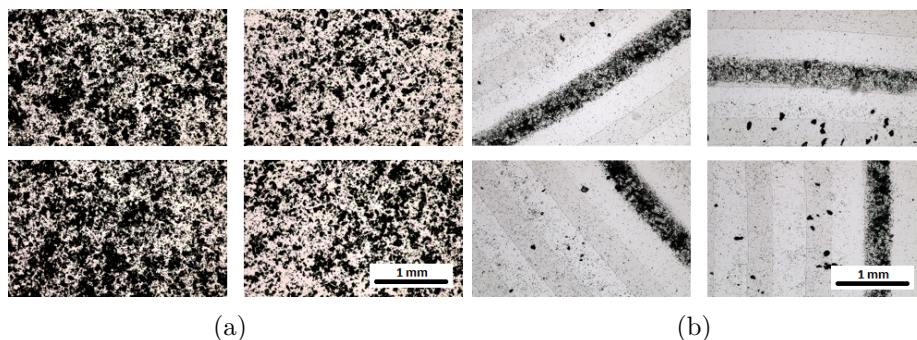


Figure 7.3: Snapshots of dusty EDS surfaces under an optical microscope. The images were taken before and after EDS activation, on random locations on the same EDS plate. 10 images were taken, only 4 are shown here. (a) before and (b) after EDS activation.

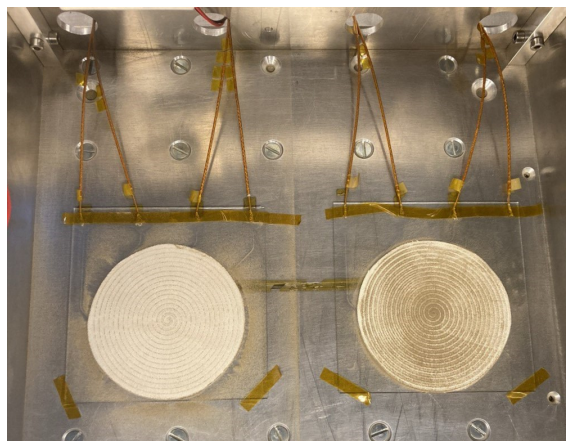
7.1.2 Response to Different Material Coatings

Materials commonly used in space applications were tested in this study to evaluate the effectiveness of the EDS across various coating materials. This section presents results from testing with Kapton (50 μm thickness), Beta cloth (200 μm thickness), and glass (100 μm thickness) for comparison. Figure 7.4 shows the tests with Kapton and Beta cloth in the vacuum chamber.

As described by Bechkoura et al. (2023), the electric field's effectiveness diminishes rapidly as it moves away from the electrode edges, and the height of the potential field lines depends on the spacing between electrodes. While this introduces another variable into the results and acknowledges the differing thicknesses of these coatings, the focus of this study remains solely on materials currently used in space applications. The specific material properties of the coatings are not further explored.



(a)



(b)

Figure 7.4: Photographs showing the 200 mg dust removal cases: (a) Kapton and (b) Beta cloth. For each case, the left side is the EDS case with UV exposure, while the right side shows the EDS case without UV exposure.

Figure 7.5 presents the results of the **UV** (blue) and **no UV** (red) tests on the three coating materials. With the exception of the 80–100 μm and LHS-1 agglutinate

simulants on 200 μm Beta cloth, all tests exhibit high DRE with UV exposure.

Discussion

A notable outlier is the performance of the Beta cloth for larger particle sizes (80–100 μm). This outcome was surprising in two ways: first, the electric field of the EDS was able to penetrate the substantial fabric material and remove a considerable amount of particles; second, a qualitative assessment of the test showed almost no movement of the dust particles, as if the EDS had not been activated at all. Even the LHS-1 agglutinates had a slightly better performance because the size range included smaller particles. The anomaly with the larger particles might be attributed to the fiber structure of the fabric, which allows dust of certain sizes to become wedged in the material, making mechanical frictional forces too strong to overcome. There is something very specific about the 80–100 μm grains, but without further experimentation to confirm, it is speculated that a combination of grain size, fiber size, and HV frequency may be responsible for this effect. Figure 7.6 shows a Beta cloth fabric coated with lunar dust. The thread spacing of the fabric is approximately the same as the size of the dust grains, suggesting that the matching dimensions may contribute to the dust's adherence to the fabric. It has been shown that particle size range plays a role in the way they are transported across an AC field (Gu et al., 2022). Figure 7.7 depicts how finer particles are trapped in the interstices of the fabric. Smaller particles on Beta cloth, which may only have a single contact point with the material, are more easily lifted than larger ones, albeit with slightly less ease than other coatings due to the fibrous surface.

7.1.3 Solar Cell Output and Optical Microscope Observations

The previous tests established that UV irradiation of the dusty surface increases the DRE. Here a test with SA is conducted to demonstrate an application of EDS and verify that the high DRE rate also translates to high optical transparency at various dust quantities. Experimentally, we noted that the finest sizes were not easily removed by the setup, but the quantity was often too small to be differentiated by weighing. As a result, the SA might still experience some reduction in power output from residual dust grains that impede light transmission. Comparisons of SA current output are presented as a ratio (Equations 6.3 and 6.4). The data is presented as the change in Short-Circuit Current (I_{sc}) with respect to an uncontaminated surface (I_{sc}^0) for LHS-1 and LMS-1 at 10 mg, 50 mg, 80 mg and 200 mg (translated to surface dust concentration, in mg cm^{-2}). A continuous monitoring of the I_{sc} during EDS activation would have been ideal, but this was unfortunately not possible with this setup.

Discussion

The cleanliness level appears consistent across various amounts of dust and simulants, as suggested by the consistently high ratios exceeding 0.9. The error margin

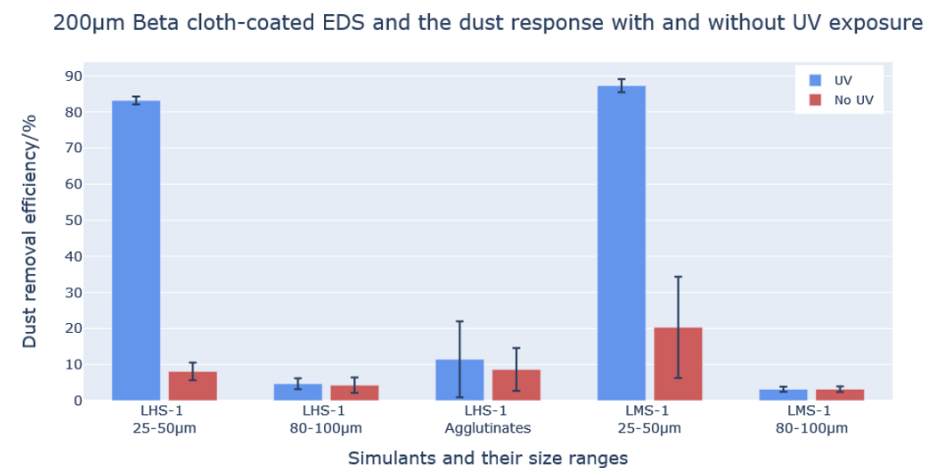
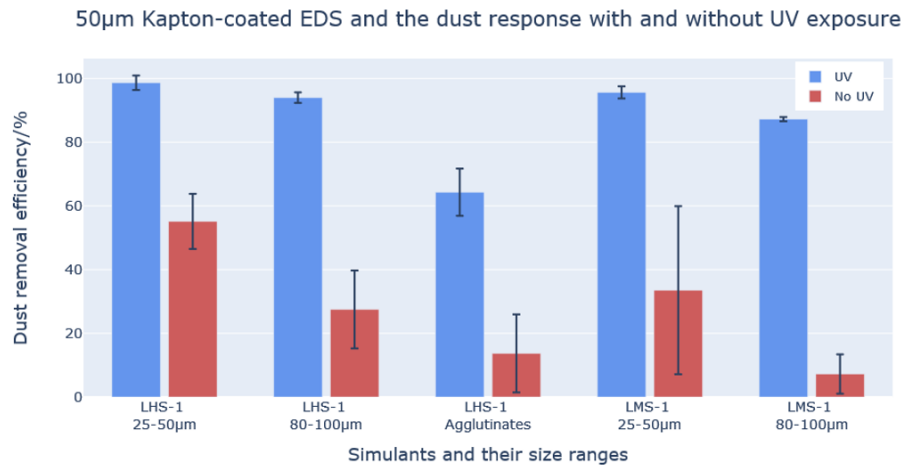
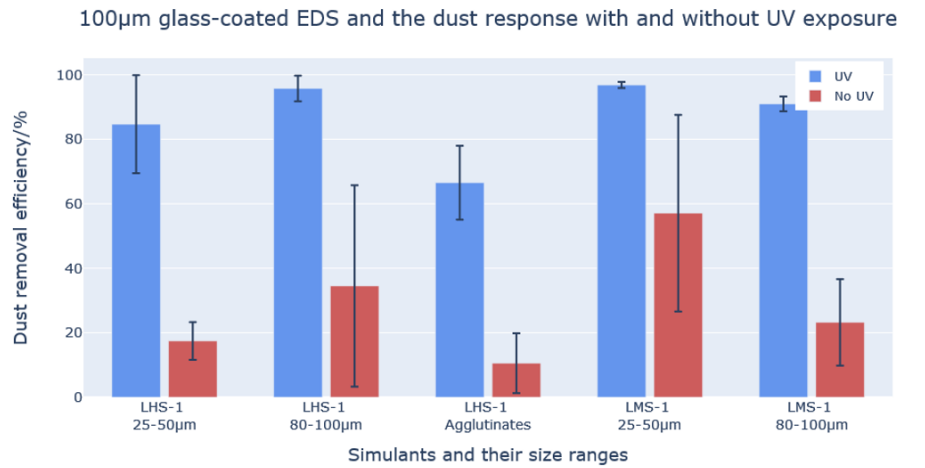


Figure 7.5: DRE comparison (by mass) of LHS-1 and LMS-1 simulants on three different EDS coatings: glass (top), Kapton (middle) and Beta cloth (bottom). Only the UV and no-UV cases are shown to highlight the effect of UV across different coatings.

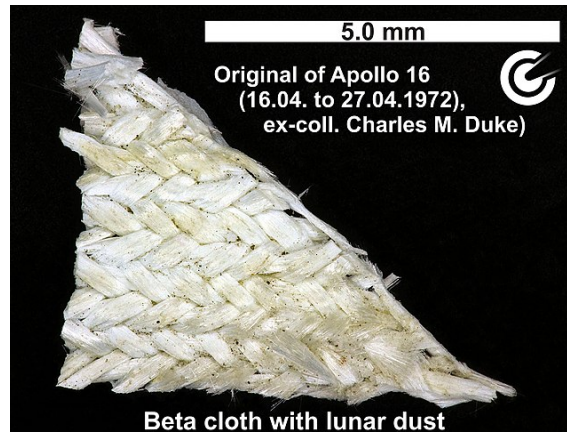


Figure 7.6: Apollo 16 Beta cloth with lunar dust trapped in the fabric. *Source: Wikimedia Commons, [link to image](#).*

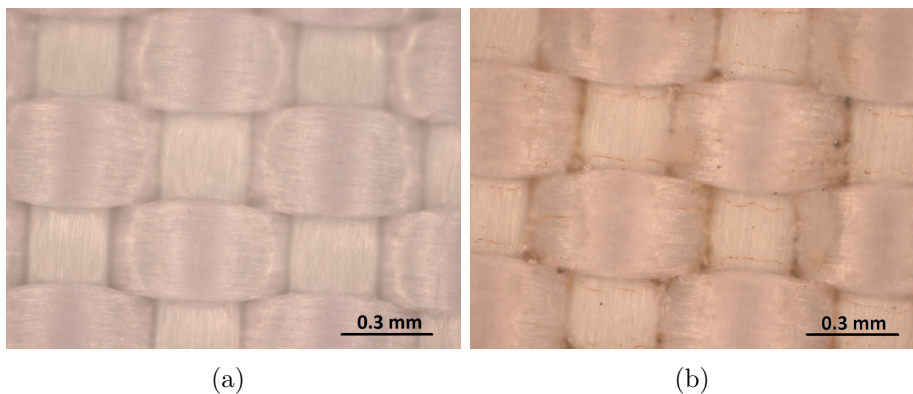


Figure 7.7: Optical microscope observation of Beta cloth usage. (a) Pristine sample of Beta cloth. (b) After a few uses for EDS dust test, which shows visible wear.

resulted in a ratio above 1. A similar result was also obtained by Calle et al. (2011). The lower transmission of LMS-1 can be attributed to the colour of the simulant, which is significantly darker than LHS-1. The latter has a high Feldspar content, which is white and results in more reflection onto the SA. The observed transmission loss from the SA output current also aligns with findings in the literature describing the impact of dust layers on photovoltaic performance (Katzan et al., 1991).

The correlation between the amounts of dust deposited onto the surface and the surface concentrations shown in Figure 7.8 is introduced as part of an experimental investigation into the scalability of solar cell output with the dust coverage area. The closer the ratio is to 1, the cleaner the EDS plate. This approach allows for assessing the effectiveness of the EDS under varying initial dust quantities. Initial low dust coverage (e.g. 0.5 mg/cm^2) results in high transparency due to minimal dust deposition, so the relative change in I_{sc} after dust removal remains small. The I_{sc} ratio appears to scale with the initial dust coverage, decreasing as dust coverage decreases. Testing with varying dust quantities was only conducted with the SA

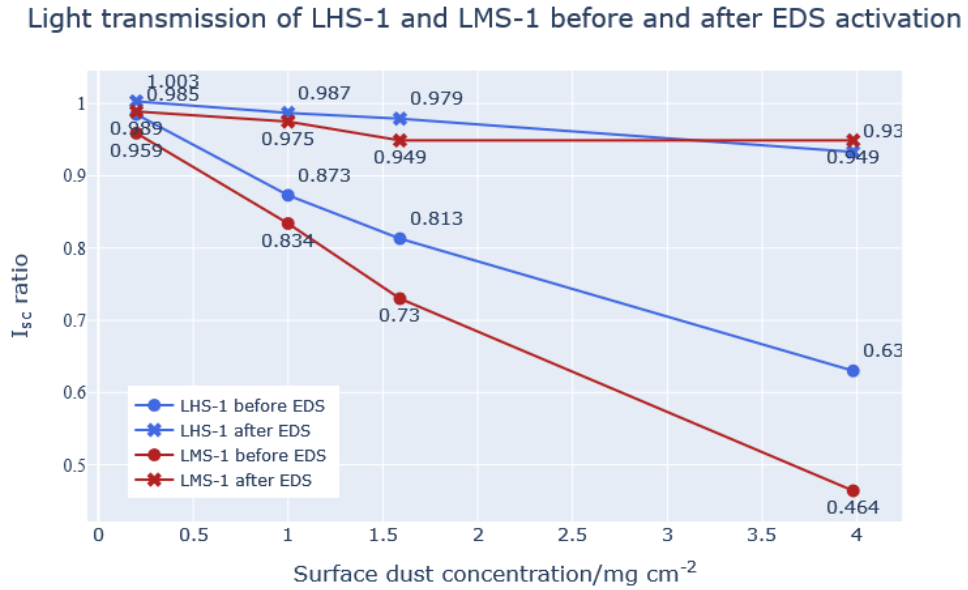


Figure 7.8: Solar cell array’s short-circuit current I_{sc} ratio for LHS-1 and LMS-1 at varying surface dust concentrations, before and after EDS activation. LHS-1 exhibited a higher initial I_{sc} (blue round dots), but both materials demonstrated similar I_{sc} values post-EDS activation across all surface dust concentrations (red and blue crosses).

measurements. Including this with all simulant and coating types would have been impractical due to the substantial volume of data that would have been generated. The results presented here could potentially be used to qualitatively predict the behaviour of other coatings and types of dust.

7.2 Qualitative Data

Throughout the experiment, qualitative observations were made to complement the quantitative data. In addition, some initial tests lacked sufficient maturity in the experimental setup to allow for a quantitative assessment, or did not yield enough data for definitive conclusions. Nevertheless, these observations were documented and still provided useful insights. In this section, the effects of baking the simulant and exposing it to ambient atmosphere, the influence of varying voltages on EDS efficacy (ranging from 300 to 1500 V), preliminary findings regarding temperature effects, and grain movements captured by the high-speed camera will be presented.

7.2.1 Unbaked Simulants and Atmospheric Testing

As previously mentioned, baking the simulant is a crucial step in replicating the lunar environment, given the negligible presence of moisture in the lunar vacuum. Some research indicated that simulant samples were used in the vacuum chamber without prior baking. In private communications, some researchers questioned the necessity of baking, speculating that brief exposure to air during transfer from the oven to the vacuum chamber would cause water to re-adhere to the grains.

The unbaked sample displayed much stickier characteristics, with clumpier particles, and achieved a less clean and even distribution. Additionally, it was thought that vacuum chamber outgassing prior to the EDS activation might suffice alone. Ideally, the vacuum chamber would serve as a vacuum oven before testing, but this approach would significantly extend the pump-down time due to the many components inside the chamber, and at 200°C, there is a risk of damaging some materials. Therefore, this study investigated whether baking indeed affects dust removal outcomes.

The tests presented in this section demonstrate the effects of residual moisture on particle surfaces and underscore the importance of its removal to accurately simulate lunar conditions. The results reveal a noticeable difference in dust grain behaviour between baked and unbaked samples in terms of dust removal efficiency. Furthermore, the contrast between baked and unbaked samples is even more pronounced under atmospheric conditions (i.e. 25°C and 45% RH). LHS-1 simulant was used in all tests, with no UV exposure.

Comparing Baked and Unbaked Samples in Air

Testing EDS with both baked and unbaked samples in air showed that the dust in the baked sample was removed more effectively and with larger force as evidenced from the spread of the dust, as seen in Figure 7.9. In contrast, the dust in the unbaked samples took considerably longer to be removed and tended to form heaps of grains that clumped together during EDS activation, remaining on the surface even after several minutes of cleaning. The phenomenon can be explained by the leakage current path provided by the water molecules present on the grain surface, which neutralises some of the charges. This phenomenon was also observed in the study conducted by (Mantovani et al., 2007), where a 10 Hz and 1200 V EDS configuration was tested under ambient conditions with JSC Mars-1 simulants (Figure 7.10). Interestingly, the JSC-1 lunar simulant was cleaned much more easily in comparison.

Comparing Baked and Unbaked Samples in Vacuum

Figure 7.11 shows the results of testing baked and unbaked samples in a vacuum. The contrast is even more stark than in the case in air; the unbaked sample (left) shows almost no movement of dust grains. The vacuum pump down outgassed the water molecules, effectively removing any charges from the particles in the process.

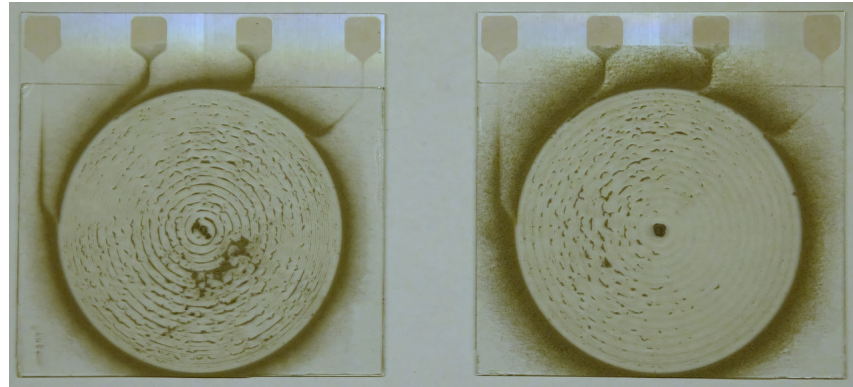


Figure 7.9: Photograph showing EDS tests conducted under atmospheric conditions with samples of LMS-1 25–50 μm grains. Left: Unbaked sample. Right: Baked sample. The unbaked sample showed greater retention in the effective area.

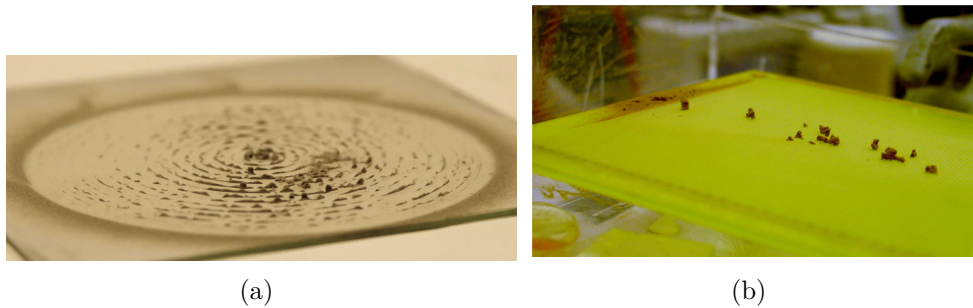


Figure 7.10: Similar observations of simulant clumping during atmospheric EDS tests, consistent with findings reported in the literature. (a) LMS-1 simulant clumps. (b) JSC Mars-1 simulant clumps. Source: (Mantovani et al., 2007).



Figure 7.11: Photographs showing EDS tests conducted under the same vacuum condition (no UV) with samples of LMS-1 25–50 μm grains. Left: Unbaked sample, showing almost no particle displacement. Right: Baked sample.

7.2.2 Voltage Amplitude Tests

A preliminary test was conducted to gauge the minimum working voltage for this particular EDS setup. The test intended to find the most suitable voltage amplitude for maximum cleanliness, while still protecting the mechanical integrity of the EDS plate from breakdown damage.

The voltage amplitude was incrementally increased from 300 to 1500 V in 300 V steps, with tests conducted both in the presence and absence of UV irradiation. Without UV exposure, particle movement was first observed at approximately 1200 V, becoming more pronounced at 1500 V. In contrast, under UV radiation, substantial particle movement initiated at 600–900 V, with no discernible difference in movement between 1200 V and 1500 V. Sparking occurred at voltages exceeding 1500 V. Based on these observations, 1500 V (± 750 V) was established as the optimal EDS voltage amplitude for this setup.

7.2.3 Temperature Effect

A thermal plate enabled cooling of the aluminium structure which supports the EDS plates to approximately -30°C . However, due to glass's excellent thermal insulation properties, temperatures measured on the EDS surface ranged from -3°C to 10°C , typically closer to the upper end of this range. Waiting to achieve sub-zero temperatures on the EDS plate alone required extended periods, and given the substantial effect of time on charge dissipation previously established, waiting for beyond 12 hours would not provide a valid comparison with the room temperature case (i.e. violating the principle of changing one parameter at a time), which usually takes about 5–7 hours to reach 10^{-6} mbar. Additionally, as dust grains are poor thermal conductors as well and their temperature could not be measured directly with a thermocouple, the exact grain temperature remained undetermined. One can only hypothesise that it exceeded the glass temperature. The vacuum chamber body maintained room temperature, while the temperature within the chamber cavity was not measured.

At very low pressures (e.g., 10^{-6} mbar), water typically sublimates directly into vapour, bypassing the liquid phase. Even with initial baking and temperature reduction, only after significant atmosphere evacuation (10^{-4} mbar), some residual moisture inevitably remains in the system. Although the precise temperature of the grains is uncertain, at 10^{-6} mbar, the system is well below water's triple point (611 Pa, 0.01°C). While the exact process and quantity of water and its form are unknown, preliminary tests demonstrated high DREs even without UV exposure, reaching values around 60–70%. This observation can be interpreted as either a different interaction between the grains and the EDS because of the temperature drop, or, also likely, a consequence of reduced vacuum pump-down time. As temperature decreases, the outgassing rate also decreases, allowing high vacuum to be achieved more rapidly and potentially leading to reduced charge dissipation. Moreover, if water molecules on the grains transition to ice, they become effectively "stuck" on the

grains, preventing their removal during outgassing and thus preserving the charge.

7.2.4 High-Speed Camera Imaging

A high-speed camera captured dust particle motion and trajectories. However, due to equipment limitations and time constraints, accurate particle tracking and quantitative analysis of the frames were not possible, so the footage was used solely to observe any notable dust dynamics.

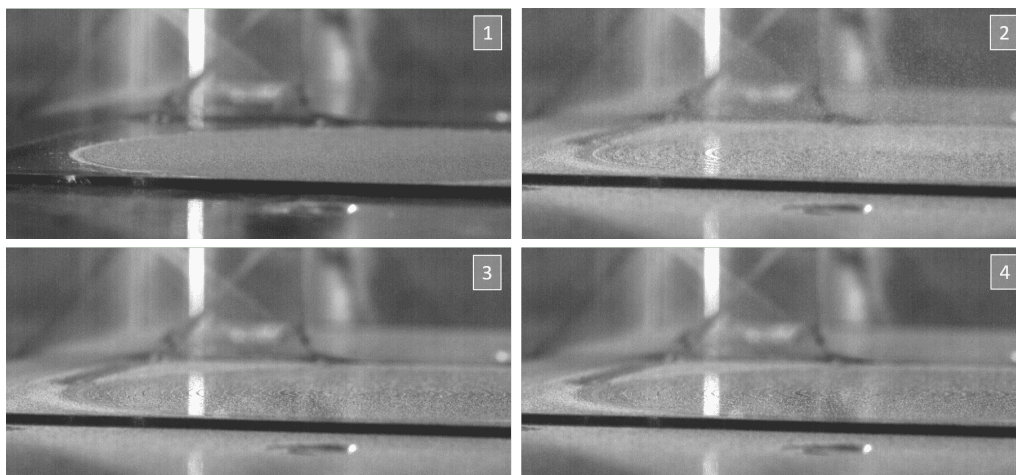


Figure 7.12: High-speed camera frames capturing 25–50 μm LMS-1 simulants at times 0 s, 1 s, 5 s, and 60 s.

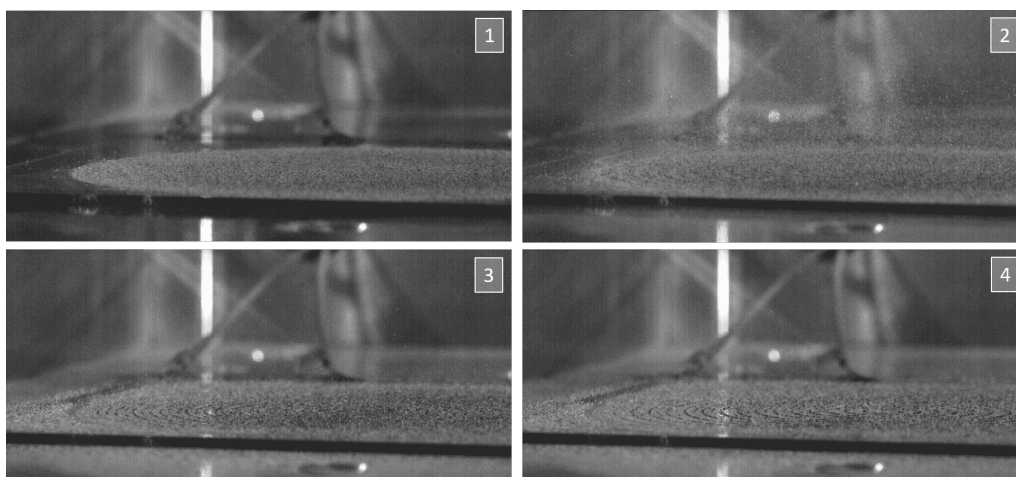


Figure 7.13: High-speed camera frames capturing 80–100 μm LMS-1 simulants at times 0 s, 1 s, 5 s, and 60 s.

Figures [7.12](#) and [7.13](#) present snapshots from high-speed camera videos capturing the migration of simulants across the EDS surface. The images show the progression at 0 s, 1 s, 5 s, and 60 s (from top-left to bottom-right) of EDS coupled with continuous UV irradiation on 200 mg of 25–50 μm LMS-1 over a 60 s period. The majority of dust particles are repelled from the EDS area within the first 5 seconds, typically

reaching maximum cleaning efficiency after 30-40 seconds. Beyond this time period, the particles lack sufficient force to move outside the effective area, resulting in minimal movement and remaining largely stationary, if there was any that stayed on the surface. Observation also shows that UV-irradiated particles exhibit higher velocities compared to those not exposed to UV or irradiated only briefly. Due to the inherent difficulty in clearly capturing micron-sized particles, only a qualitative assessment of the relative speeds has been conducted.

7.3 Discussion

7.3.1 Comparison with Literature Results

The non-UV DRE efficiencies recorded in this experiment are remarkably lower than similar type of experiments conducted by Calle et al. (2011) and Kawamoto et al. (2011), both achieving a DRE of over 90% without the use of UV radiation, compared to a median of $\sim 30\%$ in our case. The difference between their findings and this study may stem from variations in the simulant species (i.e. different chemical compositions), but a major difference is thought to lie in the dust deposition methodology and the duration for which the dust was allowed to discharge before activating the EDS (i.e. the vacuum pump-down time), which was likely considerable in this setup.

Calle et al. (2011) used unbaked JSC-1A simulant with particle sizes ranging from 50–75 μm with an in-situ dust deposition system that introduced dust grains under (presumably) vacuum conditions, enabling tribocharging and strong charge retention of the grains. Similarly, Kawamoto et al. (2011) tested FJS-1 simulants in air and at low vacuum, which is speculated to result in a much shorter pump-down time than in our experiments (5–7 hours), and samples with dust that have interacted and discharged much less with the environment (Cruise et al., 2023).

Comparably long pump-down time may thus have been enough to discharge much (at least the top layers) of the dust samples across all experiments, and that the transient-UV case, albeit with a UV-lamp explicitly designed to discharge surfaces in the lab with a short exposure, actually reintroduced a state of charge, via photoemission (Wang et al., 2016), on some dust categories, leading to slightly higher DREs in some cases, as seen in Figure 7.2. Alternatively, it is also possible that the short UV exposure was sufficient to alter the adhesion forces at play. This reasoning would also lend an explanation to the smaller spread of DRE across all transient-UV cases compared to the non-UV cases, but further investigation is needed.

7.3.2 Dust Particles Less than 25 μm

Grains in the sub-micron range are particularly challenging to remove due to prevailing adhesion forces. A significant portion of lunar regolith consists of particles smaller than 25 μm , which exhibit strong adhesion not only to coating surfaces but

also to nearby larger particles. Kawamoto et al. (2015) experimentally showed that particles of diameter less than $25\ \mu\text{m}$ and greater than $300\ \mu\text{m}$ yielded the lowest cleaning results. We did not isolate the $25\ \mu\text{m}$ size range for testing, as these particles are already present within both the $25\ \mu\text{m}$ to $50\ \mu\text{m}$ and $80\ \mu\text{m}$ to $100\ \mu\text{m}$ size ranges, as observed in scanning electron microscopy (SEM) inspections (Figure 7.14). $300\ \mu\text{m}$ particles are evidently too heavy to be move by electrostatic forces alone, as see in the agglutinate tests, which already struggled with removing $100\ \mu\text{m}$ grains (Figure 7.15).

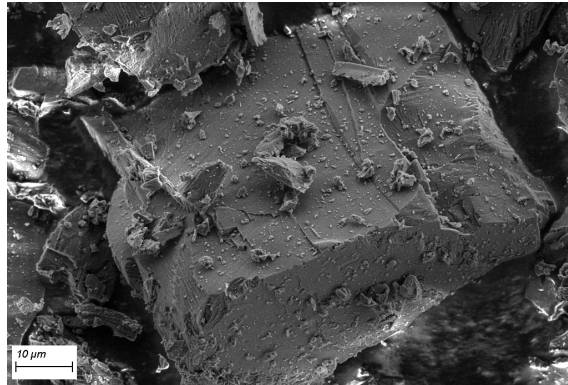


Figure 7.14: SEM image of a LHS-1 particle with smaller debris attached to its surface.

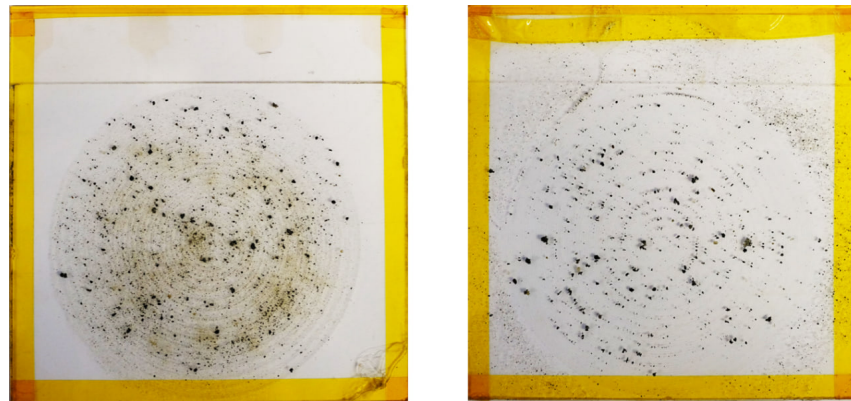


Figure 7.15: Photos of LHS-1 agglutinates before (left) and after (right) EDS activation. Remaining dust particles are grains larger than 1 mmeter, which are too heavy to be moved.

When agitated by movement, some of these particles are expected to detach from larger particles and attach to other surfaces. However, some were successfully removed by the EDS by leveraging their adhesion to larger grains. Inevitably, the particles that remain on the coating can only be removed through mechanical methods, such as wiping with isopropanol. Figure 7.16 illustrates what typically remains on a 90% clean surface and likely represents the cleaning limit of this EDS, regardless of the UV effect. Considering the weaker gravity, larger temperature fluctuations, and even lower moisture presence, the cleaning limits may differ on the Moon.

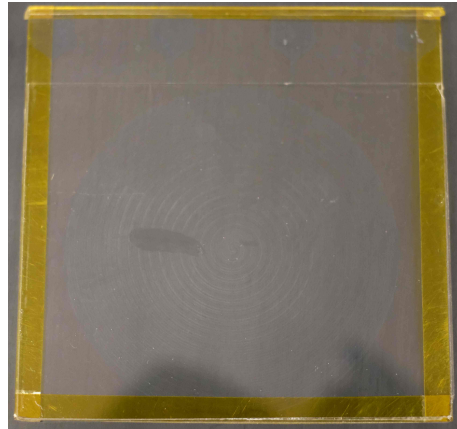


Figure 7.16: The LHS-1 sample, coated on glass and cleaned with EDS to achieve over 90% DRE, exhibits fine grain adhesion that could only be removed by wiping. The faint streak visible was created by dragging a finger across the surface to contrast the remnant dust layer.

7.4 Summary of Key Findings

Across all simulants types, it is clear that the DRE is significantly higher when the dusty surface is exposed to continuous UV irradiation. We have demonstrated the impact of UV irradiation on the efficiency of EDS in conditions resembling the lunar surface. Continuous exposure to UV, which leads to the continuous creation of photoelectrons and the formation of local weak plasma (qualitatively similar to lunar surface conditions), enhances the dust removal efficiency of the EDS system across various combinations of dust species and surface coating materials when compared to scenarios without UV radiation. Notably, the initial charge state of the particles does not seem to significantly affect the final cleanliness of the surface when exposed to an external charging mechanism. This is indicated by the minimal variation in removal efficiency observed in the UV cases, compared to the generally large spread in removal efficiency for the no-UV cases.

On smooth surfaces such as glass and Kapton, dust particles are efficiently removed across all simulants. The exception is larger particles ($80\ \mu\text{m}$ to $100\ \mu\text{m}$ and agglomerates) on Beta cloth, where it is likely that multiple-point contacts on the fiber material cause particles to adhere. Other factors such as temperature and pressure can potentially affect the system's dust removal efficiency, which remain important parameters for future tests. Dielectrophoretic forces may contribute to particle mobilisation, but analysis of the charge state of the particles and the EDS electric field lines is needed to confirm this.

Further experiments involving a broader range of simulants, materials, and environments, particularly the implementation of a plasma source and dedicated tests on smaller particles ($<25\ \mu\text{m}$), will help build a more comprehensive understanding of lunar conditions and efficient dust mitigation strategies.

7.5 Electric Field Simulation with COMSOL

In this study, the behaviour of particles with varying charges and masses within an electric field is estimated with a first-order simulation. It is hypothesised that electrostatic repulsion is not the sole force behind particle uplift and this simulation aims to assess whether the dielectrophoretic (DEP) force plays a significant role. While measuring these forces in a lab is challenging, simulations provide a controlled environment, despite the need for some potentially unrealistic estimations. COMSOL allows analysis of both electrostatic and DEP forces acting on a dielectric grain.

The electrostatic force's ability to induce dust uplift has been studied in relation to various adhesive forces and gravity, both experimentally and through modelling in different environments and applications (Sickafoose et al., 2002; Abbas et al., 2007; Poppe et al., 2010; Hartzell et al., 2011; Wang et al., 2016; Champlain et al., 2016). The non-uniform electric field generated by the EDS system may also induce a dielectrophoretic force on dielectric particles. While this force could assist in mobilising grains, its impact has been suggested to be minor compared to the Coulomb force at play (Pohl, 1951; Calle et al., 2006; Liu et al., 2010).

COMSOL Software

The COMSOL Multiphysics software (*COMSOL Multiphysics* 2024) uses the finite element method (FEM) to numerically simulate the electric field. This approach allows for the visualisation of the electric field intensity and distribution based on the actual dimensions and material properties of the EDS electrode setup.

To simplify the simulation we approximate the EDS as four electrodes in a cylindrically symmetric environment, effectively changing the ITO spirals to a series of concentric rings, but preserving the dimensions and (electrical) material properties of all EDS layers, and ensuring the modulation of the electric field propagating through the layers is as accurate as possible. This volume is then meshed for finite element computation which involves discretising the geometry into smaller geometric elements (triangles). COMSOL approximates the potential within each element with predefined polynomial functions, transforms the equations into a weak form before it assembles and solves the global system of equations. We can then modify the potential of the EDS electrodes in time to accurately mimic the EDS operation and the characteristics of our high voltage supply, and evaluate and calculate the resulting potential, electric field strength (see Figure 7.17) and DEP force anywhere in the volume.

7.5.1 Electric Field Strength

Electric field strength, denoted by \mathbf{E} , represents the force experienced by a unit positive charge placed in an electric field. It is a fundamental concept that describes the behaviour of charged particles and the interaction between them. The electric

field strength at a point is determined by the magnitude and direction of the electric field vectors in that region. Mathematically, it is defined as the force per unit charge, with its SI unit being volts per meter (V/m).

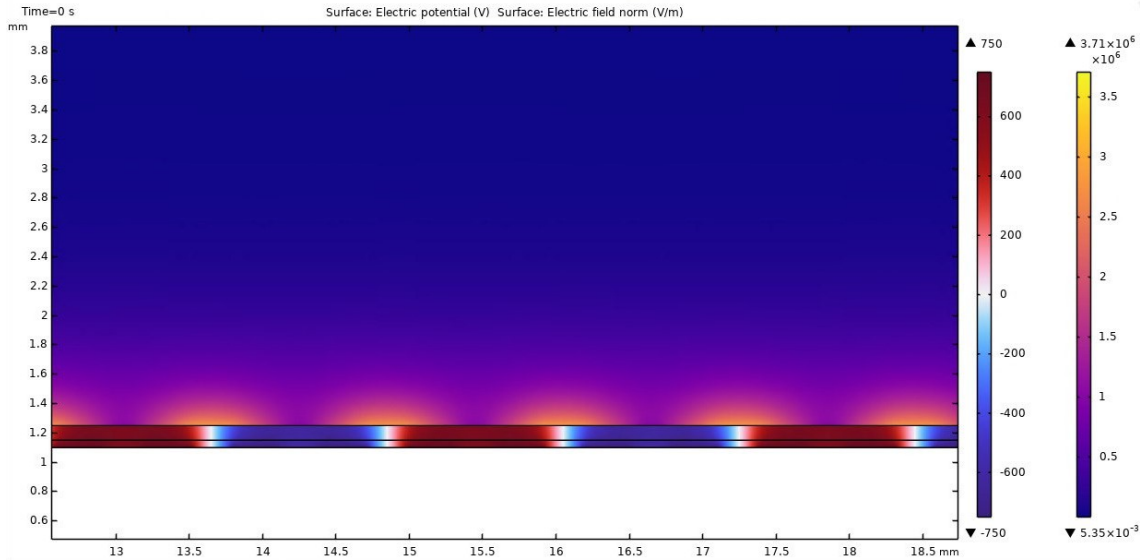


Figure 7.17: Potential and electric field in a subset of the COMSOL simulation volume at the start of an EDS cycle. The area between 1.15 and 1.2 mm contains the EDS layers and the electrodes, and is coloured by electric potential from -750 (blue) to $+750$ V (red), left colour bar. The electric field intensity in the (vacuum) volume above the EDS is coloured from high (yellow) to low (dark purple), right colour bar.

Figure 7.17 shows a side view of the EDS system. The graph separates the electric field into two components and visualises them both for the space above the EDS surface. The glass substrate is placed on an electrical ground, while the ITO electrodes are sandwiched between another much thinner glass coating using an adhesive. The electric field has two components: the radial component (E_r), which points away from or towards the axis of symmetry, and the axial component (E_z), which points along the axis of symmetry. In other words, the E_r points in the horizontal direction and E_z the vertical. The electric field of the setup is probed at four locations:

- 10 μm above the centre of a gap
- 10 μm above the junction of an electrode track and a gap
- 10 μm above the centre of an electrode track

10 μm is representative of the radius of the smallest dust grain in our experiments, and as such probing the largest (average) force felt by any solitary dust grain on the EDS surface. This is calculated by

$$|\mathbf{E}| = \sqrt{E_r^2 + E_z^2}. \quad (7.1)$$

Figure 7.18 illustrates the cases. Table 7.1 shows the maximum and minimum values of the electric potentials and electric field strengths for their respective components at each of the probed locations. For the same distance from the surface, i.e. at $10\ \mu\text{m}$, the vertical component (E_z) is of the same order of magnitude everywhere, indicating that this system has a strong field density for particle uplift overall.

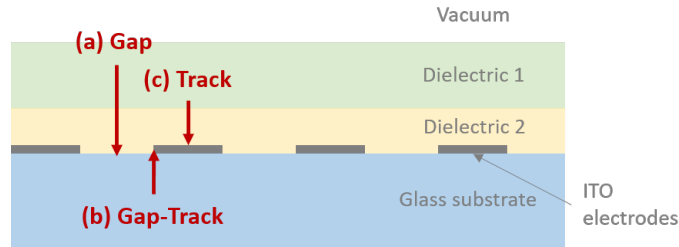


Figure 7.18: Illustration showing the positions where the electric field strength is probed, $10\ \mu\text{m}$ above the surface. (a) The center of the gap between two electrodes. (b) The region between the gap and the track. (c) The center of an electrode track.

	Location	V	V/m (r)	V/m (z)
(a)	$10\ \mu\text{m}$ above gap	± 610	$\pm 2.74 \times 10^6$	$\pm 1.04 \times 10^6$
(b)	$10\ \mu\text{m}$ above gap-track	± 620	$\pm 2.07 \times 10^6$	$\pm 1.43 \times 10^6$
(c)	$10\ \mu\text{m}$ above track	± 580	$\pm 6.90 \times 10^5$	$\pm 1.89 \times 10^6$

Table 7.1: Maximum and minimum electric field values at different positions above the EDS surface.

Location (a) is where E_r is the strongest, also the place with the greatest electric potential; particle placed in this position experiences the most pull in the horizontal direction, depending on its charge. Location (b) has the greatest electric potential, but not by much compared to location 1. In fact they have a very similar electric field profile. Location (c) is, as expected, the point where the electric field is strongest in the E_z direction. Experimental results show that the electric field strength that is applied in this EDS system is sufficient to liberate particles from the surface, provided the particles have a charge at all. The simulation results here can be used to calculate the criteria required for particle uplift. In the vertical direction, here it is assumed that only gravity needs to be overcome for uplift in a vacuum, as adhesion and friction mainly affect the horizontal component. I.e., the condition $mg \leq qE$ has to be met. Estimating the exact masses of the simulant grains is challenging for several reasons: the sample includes a range of sizes, and finer particles tend to adhere to larger ones, making it impractical to approximate the mass of a single grain. The charge-to-mass ratio q/m is introduced by rearranging the earlier equation. This ratio provides an indication of whether a particle will be uplifted, which can be computed using COMSOL.

Figure 7.19 shows the electric field and potential at locations indicated in Table 7.1. The blue line in the electric field graphs show the z-component (upward-pointing) of the electric field strength. Unsurprisingly, the field strength above the electrode

tracks is the highest, as shown in graph (c), and the weakest above the centre of a gap, shown in graph (a). The red line shows the electric field strength in the radial direction and exhibit the reverse trend: strongest above the gaps and weakest above the tracks.

7.5.2 DEP Force Strength

There are significant uncertainties when approximating the DEP force using simulations. Aside from the highly irregular shapes of regolith particles, no accurate or reproducible measurements of electric conductivity have been obtained for these particles, especially not for single grain characterisation. For instance, the charge and charge-to-mass ratio of a dust grain on the surface of a JSC-1A lunar regolith simulant are approximately two orders of magnitude smaller than those of an individual, isolated dust particle (Ding et al., 2013). At best, one can provide an effective range, but even this is challenging because conductivity varies with temperature, granular pressure, and the strength of the electric field itself. Experimental outcomes often show that DEP force is much weaker than theoretical predictions in scenarios involving electrodynamic dust removal.

Section 5.3 introduced the DEP force and the equation (Equation 5.4) to calculate its magnitude. Figure 7.20 shows the computed DEP forces again in the radial (E_r) and the axial (E_z) components. Realising (1) that particle permittivity cannot be smaller than that of vacuum, and (2) that the gradient of the electric field can point in many directions but generally always towards the EDS electrodes, which is always below the dust, it is perhaps not unexpected for the DEP force to be dominated by a downward component almost everywhere. For a particle of radius $25\ \mu\text{m}$, density $3.5\ \text{gcm}^{-3}$, relative permittivity of 3.5 (Buhler et al., 2007), a vertical force ≈ 10 times the magnitude of Earth's gravity is calculated at its maximum, just above an electrode track. The full list of assumed parameters is given in Table 7.2.

Property	Value
Vacuum permittivity ϵ_0	$8.85 \times 10^{-12}\ \text{Fm}^{-1}$
Particle permittivity ϵ_p	$3.5\epsilon_0$
Electrical conductivity of medium σ_m	$1 \times 10^{-25}\ \text{Sm}^{-1}$
Electrical conductivity of particle σ_p	$1 \times 10^{-6}\ \text{Sm}^{-1}$
Particle radius r	$25 \times 10^{-6}\ \text{m}$
Particle density n	$3.5\ \text{gcm}^{-3}$
Particle mass m	$2.29 \times 10^{-10}\ \text{kg}$
Acceleration due to gravity g	$9.81\ \text{ms}^{-2}$
Max. E-field $ \mathbf{E} _{\text{max}}$	$2 \times 10^6\ \text{Vm}^{-1}$
Max. gradient of E-field squared $\nabla \mathbf{E} _{\text{max}}^2$	$5.5 \times 10^{16}\ \text{V}^2\text{m}^{-4}$

Table 7.2: Dust grain, EDS system and vacuum properties defined for COMSOL simulation.

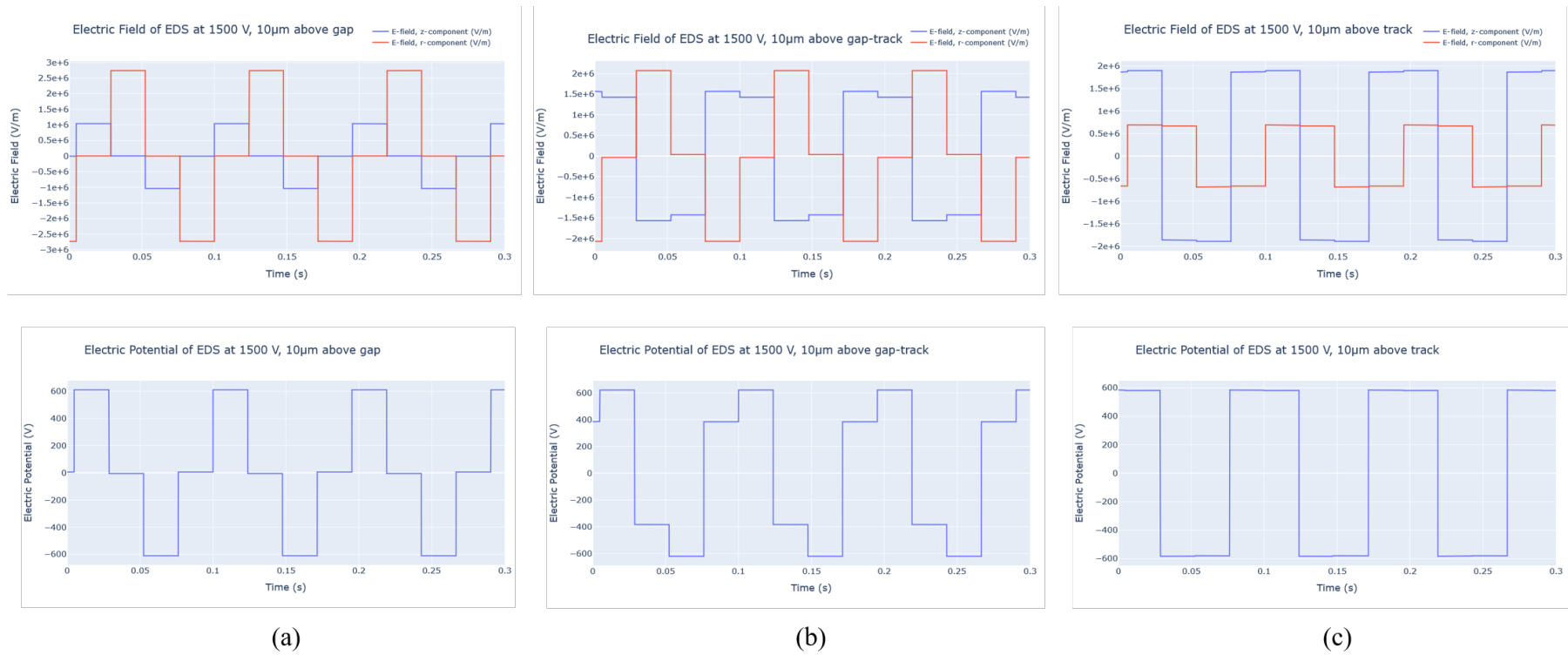


Figure 7.19: Electric field and electric potential at different locations according to Table [7.1](#). The top row displays the electric field strengths at various locations above the EDS surface, with their respective components. The z-component (vertical) is depicted in blue, and the r-component (radial) is depicted in red. The bottom row shows the corresponding electric potential.

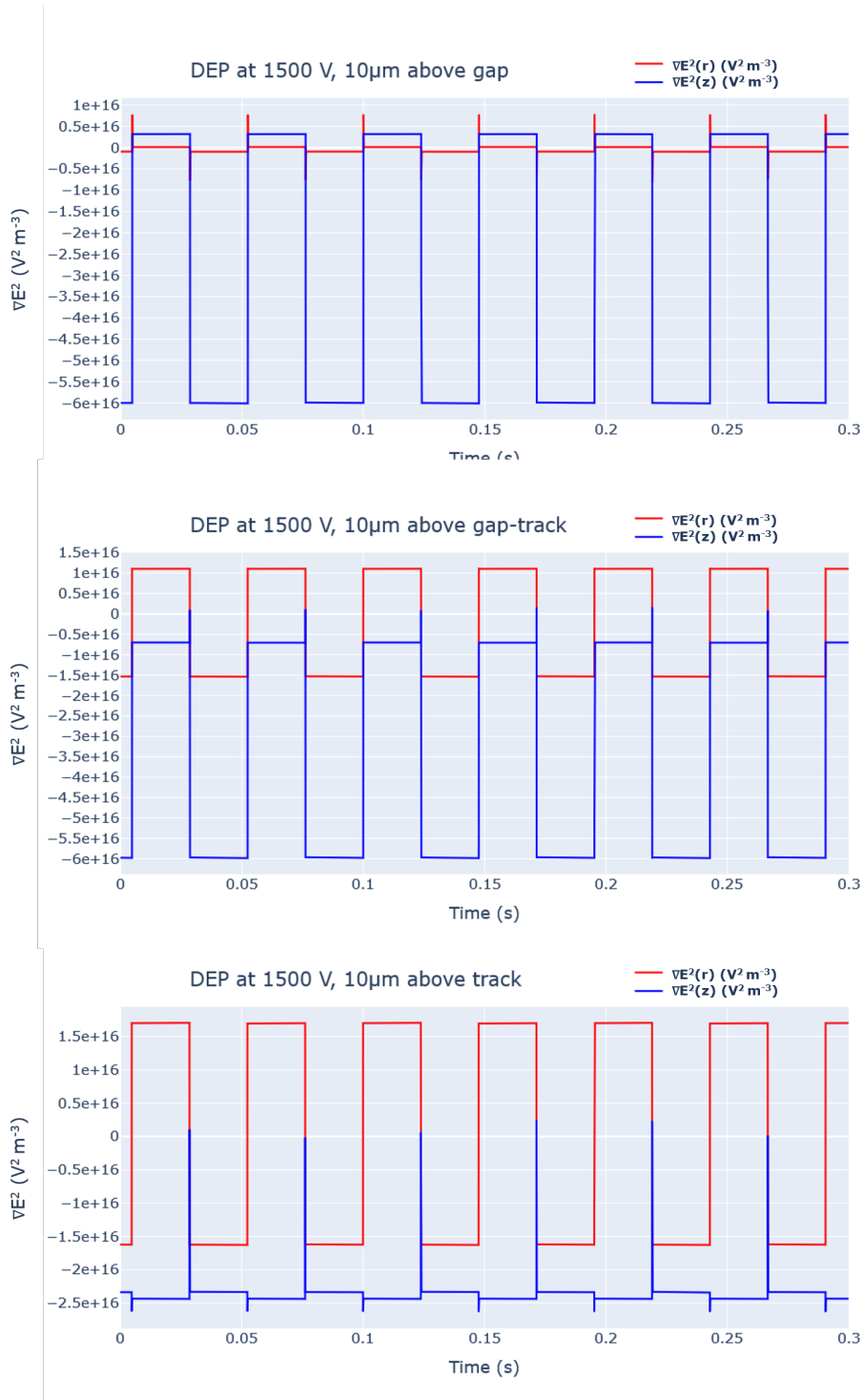


Figure 7.20: Magnitude of DEP forces at various locations according to Figure 7.18. The z-component (vertical) is depicted in blue, and the r-component (radial) is depicted in red. The z-component is mostly negative at all positions, indicating the force is downward-pointing overall. The r-component dominates in some cases but would not generate uplift.

The radial component of the DEP, which in some places is the dominant component, would also not generate uplift by itself, but can be very effective in mobilising the

grains, rubbing grains against each other and the surface coating, and triggering tribocharging in the process. This can then take the place of more natural charging mechanisms (e.g. UV) to allow electrostatic repulsion to generate uplift on the EDS.

We should also note that Equation 5.4 is a slight simplification, in reality permittivity is complex, and has an imaginary, frequency dependent component according to

$$\epsilon^*(\omega) = \epsilon' - i\frac{\sigma}{\omega} \quad (7.2)$$

where ϵ' is the real part of the complex permittivity, ω is the angular frequency, and σ is the electrical conductivity. For our square wave pulse, when the potential has reached its maximum, the forces are essentially electrostatic; the fields do not change in time, and our simplistic estimate of the force above is valid. At the rise and fall of the square wave, which can also be thought of as an infinite sum of sine waves of different frequencies and thus have frequency dependent components, and the complex permittivity will play a role. But even at very high frequencies (with a correspondingly small amplitude), the impact on the DEP force with our square wave is likely insignificant.

Kawamoto et al., 2006 performed a numerical simulation to determine the magnitude of the coulomb for and DEP force exerted on theoretical spherical dielectric particles, their result yielded $q/m = 6.10 \times 10^{-5}$ C/kg. In our case, if we take the electric field strength in Comsol and assume the electrostatic force is equal or larger than gravity, we got an initial estimate of $q/m > 4.91 \times 10^{-6}$ C/kg, roughly 10 times smaller. However, that was neglecting the DEP force, which is generally downwards and for the electrostatic repulsion force to be stronger than both DEP and gravity, we get an estimate of $q/m > 5.0 \times 10^{-5}$ C/kg, which is in very good agreement with (Kawamoto et al., 2006).

Regardless of the simulation, it is important to keep in mind that this is a highly theoretical case of a single perfect sphere with no charge that exists, without the consideration of adhesive forces, no less. The real system, in a plasma and with a significant layer of dust modulating the electric field is highly complex so we can only provide first order estimates of the DEP force. It is likely that the DEP force increases as the gradient of the electric field increases in a plasma, owing to the debye shielding of the plasma, but we can only speculate on what the dust layer and the electric field around charged and highly irregular shapes of the individual grains. However, just from a consideration of the direction of the DEP, we can conclude that the Coulomb force is the dominant force to drive particle motions, in agreement with Kawamoto et al., 2006. If the DEP has a positive contribution to the DRE of the EDS, it would be by inciting tribocharging, which then can be uplifted via the electrostatic repulsion.

Limitations

The simulation was a largely simplified system where grain cohesion, secondary electron currents, collective behaviour on dust grain charging were neglected.

Dust grain cohesion is likely to have the most significant impact if it was taken into consideration, as dust particles are likely to travel in clumps rather than single particles. Surface electric field should also decay exponentially above the surface due to Debye shielding, where a cloud of charged particles forms around a test charge, effectively reducing its electric field at a distance.

Overall, this simulation work provided a foundational understanding of the EDS electric field. Future implementations should incorporate additional features to create a more realistic model.

References

- Abbas, M. M. et al. (2007). “Lunar dust charging by photoelectric emissions”. In: *Planetary and Space Science* 55.7-8, pp. 953–965.
- Bechkoura, H., N. Zouzou, and M. Kachi (2023). “Mechanics of Particle Motion in a Standing Wave Electric Curtain: A Numerical Study”. In: *Atmosphere* 14.4, p. 681.
- Buhler, C. R. et al. (2007). “Test method for in situ electrostatic characterization of lunar dust”. In: *2007 IEEE Aerospace Conference*. IEEE, pp. 1–19.
- Calle, C. I. et al. (2004). “Electrodynamic shield to remove dust from solar panels on Mars”. In: *Proceedings of the 41st Space Congress, Cape Canaveral*.
- Calle, C. I. et al. (2006). “Electrodynamic dust shield for surface exploration activities on the moon and Mars”. In: *57th International Astronautical Congress conference*. KSC-2006-125.
- Calle, C. I. et al. (2011). “Active dust control and mitigation technology for lunar and Martian exploration”. In: *Acta Astronautica* 69.11-12, pp. 1082–1088.
- Carroll, A. et al. (2020). “Laboratory measurements of initial launch velocities of electrostatically lofted dust on airless planetary bodies”. In: *Icarus* 352, p. 113972.
- Champlain, A. et al. (2016). “Lunar dust simulant charging and transport under UV irradiation in vacuum: Experiments and numerical modeling”. In: *Journal of Geophysical Research: Space Physics* 121.1, pp. 103–116.
- COMSOL Multiphysics (2024). Software. URL: <https://www.comsol.com/>.
- Cruise, R. D. et al. (2023). “Triboelectric charge saturation on single and multiple insulating particles in air and vacuum”. In: *Scientific Reports* 13.1, p. 15178.
- Ding, N., J. Wang, and J. Polansky (2013). “Measurement of dust charging on a lunar regolith simulant surface”. In: *IEEE Transactions on Plasma Science* 41.12, pp. 3498–3504.
- Gu, J. et al. (2022). “Experimental study on particles directed transport by an alternating travelling-wave electrostatic field”. In: *Powder Technology* 397, p. 117107.

- Hartzell, C. M. and D. J. Scheeres (2011). “The role of cohesive forces in particle launching on the Moon and asteroids”. In: *Planetary and Space Science* 59.14, pp. 1758–1768.
- Katzan, C. M. and J. L. Edwards (1991). *Lunar dust transport and potential interactions with power system components*. Tech. rep. NASA.
- Kawamoto, H., K. Seki, and N. Kuromiya (2006). “Mechanism of travelling-wave transport of particles”. In: *Journal of Physics D: Applied Physics* 39.6, p. 1249.
- Kawamoto, H. and T. Shibata (2015). “Electrostatic cleaning system for removal of sand from solar panels”. In: *Journal of Electrostatics* 73, pp. 65–70.
- Kawamoto, H. et al. (2011). “Mitigation of lunar dust on solar panels and optical elements utilizing electrostatic traveling-wave”. In: *Journal of Electrostatics* 69.4, pp. 370–379.
- Liu, G. Q. and J. S. Marshall (2010). “Effect of particle adhesion and interactions on motion by traveling waves on an electric curtain”. In: *Journal of Electrostatics* 68.2, pp. 179–189.
- Mantovani, J. G. and C. I. Calle (2007). “Controllable Transport of Particulate Materials for In-situ Characterization”. In: *2007 IEEE Aerospace Conference*. IEEE, pp. 1–9.
- Pohl, H. A. (1951). “The motion and precipitation of suspensoids in divergent electric fields”. In: *Journal of applied Physics* 22.7, pp. 869–871.
- Poppe, A. and M. Horányi (2010). “Simulations of the photoelectron sheath and dust levitation on the lunar surface”. In: *Journal of Geophysical Research: Space Physics* 115.A8.
- Sickafoose, A. A. et al. (2002). “Experimental levitation of dust grains in a plasma sheath”. In: *Journal of Geophysical Research: Space Physics* 107.A11, SMP–37.
- Wang, X. et al. (2016). “Dust charging and transport on airless planetary bodies”. In: *Geophysical Research Letters* 43.12, pp. 6103–6110.

8 Conclusion and Outlook

In this thesis, experiments were conducted to investigate the combined effect of UV photoelectric charging and an external electric field on the mobilisation of charged lunar regolith simulants. The study addressed the existing gap in understanding the efficacy of the Electrodynamic Dust Shield (EDS) under solar radiation to better comprehend particle dynamics in conditions simulating the lunar environment, particularly the photoemission charging mechanism prevalent on the lunar dayside.

Using a UV lamp to simulate the photoemission charging mechanism demonstrated that dust particles could attain substantial charge states, enhancing their interaction with an EDS system. Continuous UV exposure, which generates photoelectrons and forms local weak plasma, improved the dust removal rates across various dust species and surface coatings compared to scenarios without UV radiation. The initial charge state of particles did not significantly impact the final cleanliness, as evidenced by the relatively minimal variation in removal efficiency in the presence of UV, unlike the larger spread in the case without UV. However, certain combinations of particle size and coating exhibited resistance to the cleaning technology, i.e. 80–100 μm grains on Beta cloth, which emphasises the importance of tailoring EDS parameters to address the diverse particle characteristics found on the lunar surface.

While most forces responsible for mobilisation and uplift are electrostatic, whether from photoemission or initial tribocharging, simulations of the time-varying and non-uniform electric field emanating from the EDS system indicated a strong presence of dielectrophoretic force (DEP) on dielectric particles. This DEP force was however predominantly acting in a downward and horizontal direction, therefore the minimum condition of $qE > mg + \text{DEP}$ must be fulfilled according to experimental observation, adding to the forces that electrostatic repulsion has to overcome to generate uplift. The estimated minimum q/m values are modest, yet effective cleaning efficiencies were demonstrated even in the absence of many natural charging mechanisms and under gravitational conditions stronger than those anticipated for EDS usage. Triboelectric charging induced by movement from either DEP or exploration activities such as spacecraft landing and astronaut EVAs will also further facilitate charging, but the magnitude of such charging is difficult to assess.

Overall, considering photoelectric charging as one of the primary mechanisms on the lunar surface, the EDS is likely to demonstrate increased effectiveness with additional charging sources in space. Although no single dust mitigation method is universally applicable on the lunar surface, EDS appears to be the most suitable for a wide range of applications and has a higher technological readiness level compared

to many other proposed mechanisms. A similar EDS system is also expected to function relatively well on Mars due to the planet's comparable exposure to solar and space radiation. However, since Mars' average surface pressure is approximately 0.6% of Earth's average sea-level atmospheric pressure, some modifications to the EDS system would be necessary. In this case, more frequent cleaning operations might be required to minimise the discharge time of deposited dust grains, compared to the high-vacuum lunar environment. Near Enceladus's plume where ESA plans to land its first 'large-class' mission to investigate the habitability of an ocean world, EDS technology may be required for the spacecraft to penetrate the cloud of gas and water ice in the South Pole region. The mechanism's versatility and straightforward mechanics enable its adaptation to the diverse environments within our solar system.

Outlook

An in-situ dust deposition method should be implemented in future experimental setups to better replicate real-world conditions. Existing research also indicates that the charge acquired in a vacuum is sustained for a long period of time. Future research should incorporate a plasma source and explore a more diverse and comprehensive range of lunar regolith simulants.

Future research should investigate additional factors such as temperature and pressure to assess their impact on the efficiency of dust removal systems. Expanding experimental studies to encompass a wider array of simulants, actual lunar regolith, and varying environmental conditions, especially incorporating a plasma source and examining smaller particles ($< 25 \mu\text{m}$), will enhance our understanding of lunar conditions and improve dust mitigation strategies on the Moon. Further enhancements in efficiency should explore integrating other mitigation technologies with the EDS. This integration will amplify their effectiveness and broaden their applicability not only for lunar missions but also for future space exploration endeavours.